# The State of the Blazar:
# Investigations of Variability Patterns in the Very High Energy Gamma-ray Emission from Northern Blazars

**A THESIS**
**SUBMITTED TO THE FACULTY OF THE GRADUATE SCHOOL**
**OF THE UNIVERSITY OF MINNESOTA**
**BY**

**Karlen Shahinyan**

**IN PARTIAL FULFILLMENT OF THE REQUIREMENTS**
**FOR THE DEGREE OF**
**Doctor of Philosophy**

**Advisor:**
**Lucy Fortson**

**December, 2017**

# Abstract

Blazars are active galactic nuclei with jets aimed in our direction. They are one of the most energetic astrophysical phenomena and in the very-high-energy (VHE; $> 100$ GeV) gamma-ray regime comprise the dominant extragalactic source class. Variability in the non-thermal emission of blazars is one of the key observables for discerning the details of their emission regions. In this thesis, I explore VHE gamma-ray emission properties of blazars in a variety of states. After a detailed description of the VERITAS instrument and data analysis, I present an in-depth study of an unusually stable extreme blazar (formerly, an unidentified source), HESS J1943+213, for which no concrete evidence of variability has been detected to date. The study includes the steps towards identifying HESS J1943+213 as a blazar using VLBA observations and estimation of the source redshift with gamma-ray spectra. Models of leptonic emission from the source and hadronic emission from cosmic-ray interactions along the line of sight are presented for explaining the gamma-ray observations. I then proceed to characterize the emission of two blazars in rapidly flaring states, Mrk 421 and MS 1221.8+2452. The dataset for Mrk 421, the first blazar detected in VHE gamma rays, comes from one of the brightest VHE gamma-ray flares ever observed and offers a unique opportunity for exploring VHE gamma-ray and multi-wavelength emissions of the source on timescales of few minutes. The flare of MS 1221.8+2452, on the other hand, allows for the construction of the first VHE gamma-ray spectrum of the source, which is used along with contemporaneous multi-wavelength observations to construct and model the SED of the source during the flare. Moreover, the source exhibits a spectral hysteresis pattern in X-rays during the flaring period, which is tied to the acceleration and cooling timescales of particles in the emission zone. Finally, I investigate, PG 1553+113, a blazar exhibiting long-term periodic flux modulations in lower-energy gamma rays – due to periodic accretion flow instabilities, jet precession, or the presence of a binary supermassive black hole system – and search for a similar periodicity signal in the VHE gamma rays.

# Contents

# List of Tables

# List of Figures

# Chapter 1

# Introduction

## 1.1 Gamma-ray Astrophysics

Gamma rays are the highest energy photons in the electromagnetic spectrum, spanning the energy regime above hundreds of keV.

Gamma-ray astrophysics is one of the youngest branches of astronomy, dating back to 1986 when the Whipple Collaboration, under the leadership of Trevor Weekes detected the Crab Nebula at TeV energies (Weekes et al., 1989). The path to this discovery was long and arduous, with over three decades of failed attempts. The early gamma-ray experiments did not have enough funding to build sensitive enough detectors, lacked knowledge of particle interactions that only became available with modern accelerator experiments, and did not have access to sufficient computing power (Lorenz & Wagner, 2012).

### 1.1.1 From Cosmic-Rays to Gamma Rays

The discovery of cosmic-rays by Victor Hess (F. Hess, 1912) is largely responsible for initiating and motivating the search for gamma rays. Cosmic-rays are energetic, charged particles and were seen as tracers of high-energy astrophysical processes, likely non-thermal in nature based on the extreme observed energies.

The charged nature of the cosmic-rays meant that any intervening magnetic fields would deflect their trajectories and obfuscate the locations of their sources (except perhaps for the highest energy cosmic-rays). On the other hand, gamma rays can

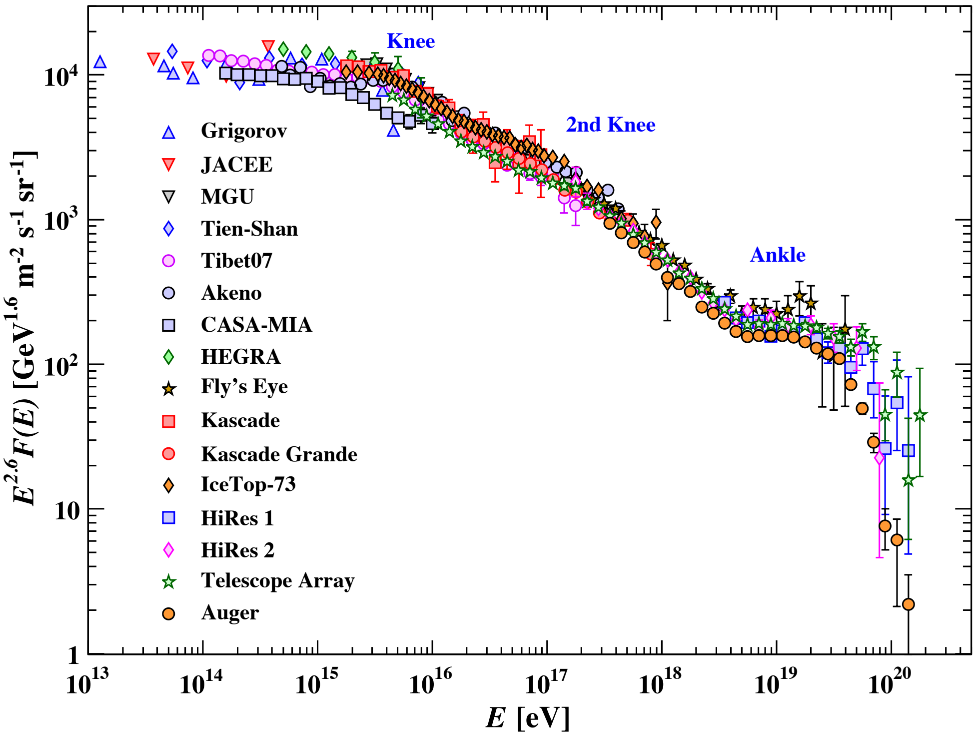

Figure 1.1: Measurement of the cosmic-ray spectrum with air-shower arrays (from Patrignani & Particle Data Group, 2016).

be produced by cosmic-ray interactions. As neutral particles, gamma rays are not deflected by magnetic fields along their travel from an astrophysical source to Earth. They were thus seen as promising messengers for not only identifying the sources of the cosmic-rays but also for carrying valuable information about the properties of cosmic-ray acceleration sites (Hillas, 2013).

There are two primary processes for generating gamma rays through cosmic-ray interactions. The first, commonly referred to as *leptonic* processes, involve interactions of relativistic electrons ($e^-$) or positrons ($e^+$) with magnetic fields to produce *synchrotron* radiation (Section 1.1.3) or interactions with low-energy photon fields to produce gamma rays (*inverse-Compton* scattering – Section 1.1.3). Synchrotron radiation is effective for production of lower-energy gamma rays, while inverse-Compton scattering can efficiently generate the higher-energy gamma rays.

The second family of gamma-ray generation processes, known as *hadronic*, primarily rely on interactions of relativistic protons with nuclei. These interactions produce charged and neutral pions (pion production; Section 1.1.3). The neutral pions decay into pairs of gamma rays, while charged pions decay into electrons, positrons, and neutrinos. Pion production requires and is more effective in higher density environments, where availability of targets for protons allows high enough interaction rates. In environments with extremely strong magnetic fields and low particle densities, synchrotron radiation by protons can also become a significant production mechanism for gamma rays (e.g., Mücke et al., 2003).

Dedicated cosmic-ray detectors have measured the cosmic-ray spectrum with high precision over twelve decades of energy. Cosmic-rays with energies below 10 GeV are dominated by particles from the solar wind. Figure 1.1 shows the cosmic-ray spectrum measurements by ground-based arrays (not including the solar-wind dominated regime). The spectrum has distinctive features, such as the *knee* ($E \sim 3 \times 10^{15}$ eV), the *2nd knee* ($\sim 8 \times 10^{16}$ eV), and the *ankle* ($\sim 10^{18}$ eV) (Patrignani & Particle Data Group, 2016, and references within). Cosmic-rays below the *knee* are thought to be of Galactic origin, with the *knee* related to the maximum energy of Galactic accelerators. The physical reasons behind the other features are less certain. There is some evidence the *2nd knee* is related to the transition from lighter to heavier cosmic-ray nuclei. The *ankle* is either due to extragalactic population of cosmic-rays overtaking the Galactic cosmic-rays or due to attenuations from proton-photon interactions involving the CMB (i.e., the GZK cutoff) (Patrignani & Particle Data Group, 2016, and references within).

There are, however, still no direct detections of cosmic-ray sources, even for ultra-high-energy cosmic-rays (UHECR; $> 10^{18}$ eV). For $> 10^{20}$ eV energies UHECRs are largely undeflected over large distances, though they are very rare with about 1 particle per square km per century. Thus, gamma rays remain the best tools for studying regions of highest-energy cosmic-ray production and acceleration.

Both cosmic-rays and gamma rays are absorbed by the Earth's atmosphere. It was not until after the discovery of extensive air showers initiated by cosmic-rays and gamma rays (Auger et al., 1939) that ground based experiments for gamma-ray and cosmic-ray detection could be developed.

### 1.1.2 Extensive Air Showers

Ground-based gamma-ray observatories rely on detections of extensive air showers in order to reconstruct properties of the initial gamma ray. A gamma ray can initiate an extensive air shower when it interacts with an atom in the Earth's atmosphere and produces a $e^+e^-$ pair. The resulting $e^+$ and $e^-$ are ultrarelativistic and will travel faster than the speed of light in the atmosphere, emitting Cherenkov radiation (Section 1.1.3). The $e^+$ and $e^-$ will be deflected by ions in the atmosphere and produce gamma rays through bremsstrahlung (Section 1.1.3). These gamma rays will, in turn, interact with atoms and pair-produce, generating an electromagnetic (EM) cascade or a shower as more and more interactions occur when particles travel deeper into the atmosphere. The air shower will typically reach a maximum of $\sim 10^{10}$ particles (and in the amount of Cherenkov light), before tapering off. The shower development will continue until $e^+e^-$ energies dip below ∼85 MeV, when collisional energy losses overtake radiative losses (Heitler, 1954).

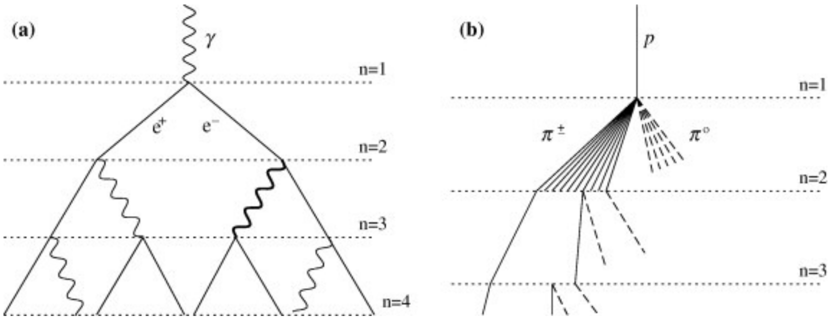

Figure 1.2: Simple models of gamma-ray and cosmic-ray initiated extensive air showers from Matthews (2005). Dashed lines indicate neutral pions that decay into gamma rays.

Extensive air showers can be initiated by cosmic-rays as well. For cosmic-ray initiated showers, cosmic-ray protons or nuclei undergo pion-production interactions with atmospheric ions. The resulting neutral pions do not undergo additional interactions, but decay into gamma rays, producing EM showers. The charged pions decay into muons and neutrinos; however, before they can decay, they can interact with ions and produce more pions. This pion-production process continues until the pion energies are below a critical energy, at which point they are more likely to decay than to interact with ions. The resulting muons can penetrate deep into the atmosphere before decaying into electrons, positrons, and neutrinos. The electrons and positrons, in turn, produce more EM showers (Matthews, 2005). The interactions of charged pions before their decays, which include deflections to their trajectories, causes the cosmic-ray generated showers to be less confined and more extended than their gamma-ray counterparts.

An illustration of extensive air shower development processes for both gamma-ray and cosmic-ray air showers is provided in Figure 1.2. The interaction lengths are marked with the numbered $n$ levels (not drawn to scale). The interaction length is the distance for an electron or a positron to lose the bulk of its energy to bremsstrahlung, for a gamma ray to pair-produce, or for a charged pion to interact with an ion (Matthews, 2005).

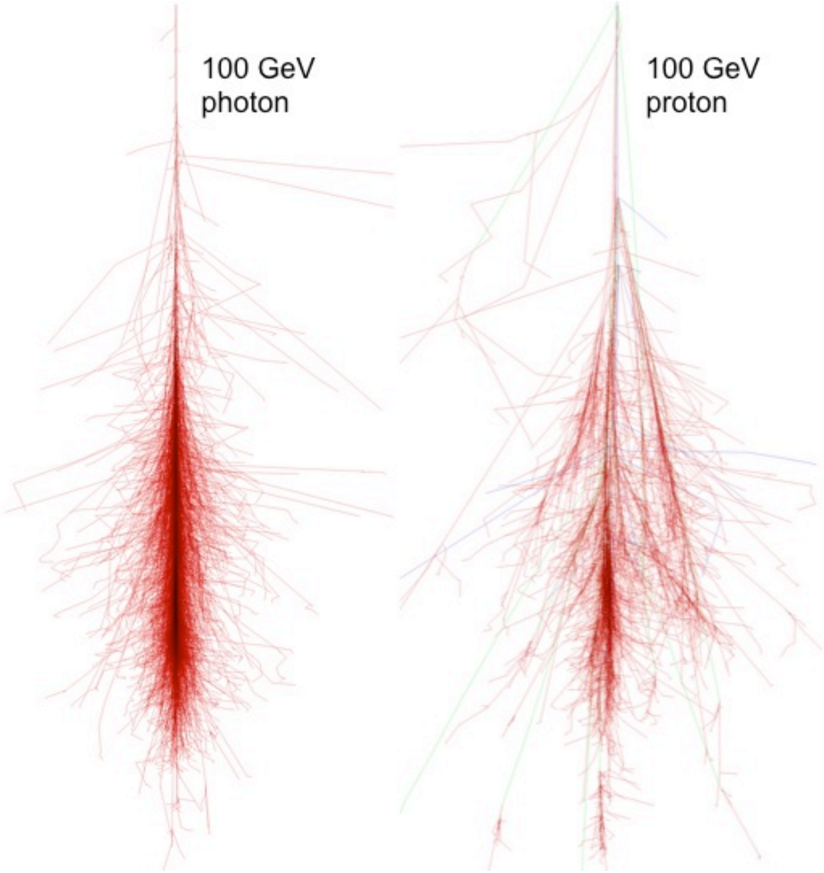

Figure 1.3: Monte Carlo simulations of 100 GeV gamma-ray (*left*) and cosmic-ray (*right*) initiated extensive air showers generated with the CORSIKA package.

A major difficulty for gamma-ray detectors is the separation of cosmic-ray showers from gamma rays. In the very high energy (VHE; $>$ 100 GeV) regime - the energy regime accessible to ground-based gamma-ray observatories - there are $\sim 10^3 - 10^4$ cosmic-rays per a single gamma-ray for an average-strength source. An effective method to differentiate between gamma-ray- and cosmic-ray-initiated showers (gamma-hadron separation) is necessary to obtain reliable measurement of a gamma-ray source. The successful gamma-hadron separation techniques rely on differences in shower morphologies or in independent detections of shower byproducts (e.g., muons) to identify and reject cosmic-ray events. Figure 1.3 shows particle tracks from Monte Carlo simulations[1] of 100 GeV gamma-ray and cosmic-ray air showers. Perhaps the most discriminatory feature for separating cosmic-ray showers from gamma rays is the width of the shower. The difference in widths is even more pronounced for heavier cosmic-ray nuclei.

### 1.1.3 Radiative Processes

Exploration of properties of astrophysical sources with gamma-ray observations requires understanding of some basic radiative processes. Processes such as synchrotron radiation, inverse-Compton scattering, pion production, and $\gamma - \gamma$ pair-production are important for characterizing gamma-ray emission, while Bethe-Heitler ($\gamma$-nucleus) pair production, bremsstrahlung, and Cherenkov radiation are necessary for understanding gamma-ray detection techniques. The following discussion draws heavily from Rybicki & Lightman (1986) and Longair (1992).

#### Cherenkov Radiation

Cherenkov radiation is emitted when a charged particle moves faster than the speed of light of the medium. This can be shown using the Liénard-Wiechert potentials, which describe the electromagnetic field for a relativistically moving charge,

$$\boldsymbol{A}(\boldsymbol{r},t) = \frac{\mu_0}{4\pi r}\left[\frac{q\boldsymbol{v}}{\kappa}\right]_{ret} \; ; \; \phi(\boldsymbol{r},t) = \frac{1}{4\pi\epsilon_0 r}\left[\frac{q}{\kappa}\right]_{ret}, \tag{1.1}$$

where, $\kappa = [1 - \boldsymbol{v}\cdot\boldsymbol{i}_{obs}/c]$, $\epsilon_0$ and $\mu_0$ are the permittivity and permeability of free space, $c$ is the speed of light, $r$ is the radius, $q$ and $\boldsymbol{v}$ are the charge and velocity of the particle,

---

[1] www.ikp.kit.edu/corsika

and $\boldsymbol{i}_{obs}$ is the unit vector in the direction of observation of the charge. The quantities are evaluated at a retarded time.

A charged particle moving in a vacuum at a constant velocity does not radiate. The situation can change with a particle moving within some medium with an index of refraction, $n$. In this case $\kappa$ in Equation 1.1 becomes $\kappa = [1 - (n\boldsymbol{v} \cdot \boldsymbol{i}_{obs})/c]_{ret}$. Along a cone defined by the condition, $1 - (n\boldsymbol{v} \cdot \boldsymbol{i}_{obs})/c = 0$, or $\cos\theta = c/nv$, the potentials become infinite, allowing radiation to occur.

Conceptually, the radiation can be thought of as a result of a "shock wave" behind the moving particle. Under the $v > c/n$ condition, the particle displaces charges in the medium much faster than the medium can relax, causing a net disturbance in the medium in the direction of the particle's motion. The radiation from the disturbance is coherent and strongly polarized. This radiation propagates at a fixed angle with respect to the direction of the motion of the particle. This opening angle, given as $\theta_C = \cos^{-1}(c/nv)$, defines the Cherenkov cone in which Cherenkov radiation is confined (the regime where $v > c/n$).

The spectrum of the Cherenkov radiation from ultrarelativistic charged particles in the atmosphere (e.g., particles in extensive air showers) peaks at near ultraviolet (UV) wavelengths. The radiation is short-lived and appears as a brief flash, requiring fast detectors to be observed.

### Bethe-Heitler Pair Production

A photon with an energy greater than $2m_ec^2$ can produce $e^+e^-$ pairs when it passes through the Coulomb field of a nucleus. The cross section for the interaction is expressed as $\sigma \propto \alpha r_e^2 Z^2$, where $\alpha$ is the fine structure constant, $r_e$ is the electron radius, and Z is the atomic number.

Bethe-Heitler pair production is important in extensive air shower development, as it is responsible for the conversions of the initial and secondary gamma rays into $e^+e^-$ pairs. In addition, this process can also act as a gamma-ray absorption process near the source of their emission.

### Bremsstrahlung

Bremsstrahlung or braking radiation (*English* translation of the *German* term) is radiation emitted by one charged particle passing through the Coulomb field of another. The most common example is an electron moving near an ion and radiating as it is deflected and accelerated.

In extensive air showers, bremsstrahlung is responsible for the production of secondary gamma rays from interactions of relativistic $e^+$ and $e^-$ with ions in the atmosphere. For production of gamma rays in astrophysical sources, bremsstrahlung is invoked for explaining gamma-ray emission from e.g., supernova remnants, where electrons are traveling through ionized gas.

### Synchrotron

Synchrotron is the radiation from relativistic charged particles accelerated by a magnetic field, with particles gyrating around the magnetic field as they travel along the field lines with a pitch angle, $\alpha$. In the non-relativistic regime, this type of radiation is known as cyclotron radiation, the frequency of which is given by the gyration frequency or the gyrofrequency, $\nu_g = \frac{qB}{2\pi m}$. The cyclotron radiation can be characterized by an isotropic dipole radiation. Synchrotron radiation is the relativistic equivalent of cyclotron, with the gyrofrequency given as,

$$\nu_g = \frac{qB}{2\pi\gamma m}, \tag{1.2}$$

where $q$ is the particle charge, $m$ is the particle mass, $B$ is the strength of the magnetic field, and $\gamma$ is the Lorentz factor. For an electron, $\nu_g = 28\ \gamma^{-1}\text{GHz T}^{-1}$.

Due to beaming effects, synchrotron radiation is no longer isotropic, but contained in a small angle ($\sim 1/\gamma$) along the direction of the particle's motion.

The total power radiated by a relativistic charged particle undergoing acceleration is given by the relativistic Larmor formula,

$$P = \frac{q^2\gamma^2}{6\pi\epsilon_0 c^3}[|a|_\perp^2 + \gamma^2|a|_{||}^2], \tag{1.3}$$

where $|a|_\perp$ and $|a|_{||}$ are the perpendicular and parallel components of the particle's acceleration. For synchrotron radiation, the particle's acceleration is always perpendicular to its velocity, $v$. Thus, $|a|_{\|} = 0$ and $|a|_{\perp} = qvB\sin\alpha/\gamma m$, from the relativistic Lorentz force law. The radiated power or energy loss for synchrotron is then,

$$P_{sync} = -\frac{dN}{dE} = \frac{q^4 B^2 \beta^2}{6\pi\epsilon_0 c m^2}\gamma^2 \sin^2\alpha;\ \beta = \frac{v}{c}. \tag{1.4}$$

From synchrotron power, it is possible to calculate the synchrotron cooling timescale for a given particle using $t_{sync} = E/P_{sync} = \gamma mc^2/P_{sync}$. It is then evident that $t_{sync} \propto m$. Thus, the synchrotron cooling timescale is vastly longer for a proton than for an electron.

Assuming the charged particle is an electron ($m \rightarrow m_e$; $q \rightarrow e$) and averaging over isotropic pitch angles, Equation 1.4 can be rewritten as,

$$P_{sync} = -\frac{dN}{dE} = \frac{4}{3} c\sigma_{\mathrm{T}} U_{mag} \beta^2 \gamma^2, \tag{1.5}$$

where we have defined the magnetic energy density, $U_B$ and the Thomson cross-section, $\sigma_{\mathrm{T}}$ as,

$$U_B = \frac{B^2}{8\pi};\ \sigma_{\mathrm{T}} = \frac{e^4}{6\pi m_e^2 \epsilon_0^2 c^4}. \tag{1.6}$$

Then, the full expression for $t_{sync}$ for synchrotron radiation from an electron is,

$$t_{sync} = \frac{E}{P_{sync}} = \frac{3 m_e c}{4\sigma_{\mathrm{T}} U_{mag} \beta^2 \gamma}. \tag{1.7}$$

For an ultrarelativistic electron, $\beta \sim 1$ and the synchrotron cooling time can be estimated by, $t_{sync} \sim 7.7 \times 10^7 (B/1\ \mathrm{T})^{-2} \gamma^{-1}$.

The synchrotron spectrum from a power-law distribution of electrons can be crudely estimated by exploiting the fact that the synchrotron spectrum of a single electron is sharply peaked around a critical frequency, $\nu_{\mathrm{c}}$ given as,

$$\nu_{\mathrm{c}} = \gamma^2 \nu_{\mathrm{g}} = \left(\frac{E}{m_e c^2}\right)^2 \nu_{\mathrm{g}};\ \text{where } \nu_{\mathrm{g}} = \frac{eB}{2\pi m_e}. \tag{1.8}$$

Here, $\nu_{\mathrm{g}}$ is the non-relativistic gyrofrequency, $B$ is the magnetic field strength, and $e$, $E$, and $m_e$ are the charge, energy, and mass of an electron.

The radiated energy in a frequency range $\nu + \mathrm{d}\nu$ corresponding to an energy range $E + dE$ and for an electron energy distribution given by $N(E)$ can be expressed by,

$$J(\nu)\mathrm{d}\nu = \left( - \frac{\mathrm{d}E}{\mathrm{d}t} \right) N(E)\mathrm{d}E. \tag{1.9}$$

With $N(E) \propto E^{-p}$ representing the power-law electron spectrum and $-\mathrm{d}E/\mathrm{d}t$ given by Equation 1.4, the emission can be expressed as,

$$J(\nu) \propto B^{\frac{p+1}{2}} \nu^{-\frac{p-1}{2}}, \tag{1.10}$$

implying that the synchrotron radiation spectrum from a power-law distribution of electrons also follows a power-law form with an index $\alpha = (p-1)/2$.

### Inverse Compton

Inverse-Compton (IC) scattering is referred to the interaction between a photon and a relativistic electron, in which the energy of the photon is greatly increased at the expense of the electron. For a non-relativistic electron, the interaction is known as Thomson scattering and is governed by the Thomson cross section, $\sigma_T$. The scattering is elastic with no energy transferred to the photon and the emitted power given by the Larmor formula is,

$$P_T = \sigma_T c U_{rad}, \tag{1.11}$$

where $U_{rad}$ is the energy density of the photon field. For inverse-Compton scattering, involving a relativistic electron, the power after scattering can be written in the electron rest frame in terms of the Thomson scattering power,

$$P = P' = \sigma_T c U'_{rad}, \tag{1.12}$$

with primed quantities indicating the electron rest frame and unprimed quantities denoting the observer frame. $P = P'$, since Larmor power is Lorentz invariant.

It can be shown that $U'_{rad} = U_{rad} 4(\gamma^2 - 1/4)/3$. Then, the net inverse-Compton power radiated, given by $P_{IC} = P - P_T$ is,

$$P_{IC} = \frac{4}{3} c \sigma_{\mathrm{T}} U_{rad} \beta^2 \gamma^2. \tag{1.13}$$

A comparison of Equations 1.13 and 1.7 will reveal the striking similarity between the formulation of the radiated power for synchrotron radiation and for inverse-Compton scattering. In fact, a quantity defined as $P_{IC}/P_{sync} = U_{rad}/U_B$ is often used to describe the relative contribution from the two processes. In the synchrotron-self Compton paradigm (see Section 1.3.4), the quantity is referred to as equipartition and characterizes the energetics of an emission region.

The IC cooling timescale can be expressed as,

$$t_{IC} = \frac{E}{P_{IC}} = \frac{3m_e c}{4\sigma_{\mathrm{T}} U_{rad} \beta^2 \gamma}. \tag{1.14}$$

A caveat to Equations 1.13 and 1.14 is that the Thomson cross-section is only valid for the low-energy photon regime, $E_\gamma \ll m_e c^2$. For higher-energy photons, the proper cross-section is given by the Klein-Nishina formula (Klein & Nishina, 1929),

$$\sigma_{KN} = \frac{\pi r_0^2}{E_\gamma} \left\{ \left( 1 - \frac{2(E_\gamma + 1)}{E_\gamma^2} \right) ln(2E_\gamma + 1) + \frac{4}{E_\gamma} + \frac{1}{2} - \frac{1}{2(2E_\gamma + 1)^2} \right\}, \tag{1.15}$$

where, $r_0 = e^2/m_e c^2$ is the classical electron radius. Compared with the Thomson cross-section, $\sigma_T = 8\pi r_0^2/3$, the Klein-Nishina cross-section is much smaller at higher energies. Thus, in the Klein-Nishina regime, IC scattering is much less efficient.

The IC spectrum from a single electron is even more sharply peaked than for synchrotron radiation, with the peak near the maximum frequency, $\nu_{max} \approx 4\gamma^2\nu_0$. In the same manner as in Section 1.1.3, it can be shown that the IC spectrum for a power-law distribution of electrons with an index, $p$ also follows a power-law shape, with an index $\alpha = (p-1)/2$.

### Pion Production

A collision of a relativistic proton with another proton can produce pions. Alternatively, pions can also be produced by interactions of ultra-high-energy protons with CMB photons (known as the GZK cutoff).

The resulting pions decay into gamma rays, electrons, positrons, and neutrinos. The decay channels are different for neutral and charged pions. Neutral pions predominantly decay into two gamma rays,

$$\pi^0 \to \gamma + \gamma, \tag{1.16}$$

with a small fraction (∼1%) of the time decaying into a gamma ray and an $e^+e^-$ pair,

$$\pi^0 \rightarrow \gamma + e^+ + e^-. \tag{1.17}$$

The charged pions decay into muons and neutrinos, the former of which promptly decays into electrons and neutrinos.

$$\pi^+ \rightarrow \gamma + \mu^+ + \nu_\mu \ ; \ \pi^- \rightarrow \gamma + \mu^- + \bar{\nu}_\mu. \tag{1.18}$$

The muons then decay through,

$$\mu^- \rightarrow e^- + \bar{\nu}_e + \nu_\mu \ ; \ \mu^+ \rightarrow e^+ + \nu_e + \bar{\nu}_\mu. \tag{1.19}$$

Pion decay is important in hadronic models of gamma-ray production.

### $\gamma$-$\gamma$ Pair Production

A gamma-ray photon interacting with a lower-energy photon can produce an $e^+e^-$ pair. This is a dominant gamma-ray absorption process for astrophysical sources. This pair-production interaction can occur above a threshold energy given by,

$$E_{th} = \frac{2m_e^2c^4}{E_{bg}(1-\cos\theta)}, \tag{1.20}$$

where $E_{th}$ is the threshold gamma-ray energy and $E_{bg}$ is the energy of the lower-energy photon. The pair-production cross section above this threshold is given by,

$$\sigma_{\gamma\gamma} = \frac{3\sigma_T}{16}(1-\beta^2)\left[2\beta(\beta^2-2) + (3-\beta^4)ln\left(\frac{1+\beta}{1-\beta}\right)\right] \tag{1.21}$$

with $\beta = (1 - E_{th}/E_{bg})^{0.5}$. The optical depth can be obtained from $\sigma_{\gamma\gamma}$ as,

$$\tau_{\gamma\gamma}(E_\gamma, z) = \int_0^z dz'\frac{dl}{dz}\int_{-1}^1 d\mu\frac{1-\mu}{2}\int_{E_{th}}^\infty dEn_E(E,z')(1+z')^3\sigma_{\gamma\gamma}(\beta',z'). \tag{1.22}$$

Here, $z$ is the redshift, $\mu = \cos\theta$, and $n_E$ is the number density of low-energy photons. The optical depth for gamma-ray absorption from pair production is a function of distance and energy. The amount of absorption also depends on the density of the lower-energy photon field, which for extragalactic sources is dominated by the extragalactic background light.

### Extragalactic Background Light

The extragalactic background light (EBL) is the combined diffuse radiation from stars and dust. It is characterized by a spectral energy distribution (SED) with two humps (see Figure 1.4). The first hump is from direct starlight and extends from UV to near-IR, peaking near 1 $\mu$m. The second hump, attributed to dust emission (reradiated starlight) peaks in mid-IR ($\sim$100 $\mu$m) and extends from near- to far-IR (Hauser & Dwek, 2001).

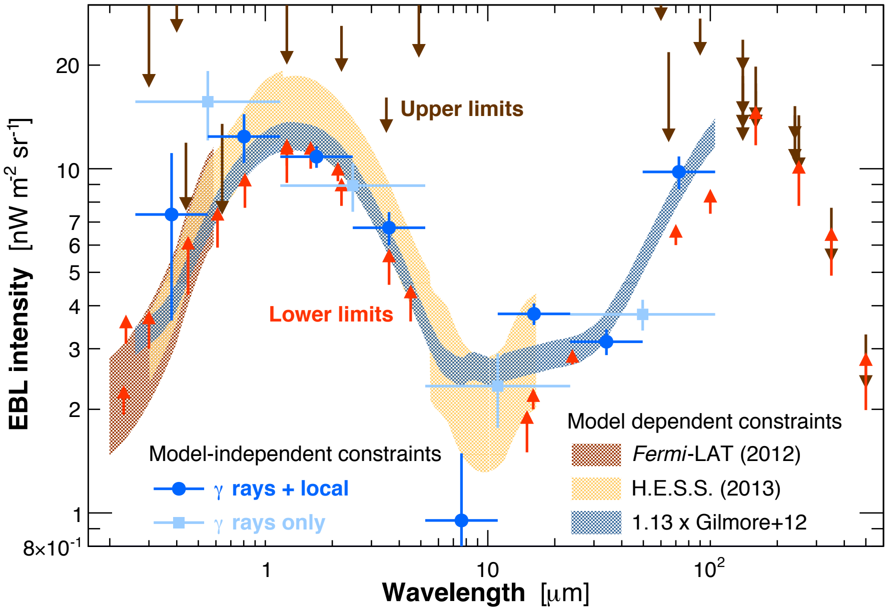

Figure 1.4: Observation constraints and measurements of EBL from Biteau & Williams (2015).

The EBL is the primary absorber of extragalactic gamma rays (through $\gamma$-$\gamma$ pair production) after they escape the vicinity of their production region. The amount of absorption due to the EBL is directly related to the distance of the source and the energy of the gamma ray. This effect creates a gamma-ray horizon in the VHE gamma-ray regime, defined for a given energy as the distance at which gamma rays are attenuated by a factor of $1/e$.

On the other hand, the effects of EBL absorption on gamma-ray spectra of extragalactic sources can be used to measure the density of the EBL (e.g., Biteau & Williams, 2015). Accurate measurements of the EBL density can put constraints on the total energy budget of the universe, give insights into the epoch of formation and the evolution of galaxies over cosmic time, estimate the Hubble constant, and place limits on exotic physics phenomena, such as Lorentz invariance violation (e.g., Primack et al., 2005; Dwek & Krennrich, 2013; Biteau & Williams, 2015).

### 1.1.4 Gamma-ray Detection Techniques

There have been three general methods for detecting gamma rays. The first two methods are ground-based, sensitive to VHE gamma rays, and rely on the detection of extensive air showers initiated by gamma rays.

An effective technique for detecting extensive air showers (and by extension gamma rays) was developed after the discovery of Cherenkov radiation (Cherenkov, 1934). Cherenkov radiation is emitted when a particle travels faster than the speed of light in a medium. Blackett (1948) noted that such radiation could be emitted when a cosmic-ray particle traveled through the air. This idea motivated Galbraith & Jelley (1953) to assemble a rudimentary detector made out of a searchlight mirror, a single photomultiplier tube, pulse amplifier, an oscilloscope, and a garbage can (for shielding) to look for Cherenkov radiation pulses from extensive air shower particles (Figure 1.5). They successfully observed a rate of 1–2 pulses per minute, marking the experimental beginnings of air Cherenkov detectors. For a detailed summary of the development of Cherenkov imaging arrays from their conception until the modern era see Hillas (2013).

The technique of detecting gamma-rays using Cherenkov light from their extensive air showers, referred to as the Cherenkov technique (Weekes & Turver, 1977), involves imaging the Cherenkov light from the shower and parameterization of the image to distinguish between cosmic-ray and gamma-ray events and to reconstruct properties of the primary gamma ray. An example of what gamma-ray and cosmic-ray shower images look like in imaging Cherenkov detectors is provided in Figure 1.6.

Full details of the modern use of the technique with Imaging Atmospheric Cherenkov Telescopes (IACT) are included in the description of the VERITAS setup, observations, and data analysis (Chapter 2).

Another technique relies on the detection of particles from extensive air showers initiated by gamma rays. The first iterations of such detectors involved arrays of small

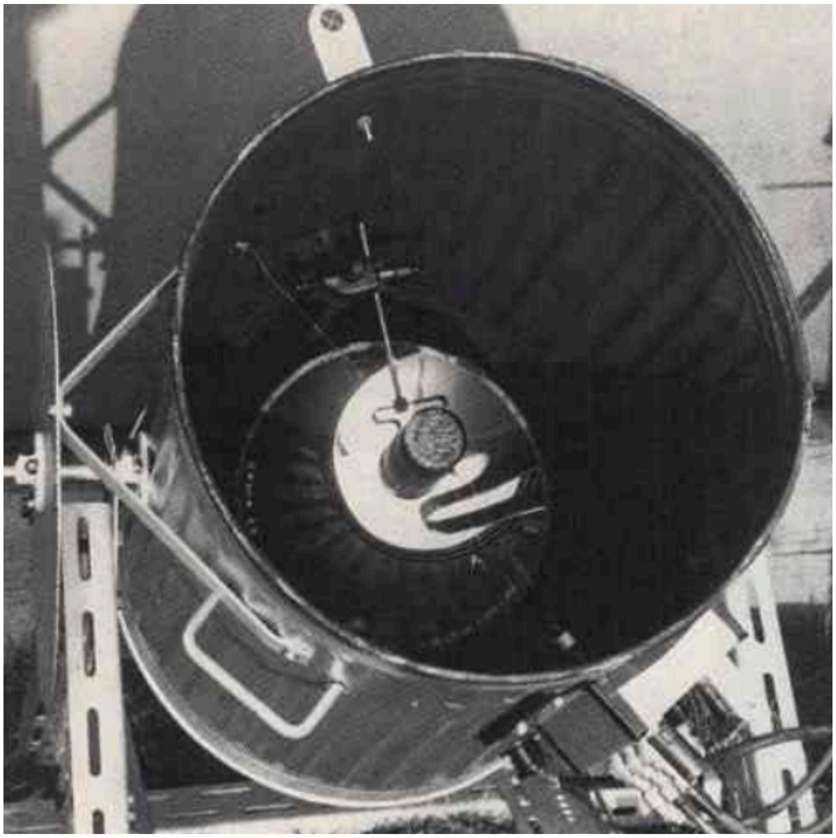

Figure 1.5: The first air-Cherenkov detectors, housed in a garbage can (Galbraith & Jelley, 1953). Photo credit: *Trevor Weekes*.

scintillators covering very large areas (e.g., Chicago Air Shower Array (Borione et al., 1994; Cassidy et al., 1997)), with energy thresholds of $> 100$ TeV. The next generation of these detectors aimed for a lower-energy threshold. The Milagro detector (Atkins et al., 2003) used a large pool of water with photo-multiplier tubes at the bottom to image the extensive air showers from the Cherenkov light emitted when shower particles passed through water (known as the water Cherenkov technique).

Air Cherenkov detectors tend to have higher sensitivities, angular and energy resolutions than air shower detectors; however, air shower detectors have much longer duty cycles (can operate during the day as well as the night) and much larger fields of view.

With the advent of space-based experiments, another gamma-ray detection technique became available. Space-based gamma-ray detectors rely on the pair production

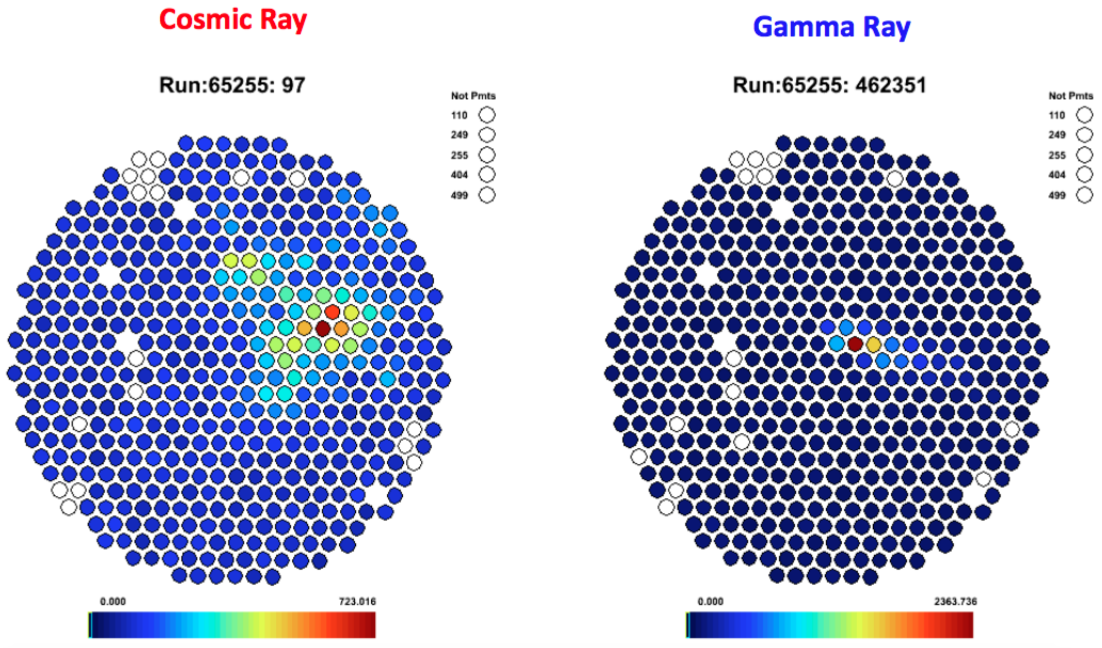

Figure 1.6: Examples of cosmic-ray (*left*) and gamma-ray (*right*) images in an IACT (VERITAS) camera. The colors indicate the number of digital counts in each pixel.

of gamma rays within the instrument and measurements of the pairs to reconstruct the direction and energy of the original gamma rays. The basic design of these detectors includes an anticoincidence detector, used to veto events from cosmic-rays, a conversion foil that facilitates the pair-production interaction, particle tracking detectors to measure the tracks of the resulting $e^-$ and e$^-$ pairs, and a calorimeter to measure the energies of the pairs (e.g., Thompson, 2015). The space-based gamma-ray detectors operate in the high-energy (HE; 100 MeV–100 GeV) gamma-ray regime.

### 1.1.5 Current Gamma-ray Observatories

Detection techniques and existing observatories separate the field into two energy regimes, divided between space-based and ground-based detectors. Space-based gamma-ray instruments detect gamma rays directly by forcing the gamma-ray to undergo a pair-production interaction within the instrument. The size of these instruments limits their sensitivity to gamma rays below few hundred GeV.

The higher energy gamma rays can be detected with ground-based observatories, employing the Cherenkov technique to image extensive air showers or detecting the particles within air showers by constructing detectors at high altitudes.

### The *Fermi* Gamma-Ray Space Telescope

The Large Area Telescope (LAT) is an instrument on board the *Fermi* Gamma-ray Space Telescope[2] . The design of the instrument follows the principles described in Section 1.1.4 for space-based gamma-ray detectors.

The detector section of LAT is composed of a 4 × 4 array of identical towers, each housing a tracker composed of layers of silicon strip detectors, a calorimeter containing layers with Cesium Iodide bars and recorded by photodiodes. The towers are enclosed in anticoincidence shields made out of scintillator tiles, used as an initial discriminator for charged cosmic-ray events.

LAT operates in the HE gamma-ray regime and is sensitive to photons with energies ranging from 20 MeV to 300 GeV. *Fermi*-LAT has a field of view of 2.4 sr at 100 GeV and scans the full sky once every three hours. The $1\sigma$ energy resolution of the LAT is $< 10\%$. The 68% containment angular resolution for a single photon is energy dependent with resolution of $< 3.5^\circ$ at 100 MeV and $< 0.15^\circ$ at $>$ 10 GeV. LAT can determine source location with better than $0.5'$ accuracy for >100 MeV photons (Atwood et al., 2009).

### HESS, MAGIC, VERITAS

There are three main IACT arrays currently operating in the world, dubbed as the third generation of IACT detectors: High Energy Stereoscopic System (HESS)[3] . Major Atmospheric Gamma Imaging Cherenkov (MAGIC) telescope array[4] . Very Energetic Imaging Telescope Array System (VERITAS)[5] . Each array is associated and operated by a major collaboration.

HESS is located in Namibia and is composed of four 12 m telescopes (known as HESS I) arranged in a square, with a large 28 m telescope (HESS II) placed at the center of the array. HESS I is primarily sensitive to gamma-rays above 100 GeV, whereas HESS II

---

[2] https://fermi.gsfc.nasa.gov

[3] http://www.mpi-hd.mpg.de/hfm/HESS

[4] http://wwwmagic.mppmu.mpg.de

[5] http://veritas.sao.arizona.edu

can detect gamma-rays down to ∼20 GeV. The Southern Hemisphere location of HESS provides it with an optimal view of the Galactic Center and the Galactic plane. The HESS Collaboration is the largest of the IACT collaborations, with 260 members from 13 countries.

Located on the Canary Island of La Palma, MAGIC is a system of two 17 m IACTs. The large-diameter telescopes made it optimal for sensitivity at the lower energy gamma rays, covering the energy range above ∼30 GeV. The MAGIC collaboration involves 165 members from 11 countries.

For details on VERITAS, see Chapter 2.

### 1.1.6 The VHE Gamma-ray Sky

The current catalog of the VHE gamma-ray sky includes 207 sources[6] and is displayed in Figure 1.7. Of the 207 sources, 74 are extragalactic, 78 are Galactic, and 55 are unidentified, but likely of Galactic origin.

Galactic sources include supernova remnants, pulsar wind nebulae, gamma-ray binaries, star formation regions, and regions of shocked interstellar medium.

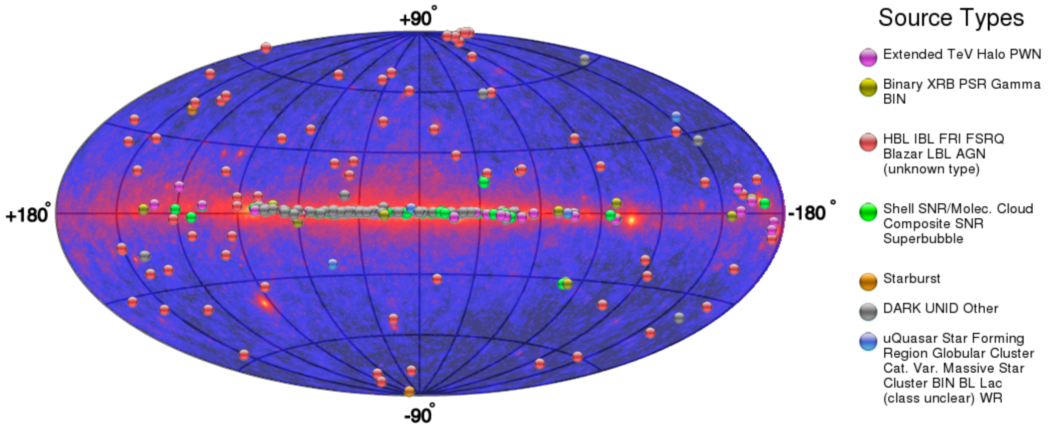

Figure 1.7: All currently detected VHE gamma-ray sources from TeVCat (http://tevcat.uchicago.edu)

Active Galactic Nuclei (AGN) dominate the extragalactic VHE gamma-ray sky, comprising 72 out of 74 detected extragalactic sources so far. The remaining two are

---

[6] http://tevcat.uchicago.edu

starburst galaxies, M82 and NGC 253.

## 1.2 Active Galactic Nuclei

Active Galactic Nuclei (AGN) are supermassive black holes (SMBH; $\mathrm{M} > 10^6\ \mathrm{M}_\odot$) in galactic centers, actively accreting matter. They are the most energetic persistent emitters in the Universe, with emission that spans over 20 orders of magnitude in energy from radio to VHE gamma rays. AGN have historically been differentiated from passive,"normal", or star-forming galaxies, in which the dominant radiation is from stellar processes.

A wide range of properties are attributed to the AGN phenomenology, including flux and spectral variability in all observed bands and on a wide range of timescales (e.g., Boettcher et al., 2012), compact emission regions (e.g., Ulrich et al., 1997), and high luminosity, with bolometric luminosity reaching, $\mathrm{L}_{bol} \sim 10^{48}$ erg $\mathrm{s}^{-1}$ (e.g., Mortlock et al., 2011). Characteristic AGN properties can differ between observed bands, however, which has caused the emergence of a large number of AGN subclasses followed by a major, multi-decade, and on-going unification effort (e.g., Urry & Padovani, 1995; Padovani et al., 2017).

### 1.2.1 Black Hole Accretion

The extreme energetics of AGN could, at least partially be attributed to the fact that accretion onto a black hole is an extremely efficient process for converting rest-mass energy into radiation. The energy released from an accreted particle is the energy loss required for it to reach the last stable circular orbit of a black hole. As derived by Longair (2003), this energy can be expressed as,

$$E_{\mathrm{orbit}} = \left\{ \frac{1 - \frac{r_g}{r}}{(1 - \frac{3r_g}{2r})^{\frac{1}{2}}} - 1 \right\} mc^2, \text{where } r_g = \frac{2GM}{c^2}, \tag{1.23}$$

where $M$ is the mass of the black hole, $m$ is the mass of the particle, $r$ is the radius of the orbit, $G$ is the gravitational constant, $c$ is the speed of light, and $r_g$ is the Schwarzchild radius.

The efficiency, $\xi$, for converting rest mass to energy can be expressed as, $\xi = \frac{E_{\rm orbit}}{mc^2}$. For a static (non-spinning) black hole the last stable orbit is given by $r = 3r_g$, which results in $\xi = 0.057$. The release of 5.7% of a particle's rest mass in energy during accretion is enormous (for comparison, burning hydrogen to helium in stellar nucleosynthesis only releases 0.7% of the rest mass). The energy conversion efficiency can be even higher for spinning, *Kerr* black holes (Shapiro & Teukolsky, 1983). In maximally spinning black holes, where the spin direction is aligned with the rotation direction of the particle, the last stable orbit is $r = 4.5r_g$, giving a conversion efficiency of 42.3% (Longair, 1992)!

### 1.2.2 AGN Anatomy and Emission

The substructure of AGN, shown in Figure 1.8, consists of a central black hole, an accretion disk, a dusty torus,"broad" and "narrow" line regions, and in some cases a relativistic jet (collimated outflow).

The masses of the central black holes ($M_{\rm BH}$) range from $\sim 3 \times 10^4\ M_\odot$ (Peterson et al., 2005) to over $4 \times 10^{10}\ M_\odot$ (Ghisellini et al., 2010). For a supermassive black hole with $M_{\rm BH} = 10^9\ M_\odot$, the last stable orbit is located at $r = 3r_g \sim 3 \times 10^{-4}$ pc (assuming a static black hole).

The black hole in an AGN is surrounded by an accretion disk, which feeds the black hole and powers the AGN. The accretion disk typically extends from $\sim 10^{-3}$ pc to $\sim 10^{-2}$pc and is bright mostly in UV and optical energies. The disk can also power a hot corona of ionized gas, bright in X-rays (e.g., Mushotzky et al., 1993). Clouds of gas near the central black hole can be ionized and become bright in nebular emission lines. The denser clouds closer to the black hole (0.01–1 pc), with fast rotation speeds generated by the influence of the central gravitational potential, are considered part of the broad-line region. The name is derived from detection of these clouds in (primarily) optical spectra, where they exhibit broad ionization lines, because of their fast rotation. Beyond the accretion disk and the broad-line region, is the dusty torus (0.1–10 pc) that can obscure the accretion disk as it absorbs the UV-optical light and reemits in the infrared (IR). The region of ionized clouds with lower densities located further away from the SMBH (10–1000 pc) and with lower rotational speeds is known as the narrow-line region (e.g., Netzer, 2015).

Finally (and most importantly for this thesis), AGN can launch and power relativistic jets. These jets are based near the accretion disk and can extend to kpc, and in some cases, Mpc scales (Bagchi et al., 2014).

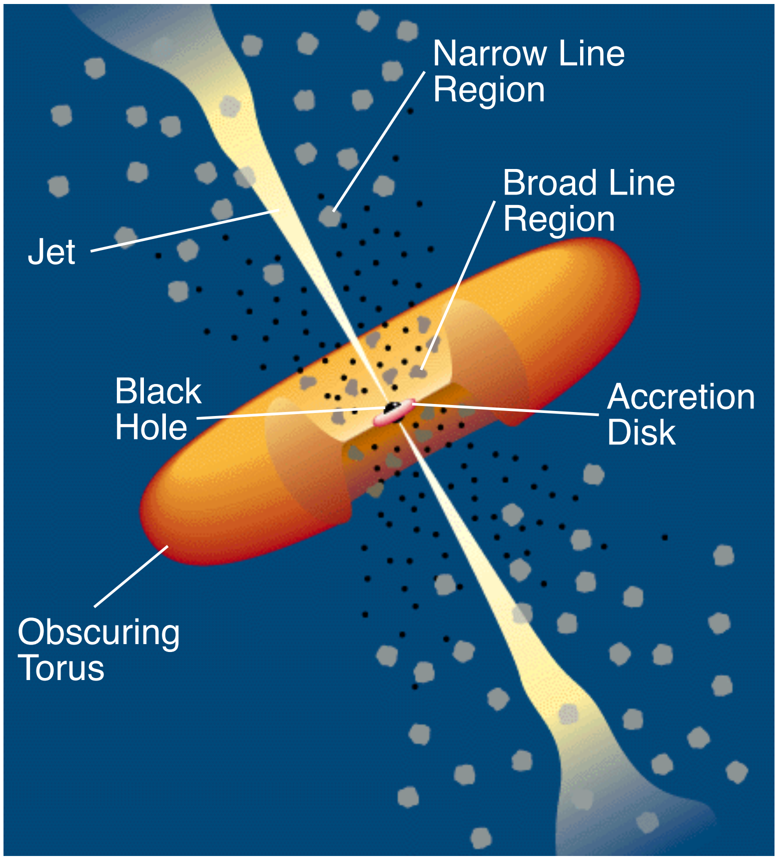

Figure 1.8: A schematic representation of an AGN and its components (Urry & Padovani, 1995).

The component that dominates emission from an AGN depends on the observed energy band. Figure 1.9 provides approximate representation of the emission from each AGN component in a SED. The thermal emission from AGN spans sub-mm to X-ray band energies, whereas the non-thermal emission from the jet can cover most of the electromagnetic spectrum.

The radiation from accretion disks, winds, and jets can heat and eject gas from both the vicinity of the AGN and from the host galaxy, and can shut off the black hole accretion process and arrest star formation in the galaxy. This process, known

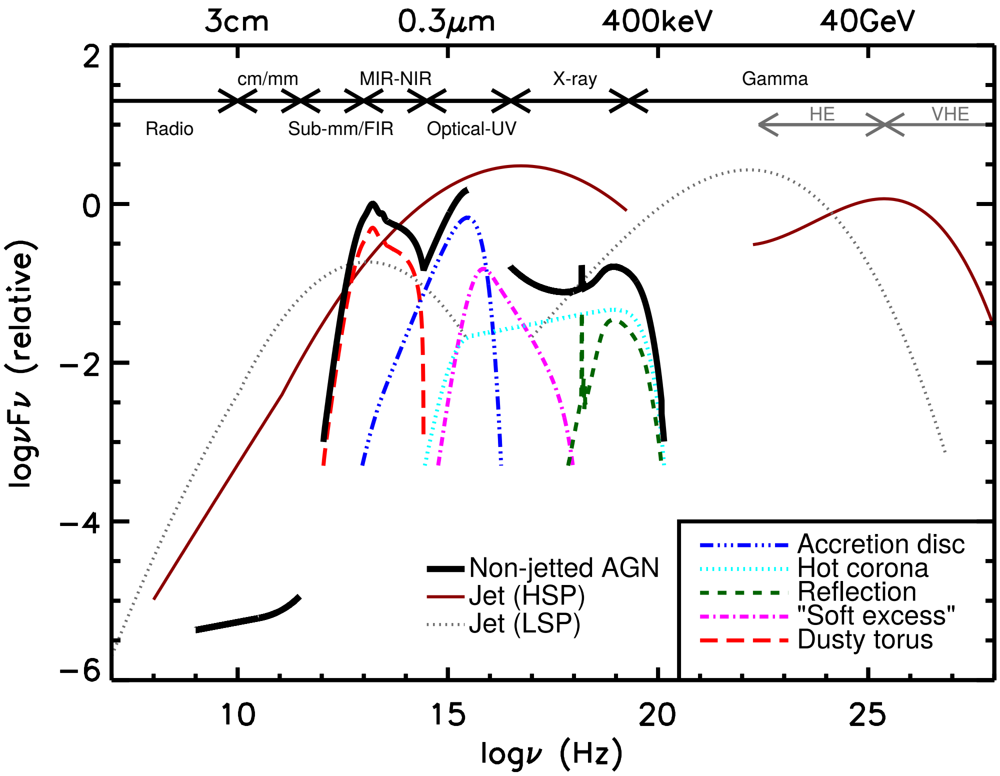

Figure 1.9: AGN emission components. Credit: Harrison (2014).

as AGN feedback, has been invoked as a mechanism to regulate the growth of the central black hole and to explain correlations seen between SMBH mass and host galaxy properties (see Fabian, 2012).

A composite image of the Centaurus A galaxy[7] is included in Figure 1.10. The image shows large-scale jets and outflows from the AGN in radio and X-ray bands, while the optical image captures starlight and dust emission, in addition to a contribution from the AGN in the central region.

## 1.2.3 Classification

The history of AGN classification and attempts to explain various subclasses in terms of a few physical parameters is very long and convoluted. For the current state of AGN unification efforts and details of non-jetted AGN classification see a recent review

---

[7] Credit: chandra.harvard.edu/photo/2008/cena

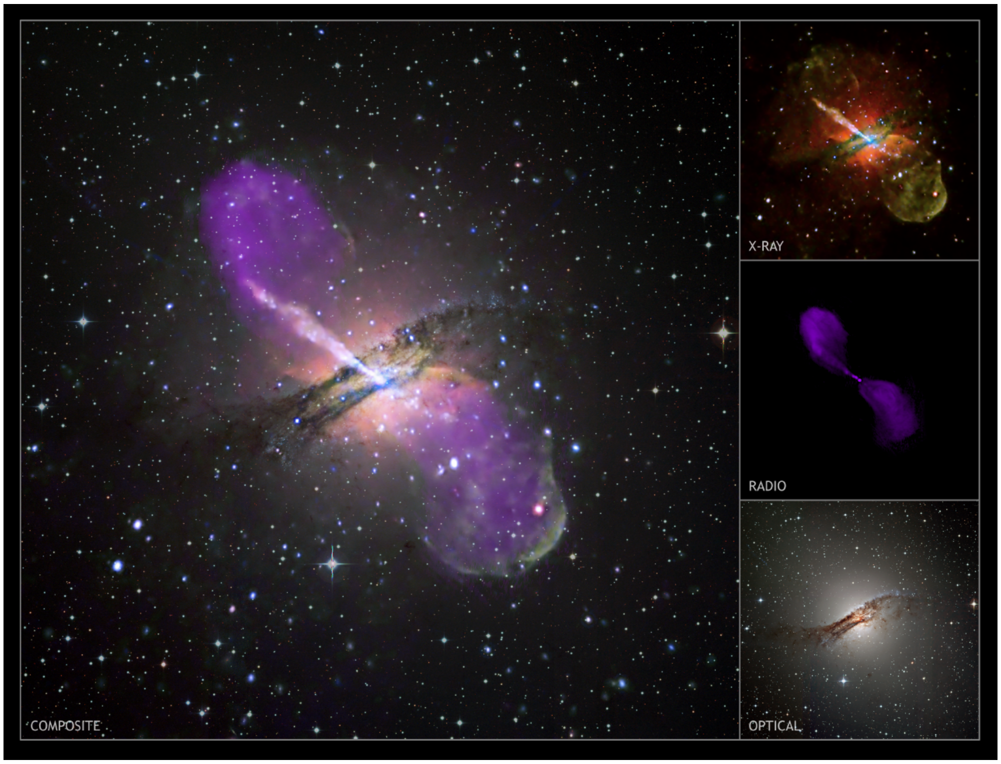

Figure 1.10: *Left*: Composite image of Centaurus A, showing the host galaxy, including the AGN and its extended jet. *Right*: *Chandra* X-ray, VLA radio, and ESO/WFI optical images of Centaurus A used for the composite image.

by Padovani et al. (2017). Here we address only a subsample of AGN classes known as jetted or radio-loud AGN.

Only a small fraction of AGN are jetted, although the exact fraction is still uncertain. Estimates from optically-selected AGN samples have found a jetted fraction ~15% (e.g., Kellermann et al., 1989), while a more recent estimate based on radio luminosity functions of AGN quoted $< 1\%$ (Padovani, 2011).

An early radio classification attempt of jetted AGN divided them into two morphological subclasses, known as Fanaroff-Riley type I (FR I) and type II (FR II) galaxies (Fanaroff & Riley, 1974). The division was based on the ratio of the distance between brightest regions on ether sides of the core and the size of the source, where FR I galaxies are core-dominated, while FR II galaxies are dominated by the extended radio lobe emission. As an example, Centaurus A in Figure 1.10 is an FR II galaxy.

The initial and largely successful idea behind the AGN unification effort has been to attribute the differences between AGN subclasses to orientation effects (Antonucci, 1993; Urry & Padovani, 1995).

This thesis is focused exclusively on blazars, a type of jetted AGN, in which the relativistic jet is closely aligned ($< 15^\circ$) with our line of sight.

## 1.3 Blazars

Blazars exhibit rapid variability, high luminosities, and superluminal motion, which are consequences of beamed emission from bulk relativistic motion of plasma along the jet (Blandford & Rees, 1978; Urry & Padovani, 1995). The beamed emission is largely responsible for this subclass of AGN to be the primary extragalactic sources detected in VHE gamma rays (68 out of 72 AGN). Blazars similarly dominate the HE gamma-ray sky observed by *Fermi*-LAT (Acero et al., 2015).

The blazar class is divided into BL Lac objects (or BL Lacs) and flat spectrum radio quasars (FSRQs). The initial division between FSRQs and BL Lacs was the presence or lack of strong optical emission lines, respectively (e.g., Stickel et al., 1991). Today, they are distinguished by their accretion rates or jet powers, with higher accretion rate FSRQs and lower-power BL Lacs (e.g., Massaro et al., 2009).

BL Lacs are in turn categorized by the location of the synchrotron emission peak into low ($< 10^{14}$ Hz), intermediate ($10^{14}$–$10^{15}$ Hz), and high ($> 10^{15}$ Hz) synchrotron-peak BL Lacs (LBL, IBL, and HBL, respectively) (Padovani & Giommi, 1995).

There are a large number of open questions in our understanding of blazars. The emission mechanisms responsible for the non-thermal blazar SEDs and their locations, the role of hadronic emission, and physical explanations for the various blazar subclasses are all under active investigation. Moreover, the exact jet-launching mechanism is still uncertain, including mechanisms for acceleration and collimation of plasma within jets (Romero et al., 2017).

Gamma-ray observations of blazars, especially when combined with observations from other bands and input from theoretical models can be used to answer these questions. Timing and spectral analyses are especially useful for exploring blazar emission and will be widely used throughout this thesis.

### 1.3.1 The Blazar Jet

The emission from blazars is dominated by the relativistic jet. A basic structure for an AGN jet is depicted by a schematic in 1.11. The jet consists of relativistic plasma with bulk motion close to the speed of light, accelerated and collimated by strong, helical magnetic fields (~mG at pc scales to ~10 G at 10 mpc scales; see Martí-Vidal et al., 2015). The plasma trapped inside the jet can develop both standing and moving shocks, which can act as sites of particle acceleration and dominate emission in parts of the blazar SED.

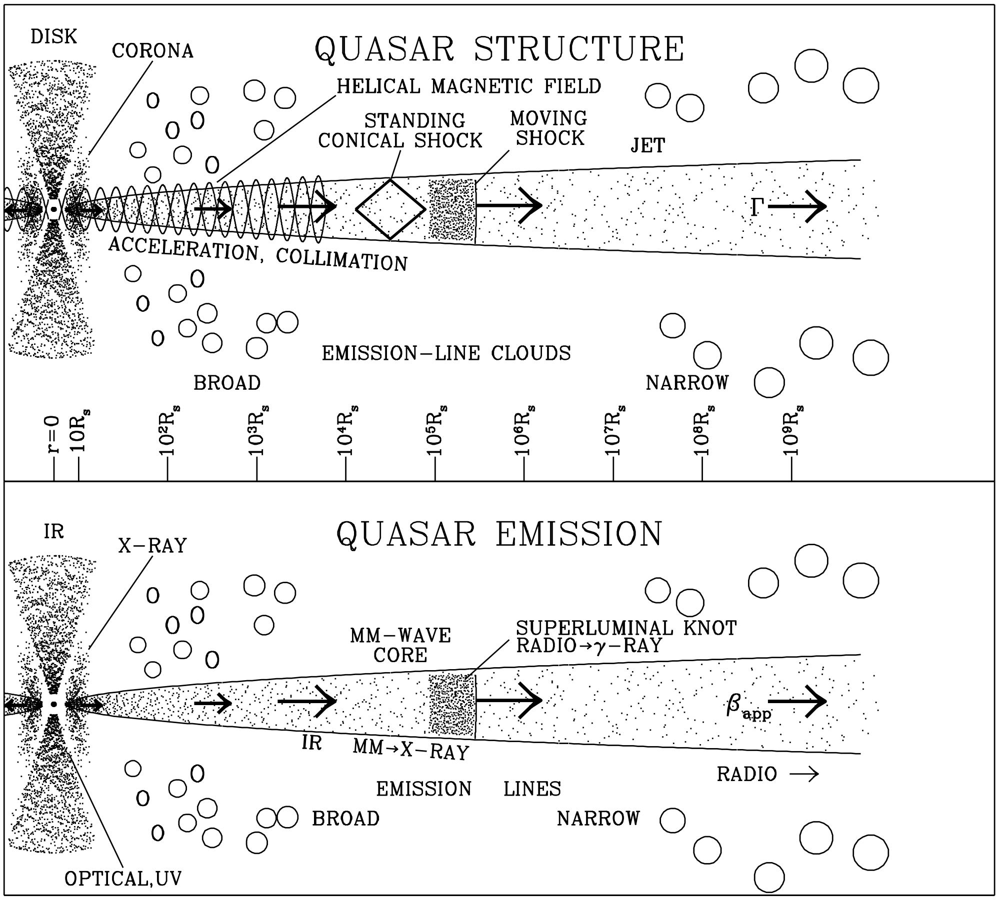

Figure 1.11: Cartoon of composition and emission of an AGN with a relativistic jet (from Marscher (2009)). The length scales are provided in terms of Schwarzschild radii of the black hole.

The exact composition of the jet plasma is not well established. Both leptons and hadrons are expected to be present in AGN jets; however, their respective contribution to gamma-ray production likely differs for different sources (e.g., Böttcher et al., 2013).

There are two proposed mechanisms for launching the relativistic jets. Under the first scenario, power and angular momentum are extracted from the rotational energy of a *Kerr* black hole through a "frame dragging" of magnetic fields to generate jet-like outflows (Blandford & Znajek, 1977). The second mechanism is powered by the accretion disk, with angular momentum magnetically removed from the disk to launch jets perpendicular to the plane of the accretion disk (Blandford & Payne, 1982).

### 1.3.2 Particle Acceleration Mechanisms

High luminosities and short variability timescales observed in blazars require efficient particle acceleration mechanisms within their jets. Fermi acceleration mechanisms (Fermi, 1949), based on energy gains of relativistic particles from scattering off turbulent magnetic structures, have been widely used in astrophysical contexts.

First-order Fermi acceleration or diffusive shock acceleration is one of the most efficient mechanisms for particle acceleration in blazar jets. The mechanism involves collisions of relativistic particles with a shock moving through the jet.

During a collision, a particle can gain (lose) energy if the shock, or in a more general case a scattering magnetic structure, is moving in the opposite (same) direction with respect to the direction of motion of the particle. The change in energy during a collision can be expressed by,

$$\frac{\Delta E}{E} = -\frac{2\boldsymbol{v}_s \cdot \boldsymbol{p}}{E} = -\frac{2\boldsymbol{v}_s \cdot \boldsymbol{v}}{c^2}, \tag{1.24}$$

where $E$ is the particle energy, $\Delta E$ is the change in energy, $\boldsymbol{v}_s$ is the shock velocity, and $\boldsymbol{v}$ and $\boldsymbol{p}$ are the particle velocity and momentum. For isotropic incidence, the average energy gain for a particle with an energy $E$ undergoing head-on collisions (opposite shock and particle velocities) is,

$$\frac{\langle \Delta E \rangle}{E} = \frac{4}{3}\left(\frac{v_s}{c}\right)\left(\frac{v}{c}\right). \tag{1.25}$$

As expected, the head-on collisions result in energy gains. For collisions with the same particle and shock directions, the right-hand side of the Equation 1.25 becomes negative and energy is lost. For relativistic particles ($v \to c$) The rate of energy gain can then be expressed as,

$$\frac{\dot{E}}{E} = \frac{\langle \Delta E \rangle}{E \delta t} = \frac{4}{3}\left(\frac{v_s}{c}\right)\left(\frac{1}{\delta t}\right), \tag{1.26}$$

where $\delta t$ is the time between collisions and can be defined as,

$$\delta t = \frac{L}{v(1 \pm \frac{v_s}{v})}, \tag{1.27}$$

with L as the mean free path of the collisions and + sign corresponds to head-on collisions. Near the shock boundary, collisions become almost entirely head-on and the acceleration is highly efficient. This is the scenario for first-order Fermi acceleration and Equation 1.26 gives the rate of energy gain for it. Knots observed in AGN jets are shocked regions and could facilitate particle acceleration with this scenario (Rieger et al., 2007).

If no strong shocks are present and collisions of particles occur stochastically with turbulent magnetic structures, energy can still be gained on average, as the time between collisions is much shorter for head-on collisions than for receding collisions, indicated by Equation 1.27. For an additional condition of $v_s/v \ll 1$, the rate of energy change in this scenario, known as second-order Fermi acceleration can be written as,

$$\frac{\dot{E}}{E} = \frac{\langle \Delta E \rangle}{E \delta t} = \frac{4}{3}\left(\frac{v_s}{c}\right)^2\left(\frac{1}{\delta t}\right). \tag{1.28}$$

The first- and second-order refer to the rate of the energy gain being proportional linearly or quadratically to the speed of the shock or magnetic structures. The timescale for these mechanisms, $\tau_{acc}$ can be estimated with $\tau_{acc} = E/(\dot{E})$. Thus, $\tau_{acc} \propto v_s^{-1}$ for first-order and $\tau_{acc} \propto v_s^{-2}$ for second-order Fermi acceleration. Since, $v_s$ for a first-order process is much greater than $v_s$ for second-order, the timescales for first-order Fermi acceleration are much shorter than the timescales for second-order Fermi acceleration. On the other hand, second-order processes can produce harder particle spectra ($p < 2$) than first-order Fermi ($p > 2$). Second-order Fermi acceleration is favored for explaining emission from regions between knots in AGN jets (Rieger et al., 2007).

An alternative acceleration mechanism that has been gaining popularity for explaining observed rapid variability from blazar jets is magnetic reconnection. This mechanism has long been favored for explaining Solar phenomena, such as Solar flares and coronal mass ejections. Magnetic reconnection can occur when magnetic field loops with opposite directions are brought very close to each other by motions of the plasma currents supporting the fields. The interactions of the plasma currents can annihilate the field loops. The result is a topological change in the magnetic fields from a higher-energy configuration to a lower-energy one, with excess energy deposited into the plasma and particle acceleration (e.g., Boettcher et al., 2012).

Based on relativistic magnetic reconnection simulations, reconnection in blazar jets can likely occur at the base of the jet, near the accretion disk. This acceleration mechanism predicts very hard particle populations with power-law index, $p \rightarrow 1$. In addition, the acceleration occurs very rapidly and can explain observations of variability on the timescale of minutes or shorter (Nalewajko, 2016). Finally, it is possible that both shock-driven and magnetic reconnection acceleration mechanisms occur in blazar jets, with magnetic reconnection accelerating the seed electrons for shock acceleration (Boettcher et al., 2012). Other acceleration mechanisms not discussed in this section have been proposed for blazar jets, such as the converter process and shear acceleration (see e.g., Tammi & Duffy, 2009).

### 1.3.3 Blazar Emission

The blazar emission is best characterized by its SED, which consists of two characteristic humps (see *jet* curves in Figure 1.9). The lower energy hump is established to be synchrotron emission from relativistic electrons. The higher energy, gamma-ray hump is believed to be from inverse-Compton scattering of photons on the same population of relativistic electrons, although the exact emission mechanisms might vary from source to source. Emission from hadrons is an appealing alternative, as it would make blazars likely candidates for sources of cosmic-rays and astrophysical neutrinos.

Blazars are known to exhibit high levels of polarized emission. Radio, including very long baseline interferometry (VLBI) observations of blazars, indicate that the linear polarization can range from few percent in cores up to $\sim$50% in extended jets; while circular polarization is $< 1\%$ – a sign of incoherent synchrotron radiation (Marscher, 2009).

### 1.3.4 Emission Models

One of the most widely used models for blazar emission, relies on a mechanism known as synchrotron self-Compton (SSC) (Jones et al., 1974),which represents the lower energy emission hump of the blazar SED with synchrotron radiation from a population of relativistic electrons and the gamma-ray hump with inverse-Compton upscattering of the synchrotron photons on the same population of electrons. In the simplest realization of these models, the emission is limited to a single, spherical region (often called a *blob*) filled with homogenous, tangled magnetic fields and a stationary electron population, with the region moving towards the observer with some Doppler factor (e.g., Konigl, 1981; Tavecchio et al., 1998).

More complicated SSC models, largely motivated by observations difficult to explain with the one-zone SSC model, rely on the presence of multiple emitting regions or jet structures. These include models with a slow jet component in front of a fast jet base (Georganopoulos & Kazanas, 2003), a jet composed of a fast spine embedded in a slower layer (Ghisellini et al., 2005), or a small spherical acceleration region embedded in a much larger emitting region (e.g., Chen et al., 2015).

SSC models are very successful for describing HBL SEDs both in average-flux states or during rapid flares. FSRQs, LBLs and IBLs, on the other hand, with their high Compton dominance, require external radiation fields. A family of models known as external-inverse-Compton (EIC) can effectively model these objects. EIC models use a similar emission region as SSC models; however, they include an additional photon field from the accretion disk, the broad-line region, or the dusty torus that can be upscattered on the electron population (e.g., Sikora et al., 1994).

As an alternative to the SSC and EIC leptonic models, the gamma-ray hump can be modeled by emission from hadronic interactions (*lepto-hadronic* or *hadronic* models), namely pion production from proton-photon interactions along with secondary EM cascades and synchrotron radiation from protons (e.g., Mücke & Protheroe, 2001; Mücke et al., 2003; Cerruti et al., 2015). The former is efficient for higher plasma densities, whereas the latter becomes significant in the strong magnetic field regime.

### 1.3.5 Blazar Unification

Fossati et al. (1998) initially attempted to unify the blazar classes with an anti-correlation between the frequency and the luminosity of the synchrotron peak. A "blazar sequence" was proposed, in which FSRQs would occupy the lowest peak frequency and highest power end, while the HBLs would reside in the lowest power, highest frequency end (with IBLs and LBLs in between).

The blazar sequence was later justified in terms of two physical parameters, the mass of the black hole and the accretion rate (Ghisellini & Tavecchio, 2008). The blazars at the HBL end of the sequence would have low accretion rates and consequently exhibit radiatively inefficient accretion disks (no strong emission lines), while blazars at the FSRQ end, with the high accretion rates and power would have radiatively efficient disks (strong emission lines).

With the addition of more observations and inclusion of non-blazar radio galaxies, (Meyer et al., 2011) found the blazar sequence to be insufficient and argued for a "blazar envelope," which encompasses two physically distinct jetted-AGN populations with varying degrees of jet alignment with the line of sight. Meyer et al. (2011) related the two populations to jet structure, with (1) a population of simpler, "non-decelerating" or "strong" jets describable by a single Lorentz factor and encompassing blazars with synchrotron peaks below $\sim 10^{14}$ Hz, and (2) a population of "decelerating" or "weak" jets with multiple emitting regions of varying speeds described by models such as the spine-layer model (Ghisellini et al., 2005) or the decelerating jet model (Georganopoulos & Kazanas, 2003).

In addition to the synchrotron peak-luminosity relationship, another observable that has been used to unify blazar sub-classes is Compton dominance, defined as the ratio of the peak of the gamma-ray hump to the peak of the synchrotron hump. Compton dominance is a redshift-independent quantity and as such is immune to selection effects. Finke (2013) found a correlation between Compton dominance and the synchrotron peak frequency and argued for a model that explains the differences between FSRQs and BL Lacs in terms of the magnetic field strength of the emission region, the energy density of the external radiation field, and the angle of alignment of the jet. In this model, FSRQ-like objects fall in the strong magnetic field strength and high external radiation field density regime, while objects resembling BL Lacs occupy the weak magnetic field and low external photon density regime.

### 1.3.6 Variability

Variability is a defining feature of blazars. In the study of blazars, flux and spectral variability are one of the most informative observables available, especially in bands with poor angular resolution and when observed in coordinated multi-band campaigns.

Blazars have been known to vary at all accessible wavelengths and on a wide range of timescales from minutes (e.g., 3C 279 (Ackermann et al., 2016b), PKS 2155-305: (H.E.S.S. Collaboration et al., 2010), Mrk 421: Chapter 4) to years (e.g., 1ES 0229+200 (Cologna et al., 2015), PG 1553+113: Chapter 6). The amplitude and the timescale of variations in blazars is energy dependent. The larger amplitudes and shorter timescales are observed for variations at the higher-energy ends of the SED humps (past the peaks), associated with the higher-energy particle populations with faster cooling timescales (Boettcher, 2012). For HBLs, this rapid, high-amplitude variability regime falls in X-ray and VHE gamma-ray energies, whereas for LBLs and FSRQs this regime is in the optical and HE gamma-ray bands. The variable emission from blazars appears to be stochastic in nature and can be described by power spectral densities (PSDs) following power-law functional shapes (e.g., Finke & Becker, 2015).

Correlated variability between VHE-gamma rays (probing the gamma-ray hump) and lower-energy bands (sampling the synchrotron hump) have been found during blazar flaring episodes (e.g., Buckley et al., 1996; Catanese et al., 1997; Aharonian et al., 2009; Fossati et al., 2004, 2008). Such variability patterns are strong indicators of and are successfully modeled by an SCC-type emission. In addition, time lags have been observed in cross-correlations of gamma-rays with lower-energy bands. Cohen et al. (2014) saw time lags of $-40$ to $+30$ days between optical and gamma-ray light curves of blazars, with gamma rays leading the optical for positive lags. On similar timescales, Max-Moerbeck et al. (2014) found radio emission lagging gamma-rays for a number of blazars, invoking a scenario in which the gamma-ray emission region is separated and upstream of the radio emission region to explain the lag. Ramakrishnan et al. (2015) found 26 blazars with radio lagging gamma rays in all but 2 sources and explained the lag in terms of a distance traveled by the emitting region.

On the other hand, major gamma-ray flares have been observed with no obvious activity in X-rays (e.g., 1ES 1959+650 in 2002 (Holder et al., 2003; Krawczynski et al., 2004; Daniel et al., 2005)). Known as "orphan flares," these events pose a considerable challenge for theoretical models, especially models that relate the gamma-ray emission to the synchrotron hump (e.g., SSC, EIC). Multi-zone SSC models (e.g., Krawczynski et al., 2004) and hadronic models with separated emitting regions (e.g., Böttcher, 2005) have been proposed to explain these flares. The reverse scenario, known as "childless" flares, in which no VHE gamma-ray flare occurs during a large X-ray flare have also been observed (e.g., Gliozzi et al., 2006).

Flux variability is sometimes observed along with spectral variability, in some cases exhibiting a spectral hysteresis primarily observed in X-rays (e.g., Sembay et al., 1993; Kataoka et al., 2000; Catanese & Sambruna, 2000; Cui, 2004; Falcone et al., 2004; Abeysekara et al., 2017) – a loop-like pattern in a spectral index vs. flux representation. Spectral hysteresis is typically explained in terms of competing dynamical, acceleration, and radiative cooling timescales (Kirk et al., 1998; Böttcher & Chiang, 2002).

The blazar variability timescale can be used to place a limit on the size of the emission region, with $R_e \lesssim t_{var} c\delta/(1+z)$. Here $R_e$ is the radius of the emitting region, $t_{var}$ is the variability timescale, z is the redshift, and $\delta$ is the Doppler factor. Combined with an assumption that the emitting region fills the full width of a conical jet, the limit on the size has also been used to estimate the distance of the emitting region from the central black hole (e.g, Aleksić et al., 2011). Very rapid variability observed primarily in VHE gamma rays with timescales of minutes has presented a significant challenge for emission models. It suggests an emission region very close to the black hole and in some cases, a region smaller than the Schwarzschild radius. In addition, in order for gamma rays to escape the emission region instead of pair-producing with lower-energy photons, the bulk Lorentz factor is required to be $\Gamma \sim 50$ (Begelman et al., 2008). This value is much higher than VLBI measurements of the bulk Lorentz factor with superluminal motions in blazar jets (Piner & Edwards, 2004). Structured jet models discussed in Section 1.3.4 can overcome this difficulty with regions of different Doppler factors.

Lack of observed variability or variability on very long timescales can be informative as well. Due to the slower cooling timescales of protons compared to leptons, the more stable blazars have been attractive candidates for hadronic emission models (e.g., Cerruti et al., 2015). In addition these blazars have also been targeted as candidates for a proposed $\gamma$-ray emission mechanism in which at least a component of the observed VHE gamma-ray emission originates from ultra-high-energy cosmic rays (UHECRs) that propagate a large fraction of the source distance before producing electromagnetic cascades, including gamma rays along the line of sight (Ferrigno et al., 2004; Bonnoli et al., 2015; Essey & Kusenko, 2010).

The remainder of this thesis is organized as follows. Chapter 2 describes the VERITAS instrument and data analysis. Chapter 3 presents first an identification of and then an in-depth study of an unusually stable extreme blazar, HESS J1943+213, followed by an investigation of a possible UHECR-generated gamma-ray contribution to the emission of a distant blazar, PKS 1424+240. Chapter 4 details the analysis of VERITAS observations of a giant and rapid flaring event from the blazar, Mrk 421, including timing analyses applied to the VERITAS and optical data. Chapter 5 presents the VERITAS detection and multi-wavelength investigation of an HBL, MS 1221.8+2452 during a flare in which the source exhibits a spectral hysteresis in X-rays. Chapter 6 gives an account of long-term VERITAS observations of PG 1553+113 and a VHE gamma-ray search for periodic modulations. Chapter 7 concludes with a summary of the research presented in this thesis.

# Chapter 2

# VERITAS

Figure 2.1: True-to-life painting of VERITAS. ©Trevor Weekes

The Very Energetic Radiation Imaging Telescope Array System (VERITAS) is an Imaging Atmospheric Cherenkov Telescope (IACT) array located at the Fred Lawrence Whipple Observatory (FLWO) in Southern Arizona (31° 40′ N, 110° 57′ W), at an altitude of 1268 m above sea level. VERITAS is one of three leading, current (3rd) generation IACT arrays dedicated to gamma-ray astrophysics.

The multi-national VERITAS Collaboration (over 80 members from four countries) maintains and operates the VERITAS array and has proprietary access to all data from VERITAS observations.

## 2.1 Hardware

The VERITAS array consists of four 12-m telescopes arranged in a roughly parallelogram configuration since Summer, 2009. The initial configuration of the array, which became fully operational in early 2007 had Telescope 1 (T1) positioned in a sub-optimal location, such that the overlap of T1 and T4 atmospheric shower images led to a reduced effective area. The move of T1 (see Figure 2.2) provided ∼15% improvement in sensitivity. The baselines of the telescopes are now ∼100 m.

### 2.1.1 Telescope Body and Mirror

The body of an individual telescope includes the positioner that allows altitude-azimuth motion and the optical support structure (OSS) mounted on the positioner. A custom tracking software is used to control the motions of the telescopes. The telescopes are equipped with tracking motors, which account for the rotation of the Earth, allowing stable pointing in the direction of a celestial object. In addition, the VERITAS Pointing Monitor (VPM) system delivers arcsecond precision pointing for each telescope using real-time star position measurements. The VPM is an optical monitoring system consisting of two CCD cameras (a sky camera and a focal plane camera), a control computer, and LEDs on the sides of each of the cameras.

The mirror of each telescope follows a Davies-Cotton design (Davies & Cotton, 1957), using hexagonal glass mirror facets with widths of 61 cm to compose a spherical surface. There are 345 facets arranged on the OSS of each telescope, producing a surface with an area of 110 $m^2$ and 24 m radius of curvature (see Figure 2.3). The mirrors had a

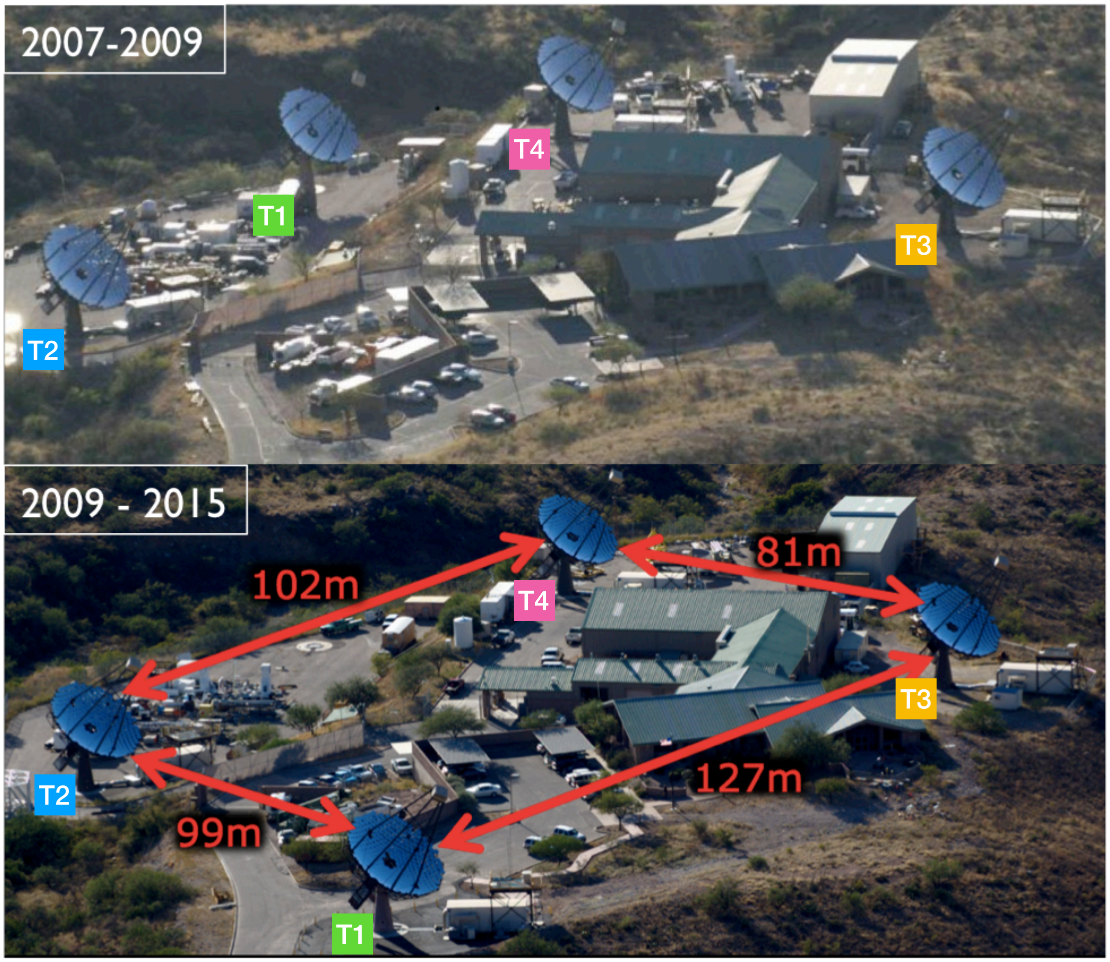

Figure 2.2: The layout of VERITAS array before (*top*) and after (*bottom*) the T1 move.

peak reflectivity of ∼94% at 310 nm when first coated, but have degraded to an average peak reflectivity of ∼87% at 380 nm. The mirrors are periodically washed to restore reflectivity lost to accumulation of dust and dirt.

### 2.1.2 Camera

The camera on each telescope is composed of 499 photo-multiplier tubes (PMTs) (shown in Figure 2.5), covering a field of view of 3.5°. A PMT uses a photocathode that can absorb photons and release electrons (photoelectrons). By applying high voltage, the photoelectrons are directed into a chain of dynodes that multiply them and create an

Figure 2.3: VERITAS Telescope 2 mirror (*left*) and an individual mirror facet (*right*).

electron cascade, which is then fed into an anode. The current measured in a PMT is linearly proportional to the photon flux over a large range of fluxes. For very high photon fluxes, however, a PMT can become saturated resulting in a nonlinear relationship between measured current and incoming photon flux.

A plate containing *Winston cones* for each PMT is placed in front of the camera, to reduce light loss due to space between PMTs. The cones act as light funnels that direct light into PMTs that would otherwise fall between them.

The choice of PMTs as camera pixels are largely motivated by the nanosecond response speed of these detectors. The original cameras were fitted with Photonis PMTs, which were upgraded to Hamamatsu PMTs in the summer of 2012, providing significant improvements in sensitivity especially for lower energy events and softer sources (by as much as 40%). The quantum efficiency for the newer Hamamtsu PMTs peaks at ~43% between 370 nm and 430 nm, while the original Photonis PMTs had a peak quantum efficiency of ~23% (D. B. Kieda for the VERITAS Collaboration, 2013).

High voltage of ~1000 V (but ranging between 800 V and 1100 V) is applied to each PMT. The voltage determines the PMT gain, i.e. the conversion rate between a single photoelectron produced by the photocathode and the number of electrons in the electron cascade after the last dynode. To ensure a uniform response for the camera, the high voltage for each PMT is tuned to produce the same gain of $\sim 2\times10^5$.

A preamplifier is used for each PMT to amplify their outgoing signal by a factor of 6.6. This is necessary to feed the signal into electronics trailers below each telescope using 45 m cables with impedance of 75 $\Omega$.

The signal from each PMT is split into two: one copy of the signal is sent to the flash-analog-to-digital converters (FADCs), while the other goes to the trigger system.

### 2.1.3 FADCs

The 8-bit FADCs are located in the electronics trailers and sample the charge on each PMT with a 500 MHz rate (i.e., each sample is 2 ns). The PMT signal is converted into digital count (DC) values, where 1 DC corresponds to a PMT signal of 7.81 mV. FADCs store the PMT signal in a buffer with a width of 32 $\mu$s until a trigger is received to record the signal. During normal observations, VERITAS records a readout window covering 48 ns from each channel.

FADCs are operated under either high or low gain modes and include a gain switch. In the high gain mode, signal is converted to digital counts between 0 and 255. If, however, the PMT accumulates enough charge to exceed 255 digital counts, the FADC delays and reroutes the signal to a low-gain channel with a range of 1500 digital counts. This 2-gain system provides a large dynamic range, with both a sensitivity to low photon fluxes and a guard against FADC count saturation for high photon fluxes.

The Cherenkov light produces a pulse in the FADC readout that can be used to identify and characterize it when combined with information from multiple channels (see Figure 2.4).

### 2.1.4 Trigger System

VERITAS relies on a 3-level trigger system for filtering data at the hardware level. The level one trigger (L1) is associated with an individual FADC channel constant fraction discriminator (CFD) crossing a threshold, implying the PMT has been exposed

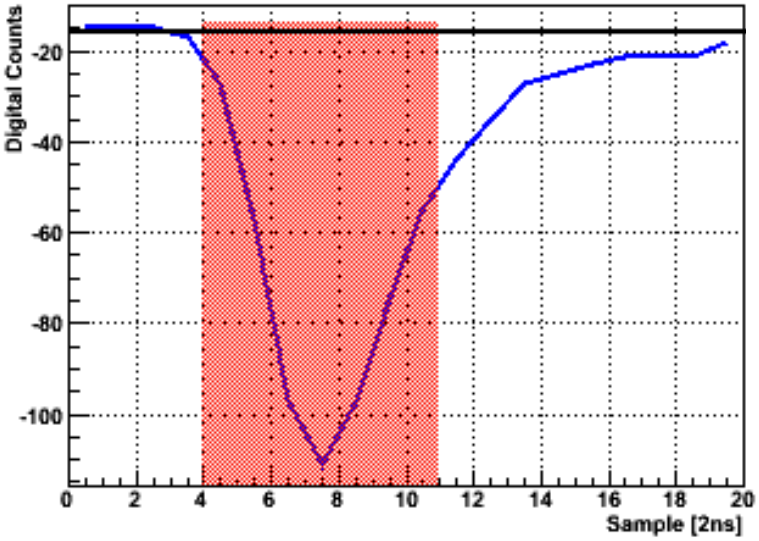

Figure 2.4: An FADC trace, showing a pulse from Cherenkov light.

to sufficient light to be considered bright. For dark time observations, a CFD of 45 mV is used, which along with the high voltage applied to the PMTs is adjusted for different moonlight conditions.

The level two trigger, L2 operates at the level of an individual telescope camera and is activated when a number of adjacent pixels are bright and have triggered L1. The L2 is a pattern trigger and filters out potential events from random fluctuations in the night sky background (NSB). If not filtered, the L1 triggers from NSB fluctuations can overwhelm the system and make the detection of Cherenkov showers very difficult. At least three adjacent triggered pixels are required within a coincidence time window of 6 ns to fire the L2 trigger.

L2 triggers from at least two telescopes within a 50 ns window activate the level three trigger (L3). L3 is an array-level trigger, intended to increase the reliability of events and to eliminate local events, especially those from muons. Muons interact deep in the atmosphere and can produce images resembling gamma rays, but usually appear in a single telescope. Hence, they can be efficiently rejected with the L3 system.

Once the L3 is triggered, the array enters readout mode, during which no events are recorded. This is the main contributor to "deadtime" for VERITAS exposures (exposure

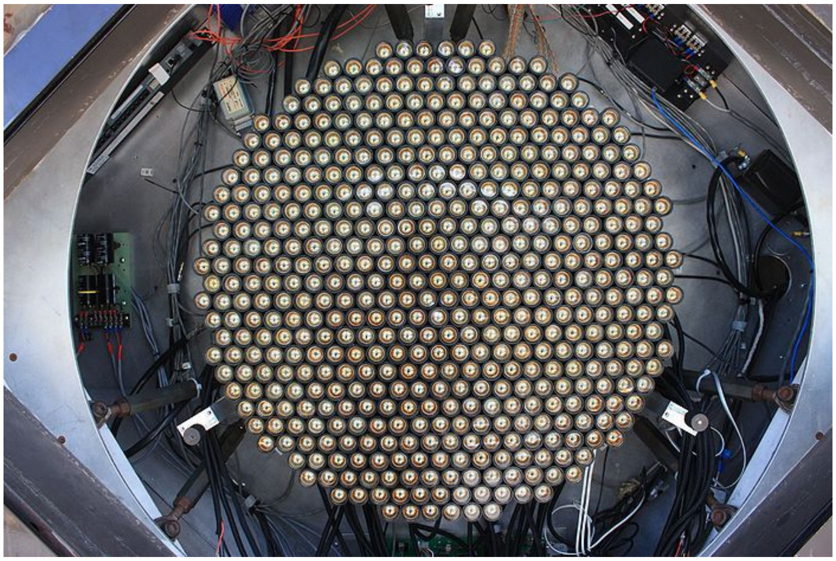

Figure 2.5: VERITAS camera shortly after the upgrade.

time = livetime + deadtime), which for the upgraded array is ∼13% (∼8% before the camera upgrade). The higher deadtime with the upgraded camera is due to a higher L3 trigger rate from the more sensitive PMTs.

### 2.1.5 VERITAS Data Acquisition

VERITAS uses VME (VERSA-Module Euro) Data Acquisition (VDAQ) system for recording data. A visual representation of VDAQ components is provided in Figure 2.6.

After an L3 trigger, the VERITAS DAQ reads out the buffers of FADCs associated with each telescope. The system responsible for storing FADC traces for individual telescopes is called Event Builder (one for each telescope). The Event Builders package the FADC traces with other information from the L3 system, including the telescope number, the event number (associated with each L3 trigger), the GPS timestamps for every telescope, and a telescope participation flag into a single-telescope *event*. The Event Builders both store the events locally and send them to the Harvester system.

Harvester is responsible for constructing the final array events from the Event Builder and L3 data, storing the array events on disk, and transferring the data to a dedicated archive machine. In addition, a program on Harvester called QuickLook performs a real-time simple analysis of the data, producing diagnostics information and, when applicable, an estimate of the detection significance of the targeted source.

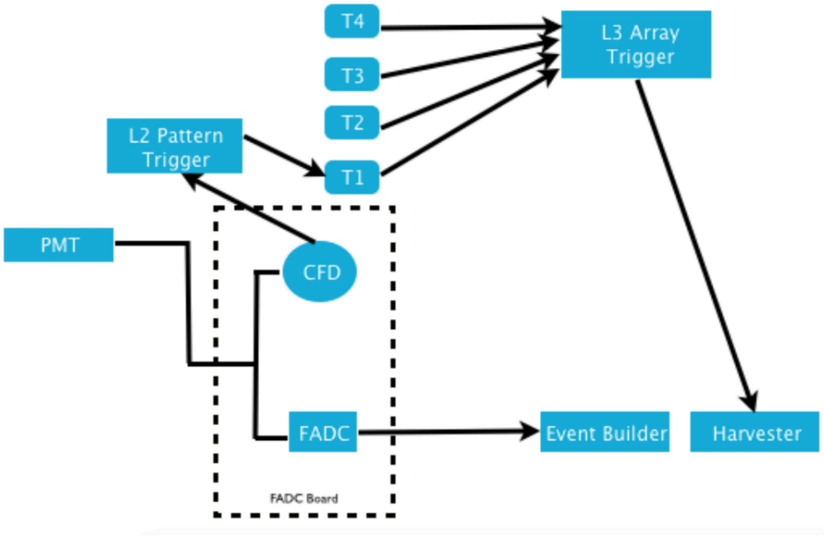

Figure 2.6: Primary components of the VERITAS DAQ from Madhavan (2013).

## 2.2 Operation

With a 3.5° field of view, VERITAS is a narrow-field gamma-ray instrument and makes primarily targeted observations. VERITAS is used in sky-survey mode as well, to image the Cygnus region (5° × 15°) of the Galactic plane (e.g., Krause & the VERITAS Collaboration, 2017).

### 2.2.1 Observing Modes

The main observing mode for VERITAS, known as "wobble", places the tracking position or center of the field of view at an offset from the target position (typically, by 0.5°) towards one of the cardinal directions, with changing offset directions (N, E, S, W) for successive exposures. Wobble mode observations provide target and background coverage with comparable acceptance - the probability of accepting a gamma-ray-like event at a given position in the field of view - crucial for spectral reconstruction.

An alternative “On-Off” observing mode is used for a smaller subset of targets, during which exposures are alternated between a field of view centered on the target and a background field. This mode is necessary for extended targets, especially targets that subtend an angular size comprising a large fraction of the field of view.

### 2.2.2 Calibration Observations

Calibration observations and measurements are made regularly as part of VERITAS operations. Calibrations fall into two rough categories: bi-weekly or monthly calibrations that track and tune the VERITAS hardware and nightly calibration observations sensitive to nightly changes in the performance of the cameras due to changes in environmental conditions or minor hardware tweaks.

Nightly calibration observations employ a “flasher” system composed of 6 LED lights (formerly a laser) that uniformly illuminates the camera. The light intensity is varied during the course of this calibration observation by using different numbers of LEDs (0 – 7) for successive flashes (Hanna et al., 2010). The flasher observations measure and calibrate the relative gains and timing offsets between camera pixels.

The main bi-weekly or monthly calibrations include whole-dish reflectivity measurements for each of the telescopes, single photo-electron measurements for calibrating absolute gains, High-Low gain calibration, pointing monitor system calibration, and measurement of on-axis PSF. This list is not exhaustive. At the beginning of each observing season, in particular, an array of other calibrations are made to return the VERITAS hardware to its standard operating parameters.

### 2.2.3 Conditions for Operation

VERITAS mostly observes under clear, dark skies. Very cloudy or rainy conditions make observations impossible; however, VERITAS can operate with some cloud cover (known as “filler observations” ), data from which is unreliable but is used to search for gamma-ray flaring activity, primarily from blazars.

Observations are possible under moderate moonlight, when the moon is less than half illuminated. When the moon illumination is above ~35% (but typically below ~65%) and when currents on the camera exceed 15 $\mu$A, observations are taken with lowered voltages on the PMTs - known as reduced high voltage (RHV) mode. Brighter moonlight raises the level of NSB, consequently increasing the current on the exposed PMTs, the trigger rates, and deadtime. Lowering the PMT voltage in the RHV mode counteracts this effect, while retaining sensitivity by also lowering the CFD threshold to ~25 mV. The cost of this mode is reduced sensitivity to fainter, primarily lower energy Cherenkov showers. The observatory shuts down for ~6 days every month around full moon.

Between 2011-12-15 and 2014-12-31, VERITAS also observed under bright moonlight using a plate composed of neutral density filters for each pixel, which reduced the down time of the observatory to only 3 days around full moon. The filters have a similar (but a larger-magnitude) effect and consequences to lowering voltage. Fainter, lower-energy showers are preferentially missed. The RHV mode raises the minimum energy event that can be reliably reconstructed by ~50 GeV, while use of filters raises the minimum energy by hundreds of GeV.

The VERITAS observatory shuts down during the months of July and August. The monsoon conditions over this period make operation impossible.

## 2.3 Performance

VERITAS can reliably detect gamma rays with energies between 85 GeV and >30 TeV, with spectral reconstruction starting at 100 GeV (for dark-time observing). The lower energy limit is determined by the ability of individual telescopes/cameras to detect faint showers, while the higher energy limit is given by the ground area coverage of the array. The energy resolution of VERITAS is set by the degeneracy between the energy of the primary gamma ray and the depth of its first interaction in the atmosphere. At 1 TeV, the energy resolution is 17% (ranging between 15% and 20%) and the peak effective area is 100,000 $\mathrm{m}^2$ (see Figure 2.7).

VERITAS works best for sources at high elevation angles: For observations made below 60° elevation, IACTs have significantly reduced sensitivity and higher low-energy thresholds. This limits most VERITAS targets to declinations 0° to +60°; exceptions

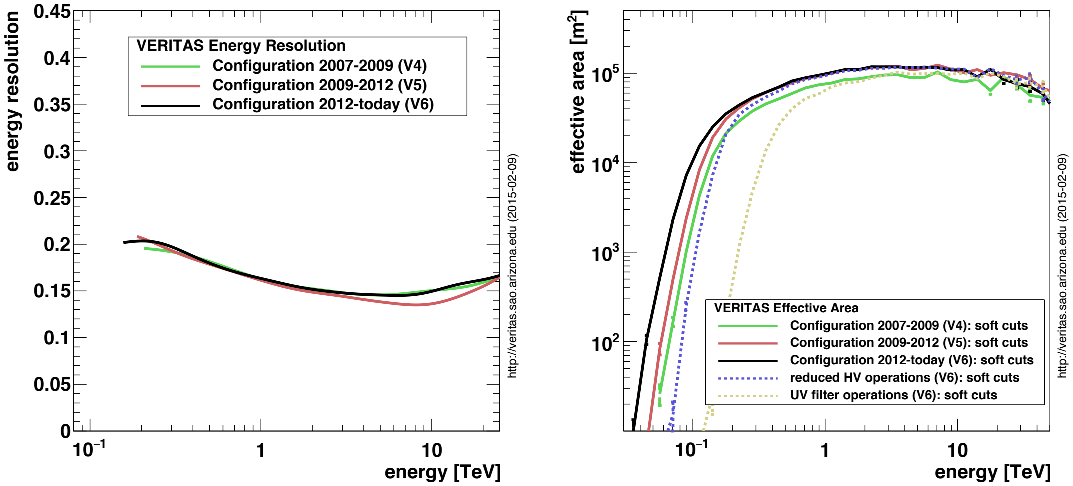

Figure 2.7: *Left*: Energy resolution of VERITAS for different configurations. *Right*: Effective area curves for the different VERITAS configurations.

Table 2.1. Summary of VERITAS performance specifications.

| | |
|---|---|
| energy resolution | 17% at 1 TeV |
| peak effective area | 100,000 m$^2$ |
| angular resolution | 0.08° at 1 TeV, 0.13° at 200 GeV (68% values) |
| source location accuracy | 50 arcseconds |
| point source sensitivity | 1% Crab in < 25h, 10% in 25 min |
| observation time per year | 750 hours non-moonlight, 100 hours moonlight |

are made for particularly interesting targets slightly outside of this region (-10° to +70°).

Figure 2.8 shows the differential sensitivities for 50 hours of observations at 20° zenith angle. Sensitivity is defined as the minimum differential flux to reach a 5 sigma detection per energy bin (there are 5 bins per decade, equal bin sizes on log10 scale) and at least 10 signal events. VERITAS outperforms MAGIC and is comparable to HESS at > 200 GeV energies, despite having lower sensitivity at low energies and an overall higher low-energy threshold.

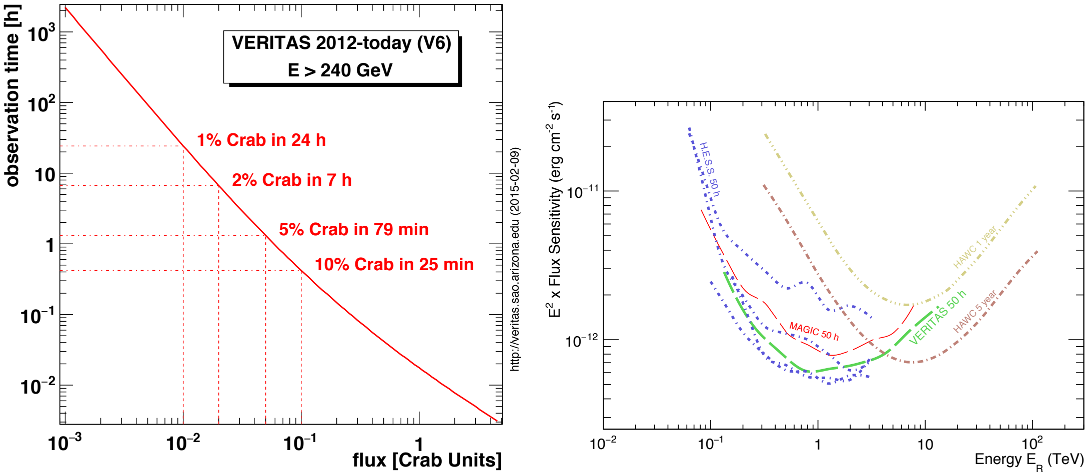

Figure 2.8: *Left*: Sensitivity of VERITAS, showing the time requirement for detection of sources with different brightnesses. *Right*: Comparison of differential sensitivities of gamma-ray observatories, including current-generation IACT arrays including VERITAS and the next-generation CTA. MAGIC points are from Aleksić et al. (2016). HESS curves: 4-telescopes HESS I, mono HESS II, and HESS I+HESS II stereo sensitivities (HESS sensitivities reaches higher energies than shown).

## 2.4 Data Analysis with `VEGAS`

The VERITAS data is stored in a specialized format known as VERITAS Bank Format (VBF), optimized for recording the low-level data products produced by VDAQ. VBF files store information from the detector associated with individual events, including FADC traces for each pixel, event arrival times, the number of participating telescopes, dead-time, array configuration, etc. There are two primary software packages for analyzing the VERITAS data: VERITAS Gamma-ray Analysis Suite (`VEGAS`) and Event Display (`ED`). The VERITAS Collaboration requires agreement between the two packages for analysis results before they are presented outside of the collaboration. Below is a description of the VERITAS data analysis with `VEGAS`. `ED` follows similar procedures.

One of the official analysis packages for VERITAS data, `VEGAS` is written almost entirely in `C++` with use of `CERN ROOT` libraries. Although `VEGAS` is not strictly a modular package, it is divided into separate stages (1, 2, 4, 5, 6) corresponding to steps in the data analysis. Stage 3 is omitted for superstitious reasons. The data analysis includes calculation and application of calibrations, measurement of image parameters, reconstruction of shower parameters, selection of gamma-ray events, and visualization of results and statistics. Each stage of `VEGAS` has multitudes of configuration options, providing flexibility necessary for a diversity of analyses.

### 2.4.1 Calibration Calculation

Stage 1 of `VEGAS` reads in VBF files and calculates hardware-dependent calibration parameters for both science and calibration data (and data simulations). Calibrations are determined for relative gains, timing offsets, and pedestal variances (pedvar) for each pixel. In addition, information from the VERITAS database is obtained for the status of individual pixels, tracking of the telescopes, telescope positions, and camera configuration necessary for later stages.

### 2.4.2 Calibration Application and Charge Integration

Stage 2 of `VEGAS` applies calibration information calculated in Stage 1, including relative gains, timing offsets, and pedestal variance to science data. The result is a hardware-independent charge information for FADC traces for each channel. The traces are integrated to calculate the total charge in each pixel, producing an image per event for each camera. A simple image cleaning algorithm is applied to eliminate pixels triggered by NSB fluctuations. Pixels with signal-to-noise ratio (defined as $\frac{IntegralCharge}{PedVar}$) exceeding 5 and any neighboring pixels exceeding signal-to-noise ratio of 2.5 are retained; all other pixels are discarded.

### 2.4.3 Image Parameterization

The cleaned image, which represents the projection of the Cherenkov light from the particle shower on the camera plane is parameterized using a standard approach defined by Hillas (1985) (this step is also performed in Stage 2). Figure 2.9 gives a representation of the Hillas parameters, which are intended to characterize the image of a gamma-ray shower on the camera plane with only a handful of quantities.

The Hillas parameterization describes the gamma-ray shower as a 2-dimensional ellipse with the following parameters: length $L$ and width $w$ of the ellipse, distance $d$

between the ellipse center of gravity and camera center, ellipse major axis azimuthal angle $\phi$, orientation angle $\alpha$, image size determined by the total charge of all pixels in the image, and the fraction of image size contained in the N brightest pixels, $fracN$, used to estimate image concentration. $\phi$ and $\alpha$ are primarily useful for single-telescope event reconstruction, but not for stereo reconstruction for an array like VERITAS. Hillas parametrization is a moment analysis and hence has a low computation cost.

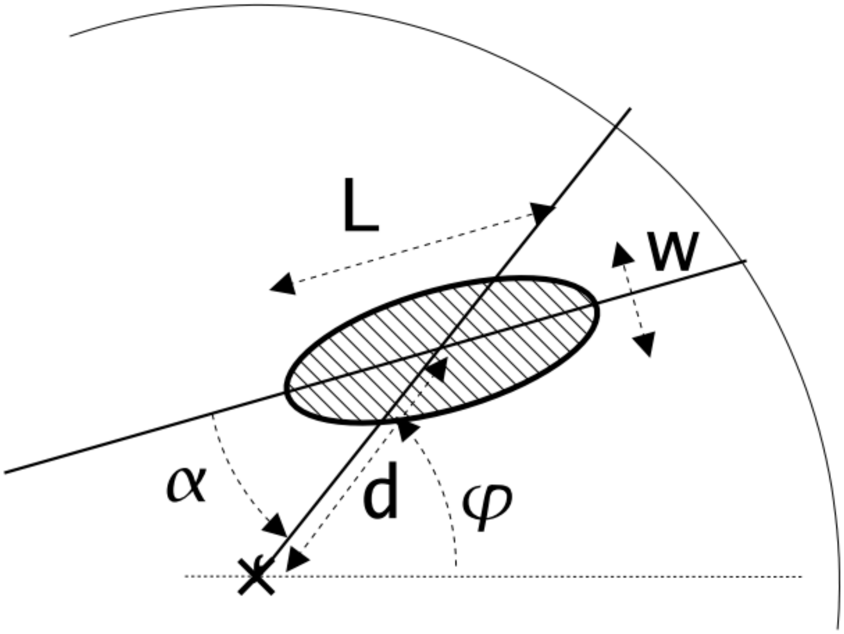

Figure 2.9: Representation of the Hillas parameters from de Naurois (2006).

### 2.4.4 Shower Parameterization

Shower direction, core location, height of the shower maximum, and gamma-ray energy of individual events are reconstructed at the array level in Stage 4 of `VEGAS` using the image parametrization information from previous stages and lookup tables from simulations.

Before these quantities are reconstructed, however, an image quality selection is applied for the image from each telescope. The criteria for the selection (with default values) during a standard analysis include a minimum number of pixels in an image, minimum image size, and maximum image distance. These criteria are intended to remove unreliable shower images, either because they are too small and could be spurious or are near or fall off the edge of the camera. Any images that fail to satisfy these criteria are not included in shower parameter reconstruction.

The shower core is defined as the location where the shower axis hits ground, i.e., the location on the ground a gamma ray would reach in the absence of the atmosphere. The shower core location is determined from the weighted (by image size) intersection of the image major axes from all participating telescopes, with the images projected onto the ground plane at the location of each telescope.

The shower direction or the arrival direction of the primary gamma ray is reconstructed by overlaying the images from all participating telescopes in the camera plane and calculating the weighted intersection of their major axes.

The shower maximum is the brightest part and the part with the largest number of particles during a development of an air shower. The height of the shower maximum can be calculated using the impact parameter of the shower - the distance between the shower core and a telescope - and the angle between the reconstructed shower direction and image centroid in the camera plane.

The energy of each event is reconstructed as part of the shower parameterization based on the size and the impact parameter. These parameters for each telescope event are used to look up the energy value from tables generated using simulations of gamma-ray showers for a wide range of observing parameters. The weighted average for the energy estimates for all participating telescopes is used as the reconstructed energy for the event.

### 2.4.5 Atmospheric Shower and Detector Simulations

As already hinted, the VERITAS data analysis relies heavily on simulations of the VERITAS detector and gamma-ray-initiated atmospheric showers. These simulations are necessary to generate instrument response functions (IRFs) used for the reconstruction of observed shower parameters, for separation of gamma-ray events from background, and for conversion of counts data to flux during spectral reconstruction.

Simulations of VERITAS data can be generated with one of three available packages, CARE[1] , GrISUDet[2] , KASCADE (Kertzman & Sembroski, 1994). These packages simulate the VERITAS detector and use simulations of atmospheric gamma-ray-initiated showers produced by a Monte Carlo code, CORSIKA (Heck et al., 1998) to generate simulated data.

For a typical simulation set, $\sim 10^7$ gamma-ray showers are generated and fed through the detector simulation. If a particular shower triggers the array, the event is recorded and stored in a VBF file. A recording of a simulated event carries similar information as an event from real observation, except it contains additional *true* properties, such as the energy and arrival direction of the initial gamma ray.

Simulation sets are produced for the full range of VERITAS observing conditions and array configurations. Simulation sets are generated for observations over three epochs, separated by substantial changes in VERITAS hardware: original array configuration (Epoch V4 or *old array*), after Telescope 1 move with original cameras (Epoch V5 or *new array*), after camera upgrade (Epoch V6 or *upgraded array*). In addition, separate simulations are produced for “winter” and “summer” observations (typically November through April and May through October, respectively, though exact dates vary each year) to account for seasonal differences in humidity and levels of dust and aerosols in the atmosphere, which modify the visibility of atmospheric showers. For a given array configuration and season, simulations cover the full observable range of source elevation and azimuth angles, offset angular distances from a source (for wobble observations), and night sky background light levels.

In order to obtain quantities necessary for comparing images of observed and simulated showers, such as shower length and width, impact parameter, size, etc., the simulated event data is processed with `VEGAS` following steps near-identical to real observations until the shower parameterization stage. Within the shower parameterization stage, multi-dimensional look-up tables are filled, with e.g., impact parameter and size of shower (along with observing conditions and configuration) corresponding to a specific gamma-ray energy. These look-up tables make up the first piece of the VERITAS IRFs. The second piece is the effective area.

---

[1] http://otte.gatech.edu/care

[2] http://www.physics.utah.edu/gammaray/GrISU/GrISU/Documentation/grisu.html

Once energy look-up tables are available, effective areas are produced by again processing simulation data through the shower parameterization step. This time, however, the energy reconstruction is carried out with the same method as energy reconstruction for data from observations described in Section 2.4.4. The comparisons between this reconstructed energy ($\mathrm{E_{reco}}$) and the known energy of the simulated gamma-ray ($\mathrm{E_{true}}$) for events after gamma-hadron separation define the effective area, given as,

$$A(E) = A_0 \left( \frac{\mathrm{N_{reco}}(E)}{\mathrm{N_{sim}}(E)} \right), \tag{2.1}$$

where $\mathrm{A_0}$ is the throw area of simulated events and $\mathrm{N_{reco}}(E)$ and $\mathrm{N_{sim}}(E)$ are the number of reconstructed simulated events after gamma-hadron separation and the total number of simulated events, respectively at energy $E$. A representative example of effective areas for a number VERITAS array configurations is show in Figure 2.7.

### 2.4.6 Event Selection or Gamma-Hadron Separation

The reconstructed events are a mix of gamma rays and cosmic rays. In order to separate out the gamma rays from the cosmic rays, a set of selection criteria based on shower parameters can be identified. The procedure relies on the so-called *mean reduced scaled parameters*, which quantify the similarity of observed shower properties to gamma-ray-initiated showers simulated for given observing conditions and array configurations. Mean reduced scaled parameters are defined as,

$$MSCP = \frac{1}{N_{\mathrm{tel}}} \sum_{i=1}^{N_{tel}} \frac{X_i - \tilde{X}_s}{\sigma_X}, \tag{2.2}$$

where $N_{tel}$ is the number of telescopes with parameterized images, $X_i$ is the observed parameter value for telescope $i$, $\tilde{X}_s$ is the corresponding parameter median value from gamma-ray simulations for similar zenith angle, impact parameter, and size, and $\sigma_X$ is the standard deviation of $X$. The typical Hillas parameters used for mean reduced scaled parameter calculations are the width and length parameters, primarily for their discriminatory power between cosmic-ray and gamma-ray events.

The default method for event separation in VERITAS analyses uses the so-called "box cuts," where cut values are determined for the mean reduced scaled width, mean reduced scaled length, and shower maximum height parameters to optimize sensitivity for different source strengths.

### 2.4.7 Background Estimation and Source Detection

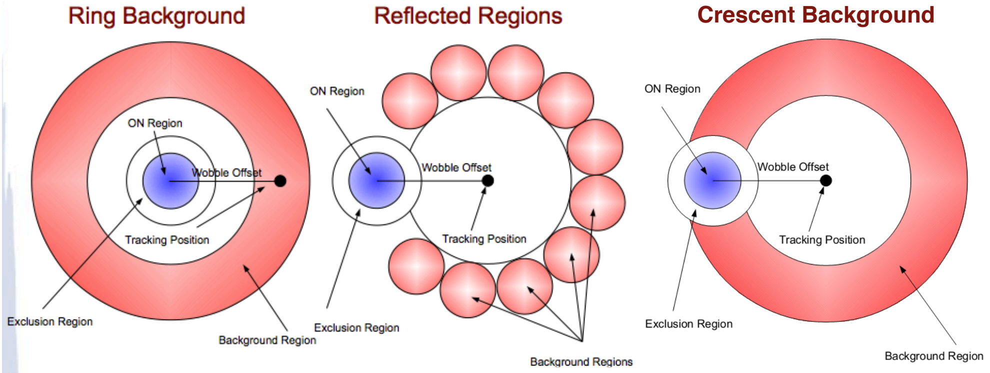

Figure 2.10: Background estimation methods in `VEGAS`. Image credit: *Dr. Ben Zitzer.*

The process of separation between cosmic-ray-like and gamma-ray-like events is not perfect and it is expected that the remaining gamma-ray-like events will still be contaminated by a background of cosmic-ray events.

Stage 6 projects events into sky coordinates and applies a cut based on the arrival direction with respect to the source position. This allows for further discrimination between gamma-ray and the background of cosmic-ray events. As opposed to the isotropically distributed cosmic rays with random arrival directions, gamma-rays are expected to arrive from the direction of the source.

`VEGAS` has several main methods for measuring the expected background from cosmic rays: reflected regions (wobble), ring background model, crescent background model, and timing for pulsar analysis.

The reflected regions method measures the number of counts for an On region centered around the source and identically sized Off regions intended to sample the background. Both the On and the Off regions are offset from the center of the camera by the same distance (typically by 0.5°) to guarantee equal acceptance. Since the acceptance varies both with energy and with the distance from the camera center, equal acceptances for the On and Off region are necessary for robust spectral reconstruction.

The ring background method, on the other hand, defines the Off region in an annulus around the On region. Sky maps for various quantities can be produced with this method by centering an On region with the Off region around it across the full grid of positions within the field of view.

The crescent background method combines the benefits of reflected regions and RBM methods, providing more background events than the reflected regions while maintaining suitability for spectral analysis. The background region used in this model is an annulus centered at the tracking position for each run rather than the source position. The circular On region located within this annulus is excluded from the background, making the background a crescent shape.

With a background defined, the significance, S of the excess events at the source location is calculated using the generalized version of the Li & Ma (1983) equation 17 by Klepser (2012),

$$S = \sqrt{2\left[N_{\mathrm{on}}\ln\left(\frac{1+\alpha}{\alpha}\frac{N_{\mathrm{on}}}{N_{\mathrm{on}}+N_{\mathrm{o}ff}}\right)+N_{\mathrm{o}ff}\ln\left((1+\alpha)\frac{N_{\mathrm{o}ff}}{N_{\mathrm{on}}+N_{\mathrm{o}ff}}\right)\right]}, \tag{2.3}$$

where $N_{on}$ and $N_{off}$ are the number of counts in the On and Off regions, respectively, and $\alpha$ is the On-Off normalization given as the ratio of the area of the On region to the area of the Off region.

A significance map is produced by applying the formula to the full grid of positions in a given field of view.

### 2.4.8 Spectral Reconstruction

To construct a spectrum from individual events, the main challenge is in properly applying instrument response functions and any associated uncertainties to convert the number of observed counts to flux.

By default, `VEGAS` uses a bin-by-bin correction method - a simplified version of a forward folding or parameterized deconvolution technique (Piron et al., 2001). The procedure boils down to solving the equation 2.4, where T is the exposure time, $\Delta$ E$_i$ is the size of an energy bin, $\alpha$ and $A_{reco_j}$ is the product of the effective area and the source spectral shape.

$$\frac{\mathrm{d}N_i}{\mathrm{d}E} = (T\Delta E_i)^{-1} \times \left( \sum_{j=0}^{N_{on}} (A_{reco_j})^{-1} - \alpha \sum_{k=0}^{N_{off}} (A_{reco_k})^{-1} \right) \tag{2.4}$$

Upper limits are calculated for non-significant bins (by default, less than $2\sigma$ significance and less than 5 excess counts). At the low-energy end, spectra are cut off at the threshold energy, determined from uncertainty in the effective areas, energy bias, and the peak of the energy distribution. The source spectral shape is assumed to be a power-law function ($\frac{\mathrm{d}N}{\mathrm{d}E} = N_0(\frac{E}{E_0})^{-\gamma}$) by default; however, `VEGAS` also allows exponential cutoff power-law, log-parabola, and user-specified custom functions.

The spectral reconstruction process is iterated until the input parameters for the source spectral shape converge to the parameters from the fit to the reconstructed spectrum.

### 2.4.9 Light Curve Production

The `VEGAS` program for producing light curves, known as `vaMoonShine` was designed to take the end-product of a standard `VEGAS` analysis and calculate flux and spectral properties in individual time bins. The arrival time of individual events is preserved throughout the analysis, allowing events to be assigned to time bins. Once the dataset is divided into time bins, spectral reconstruction is repeated in each time bin. The spectra are then integrated above a specified energy to determine flux. Provided there is enough signal in a given time bin, time-resolved spectral index and index vs. flux plots are generated as well; otherwise, upper limits are calculated using the Rolke method (Rolke & López, 2001). More advanced timing analyses, including variability measurements are not included in `VEGAS`. These are expected to be developed and applied by the analyst based on the specific needs of the analysis.

Over the last decade, VERITAS has operated very successfully, detecting 59 sources, including 31 discoveries or co-discoveries in the VHE gamma rays. These detections span a range of source classes from Galactic (e.g., supernova remnants, pulsar-wind nebulae, gamma-ray binaries) to extragalactic (AGN, starburst galaxies). This thesis is focused on VERITAS observations of blazars, the dominant source class.

# Chapter 3

# Extremely Stable and Extremely Distant Extreme Blazars

The following chapter presents an in-depth study of HESS J1943+213, one of the most stable gamma-ray blazars. The manuscript of this work, provided below has been submitted for publication to the Astrophysical Journal and is in the 2nd, likely final round of review. In addition to this manuscript, Section 3.5 details my contributions to a published work (Cerruti et al., 2017) exploring gamma-ray emission models of one of the most distant gamma-ray-detected blazars, PKS 1424+240.

**Abstract**

HESS J1943+213 is a very-high-energy (VHE; >100 GeV) $\gamma$-ray source in the direction of the Galactic Plane. Studies exploring the classification of the source are converging towards its identification as an extreme synchrotron BL Lac object. Here we present 38 hours of VERITAS observations of HESS J1943+213 taken over two years. The source is detected with ~20 standard deviations significance, showing a remarkably stable flux and spectrum in VHE $\gamma$-rays. Multi-frequency very-long-baseline array (VLBA) observations of the source confirm the extended, jet-like structure previously found in the 1.6 GHz band with European VLBI Network and detect this component in the 4.6 GHz and the 7.3 GHz bands. The radio spectral indices of the core and the jet and the level of polarization derived from the VLBA observations are in a range typical for blazars. Data from VERITAS, *Fermi*-LAT, *Swift*-XRT, FLWO 48$''$ telescope, and archival infrared and hard X-ray observations are used to construct and model the spectral energy distribution (SED) of the source with a synchrotron-self-Compton model. The well-measured $\gamma$-ray peak of the SED with VERITAS and *Fermi*-LAT provides constraining upper limits on the source redshift. Possible contribution of secondary $\gamma$-rays from ultra-high-energy cosmic ray-initiated electromagnetic cascades to the $\gamma$-ray emission is explored, finding that only a segment of the VHE spectrum can be accommodated with this process. A variability search is performed across X-ray and $\gamma$-ray bands. No statistically significant flux or spectral variability is detected.

## 3.1 Introduction

Blazars are active galactic nuclei (AGN) in which the axis of the relativistic jet is closely aligned with our line of sight (Urry & Padovani, 1995). The spectral energy distribution (SED) of blazars is characterized by a double-hump structure. In the simpler synchrotron self-Compton (SSC) models, the lower energy hump is attributed to synchrotron emission from relativistic leptons, whereas the higher-energy hump is thought to be from inverse-Compton upscattering of the synchrotron photons on the same population of relativistic leptons (Marscher, 1980a; Konigl, 1981; Reynolds, 1982). In more complicated scenarios, such as external-Compton models, an external photon field, typically from the accretion disk or the dusty torus around the central black hole is required to explain the higher energy hump (e.g., Sikora et al., 1994). Alternatively, part or all of the $\gamma$-ray emission may be attributed to a hadronic origin, with proton synchrotron radiation and pion production constituting the two primary mechanisms (Mücke & Protheroe, 2001; Mücke et al., 2003). Variability is a common attribute of blazars, with variations in flux and spectrum detected in every observed frequency band and over a wide range of timescales (see Böttcher, 2007).

Blazars come in two flavors: BL Lacertae objects (BL Lacs) and Flat Spectrum Radio Quasars (FSRQs), with BL Lacs exhibiting lower power jets and higher Doppler factors and FSRQs possessing high-powered jets and showing high Compton dominance (Stickel et al., 1991, 1993). Based on the location of the synchrotron peak, BL Lacs are classified into low, intermediate, and high synchrotron peak BL Lacs (LBLs, IBLs, and HBLs respectively) (Padovani & Giommi, 1995). HBLs are the most commonly detected blazars in VHE $\gamma$-rays, comprising 47 of the 64 VHE-detected blazars[1] . A subclass of HBLs has been proposed, known as extreme HBLs (EHBLs), identified by synchrotron emission peaks at energies above 1 keV (Costamante et al., 2001).

Within the context of the blazar sequence (e.g., Fossati et al., 1998; Ghisellini & Tavecchio, 2008; Meyer et al., 2011; Giommi et al., 2012) – where the blazar jet luminosity is inversely related to the Doppler factor – EHBLs would be the least luminous and would have the highest Doppler boosting factors, making them one of the most efficient and extreme accelerators in the Universe. However, with only a handful of blazars belonging to the EHBL subclass (including 1ES 0229+200, 1ES 0347-121, RGB J0710+591, 1ES 1101-232), there is as yet no conclusive physical explanation for them.

EHBLs constitute a challenge for leptonic emission models that tend to only accommodate the observed spectral energy distributions of these objects with unusually hard particle populations (e.g., Tavecchio et al., 2010). Moreover, unlike other blazars, they do not appear to exhibit rapid variability, despite predictions of large flux variations on short timescales by leptonic models. The higher synchrotron peak frequency could potentially explain this as an observational effect by shifting the more variable emission produced by higher energy particles into the hard X-ray band. The less energetic particles producing steadier emission would then be responsible for the emission in the commonly observed infrared to soft X-ray bands.

---

[1] tevcat2.uchicago.edu

The lack of rapid flux variability and the hard VHE spectra make EHBLs attractive candidates for hadronic emission models. Their observed properties can be explained by synchrotron emission from relativistic protons within the jet and by proton-initiated electromagnetic cascades (Cerruti et al., 2015). As such, the more distant EHBLs are also ideal candidates for a proposed $\gamma$-ray emission mechanism in which at least a component of the observed VHE emission originates from ultra-high-energy cosmic rays (UHECRs) that propagate an appreciable fraction of the distance between the blazar and Earth before producing electromagnetic cascades along the line of sight (see Ferrigno et al., 2004; Bonnoli et al., 2015; Essey & Kusenko, 2010). If either mechanism is confirmed, EHBLs would become one of the most likely sources for the acceleration sites of UHECRs, directly addressing one of the oldest questions in high-energy astrophysics.

### 3.1.1 HESS J1943+213: An Extreme HBL

HESS J1943+213 is a VHE $\gamma$-ray point source discovered during the H.E.S.S. Galactic Plane scan (Abramowski et al., 2011). Since the discovery publication, the identity of HESS J1943+213 has been a topic of debate, with most of the observations suggesting the source is a blazar, but with alternative possibilities including a pulsar wind nebula (PWN) and a $\gamma$-ray binary.

Assuming the source is a $\gamma$-ray binary, Abramowski et al. (2011) used the lack of detection of a massive (O- or Be-type) companion star to estimate a distance limit of greater than $\sim$25 kpc. This distance places the binary well beyond the extent of the Galactic disk and implies an X-ray luminosity 100–1000 times higher than luminosities of known $\gamma$-ray binaries. Hence, Abramowski et al. (2011) disfavor the $\gamma$-ray binary scenario.

The point-like appearance in X-rays and the soft VHE spectrum, with a power-law index of $\Gamma = 3.1 \pm 0.3$, motivated Abramowski et al. (2011) to argue against the PWN scenario. However, 1.6-GHz observations of the HESS J1943+213 counterpart with the European VLBI Network (EVN) detected an extended source, with FWHM angular size of 15.7 mas (with 3.5 mas expected size for a point source) (Gabányi et al., 2013). Based on this measurement, the brightness temperature of the counterpart was estimated to be $7.7\times10^7$ K and was used to argue against the blazar scenario, as the expected brightness temperature of VHE-detected HBLs is in the $10^9$–$10^{10}$ K range. In addition, Gabányi et al. (2013) employed a $1'$ feature observed in the 1.4-GHz very-large array (VLA) C-array configuration image to support the PWN hypothesis, with the assertion that the angular size of the feature is consistent with a Crab-like PWN placed at a distance of 17 kpc. However, a pulsar search with the Arecibo telescope resulted in a non-detection and a claim of no pulsar at the HESS J1943+213 location at ∼70% confidence (Straal et al., 2016).

As reported by Abramowski et al. (2011), all observations were found to be consistent with the blazar scenario, however, including the point-like nature in both X-rays and VHE, the soft VHE spectral index, and an (unpublished) featureless IR spectrum. In addition, Tanaka et al. (2014) argued in favor of an EHBL by constructing a spectral energy distribution and by drawing comparisons to a known EHBL, 1ES 0347-121. The case for the extreme blazar has been bolstered further with Peter et al. (2014) observing the near-infrared (K-band) counterpart of HESS J1943+213 and claiming a detection of an elliptical host galaxy.

Recently, Straal et al. (2016) obtained VLBI observations in the 1.5 GHz and 5 GHz bands using the e-Multiple Element Remotely Linked Interferometer Network (e-MERLIN), showing that the source exhibits a flat spectrum between the two bands and claiming a detection of flux density variability in the 1.5 GHz band when compared with the EVN observations of the source.

A strong argument for the blazar case was made with a reanalysis of the initial EVN dataset and addition of new and higher resolution observations in 2014 (Akiyama et al., 2016). Based on both EVN observations, the brightness temperature of the core is estimated to be well within the blazar range with $T_B > 1.8\times10^9$ K and $7.7\times10^9$ K for 2011 and 2014 observations respectively. The claim for flux density variability was also made more robust through a consistent analysis of EVN data from the two epochs. In addition, the 2014 EVN observations revealed extended jet-like structure with brightness temperatures of the individual substructures of the extended emission typical of AGN jets.

The arguments presented above strongly suggest that HESS J1943+213 is a BL Lac object behind the Galactic Plane. With a synchrotron peak located at ∼10 keV and with no apparent cutoff, HESS J1943+213 is classified as an extreme synchrotron BL

Lac object or an EHBL. In addition to the location of the synchrotron peak, HESS J1943+213 displays other attributes of EHBLs, including a very large X-ray to radio flux ratio, weak emission in the GeV band and a lack of strong flux variability relative to other blazars.

There are only indirect limits on the distance of HESS J1943+213 measured by Peter et al. (2014). Lower limits on the redshift come from the assumed size for the host galaxy and measurement of its extension in near IR, while upper limits are derived by extrapolating the *Fermi*-LAT spectrum into the VHE regime and assuming that the deviations from the extrapolated spectrum are entirely due to absorption by the extragalactic background light (EBL). The redshift bounds found by Peter et al. (2014) are $0.03 < z < 0.45$.

In what follows, we detail results from observations of HESS J1943+213 with VERITAS, *Fermi*-LAT, *Swift*-XRT, and VLBA and further characterize the properties of the source as an EHBL. Section 3.2 presents new observations and results collected with VERITAS and VLBA, in addition to analyses of 8-years of *Fermi*-LAT data, recent *Swift*-XRT observations, and long-term optical observations with the Fred Lawrence Whipple Observatory (FLWO) 48″ telescope. The results from the analysis of HESS J1943+213 multi-wavelength data are interpreted and discussed in Section 3.3, including a derivation of improved and more robust limits on the source redshift (3.3.1) based on the $\gamma$-ray spectra from *Fermi*-LAT and VERITAS. We perform a search for variability in X-ray and $\gamma$-ray observations of HESS J1943+213 (3.3.2), construct and model the broadband spectral energy distribution of the source (3.3.3), and explore UHECR line-of-sight $\gamma$-ray production as an alternative emission mechanism (3.3.4). We conclude in Section 3.4.

## 3.2 Multi-wavelength Observations of HESS J1943+213 and Data Analysis

### 3.2.1 Strong Detection and Characterization of the Source with VERITAS

The Very Energetic Radiation Telescope Array System (VERITAS) is an imaging atmospheric Cherenkov telescope array located at the Fred Lawrence Whipple Observatory in southern Arizona ($31^\circ\ 40'$ N, $110^\circ\ 57'$ W, 1.3 km a.s.l.). VERITAS is composed of four 12-m telescopes, each equipped with a 499 photo-multiplier tube camera providing a $3.5^\circ$ field of view (Holder et al., 2006). The array can reliably reconstruct $\gamma$-rays with energies between 85 GeV and 30 TeV, and has an angular resolution at 68% containment of $< 0.1$ degrees for a 1 TeV photon. The energy resolution is 17% at 1 TeV, with a $10^5$ m$^2$ peak effective area (Park & the VERITAS Collaboration, 2015).

VERITAS observations of HESS J1943+213 took place over ∼2.5 years and are broken up into two periods for spectral analysis: (I) 2014 May 27 (MJD 56804) – 2014 July 02 (MJD 56840), (II) 2015 April 20 (MJD 57132) – 2015 November 09 (MJD 57335). The total exposure time of these observations is 37.2 hours, amounting to a weather-cleaned live time of 30.9 hours. Observations from Period I focused on deep exposures of the source and constitute 24.2 hours of weather-cleaned data, while the remaining 6.7 hours in Period II aimed at probing the source for variability. The source elevation during the VERITAS observations was within the $63^\circ - 80^\circ$ range, with the common low-energy threshold for this analysis determined to be 180 GeV.

The analysis of the VERITAS data is performed and cross-evaluated for consistency with the two independent, standard VERITAS analysis packages (Cogan, 2008; Daniel, 2008). The images of Cherenkov light from particle showers are parameterized with the classical Hillas approach (Hillas, 1985). Standard cuts optimized for average source strength (∼5% Crab Nebula flux) and spectral index ($\Gamma \sim 2.7$) are used for separating $\gamma$-ray and cosmic ray events (See Acciari et al., 2008, for details). The background for $\gamma$-ray-like events is measured using the reflected regions method (Fomin et al., 1994). The source significance is calculated using the generalized version of equation 17 from Li & Ma (1983) derived by Klepser (2012).

A source centered at $\alpha = 19^h 43^m 59^s \pm 1^s{}_{(\mathrm{stat})} \pm 2^s{}_{(\mathrm{sys})}$ and $\delta = 21^\circ 19' 05'' \pm 11''_{(\mathrm{stat})}$

Table 3.1. Summary of VERITAS observations.

| Period | Exposure [hours] | $\sigma$ | Flux (>180 GeV) [$10^{-12}$ cm$^{-2}$ s$^{-1}$] | $\Gamma$ | $\chi^2$/NDF |
|---|---|---|---|---|---|
| I | 24.2 | 17.9 | 8.61±0.78 | 2.76±0.12 | 3.5/6 |
| II | 6.7 | 7.2 | 8.55±1.88 | 3.12±0.38 | 4.4/4 |
| Combined | 30.9 | 19.3 | 8.61±0.67 | 2.81±0.12 | 3.8/5 |

$\pm\ 25''_{\rm (sys)}$ is detected with an excess of 19.3 standard deviations ($\sigma$), consistent with the catalog position of HESS J1943+213. The VERITAS detection is fit by a 2-dimensional Gaussian function representing the VERITAS point spread function. The fit $\chi^2$/NDF is 2069/1931, which corresponds to a fit probability of 1.5%. The best-fit Gaussian width is 0.05 degrees, smaller than the angular resolution of VERITAS. Thus, there is no evidence for source extension. The VERITAS source name is VER J1943+213.

The VERITAS differential energy spectra of HESS J1943+213 are constructed separately for each period specified above to look for variations in the source spectrum. The spectra from the two periods agree with each other within the statistical uncertainties, indicating no significant detection of spectral variability and justifying the use of a combined, time-averaged spectrum from the entire dataset for the SED modeling detailed in Section 3.3.3. The combined VERITAS spectrum of HESS J1943+213 is presented in Figure 3.1. The spectrum is fit well by a power-law function, $\frac{dN}{dE} = \mathrm{N}_0(\frac{E}{E_0})^{-\Gamma}$, with a spectral index, $\Gamma = 2.81 \pm 0.12_{\rm (stat)}{}^{+0.14}_{-0.34}{}_{\rm (sys)}$ in the 180 GeV–2 TeV energy range. Abramowski et al. (2011) reported a spectral index of $3.1 \pm 0.3_{\rm (stat)} \pm 0.2_{\rm (sys)}$ for HESS J1943+213 above 470 GeV. In the same energy range, the VERITAS best-fit spectral index is $2.85 \pm 0.32_{\rm (stat)}{}^{+0.14}_{-0.34}{}_{\rm (sys)}$, consistent with the H.E.S.S. result.

There is no evidence for flux variability between Periods I and II and on weekly timescales as illustrated by the VERITAS light curve of HESS J1943+213 in Figure 3.2. The average flux of the source is $(5.57 \pm 0.46_{\rm (stat)}{}^{+0.72}_{-1.27}{}_{\rm (sys)}) \times 10^{-12}$ cm$^{-2}$ s$^{-1}$ above 230 GeV. A constant line is fit to the full weekly-binned light curve with $\chi^2$/NDF = 15.6/12, corresponding to a p-value of 0.21 for a constant flux. The higher cadence Period I observations were investigated for variability separately on both daily and weekly timescales. No significant variability was found in that dataset, with $\chi^2$/NDF = 31.34/20 for a constant fit to a daily light curve, corresponding to a p-value of 0.05 for a constant

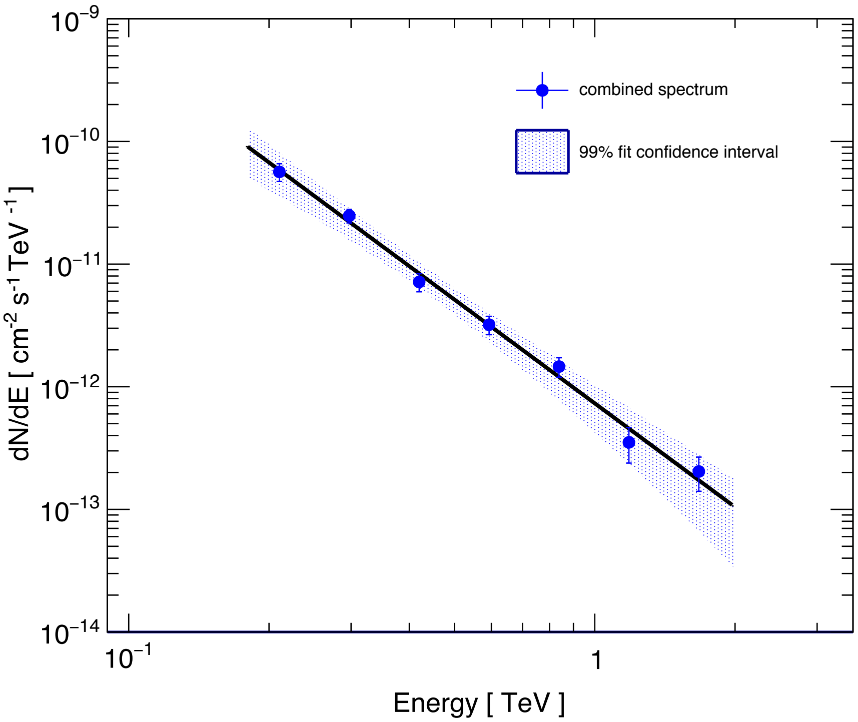

Figure 3.1: Time-averaged VERITAS spectrum of HESS J1943+213, combining data from 2014 and 2015 observations. The band shows the 99% confidence interval of a power-law fit to the spectrum.

flux (Shahinyan & the VERITAS Collaboration, 2015).

H.E.S.S. reported a source flux of $(1.3 \pm 0.2_{(\mathrm{stat})} \pm 0.3_{(\mathrm{sys})}) \times 10^{-12}$ cm$^{-2}$ s$^{-1}$ above 470 GeV (Abramowski et al., 2011) from observations taken between 2005 and 2008. This is consistent with the VERITAS flux above 470 GeV of $(1.47 \pm 0.16_{(\mathrm{stat})}{}^{+0.72}_{-1.27(\mathrm{sys})}) \times 10^{-12}$ cm$^{-2}$ s$^{-1}$. Thus, in addition to the remarkable stability of the source flux over two years of VERITAS observations, there is also good agreement between fluxes from observations more than six years apart from two different VHE $\gamma$-ray instruments.

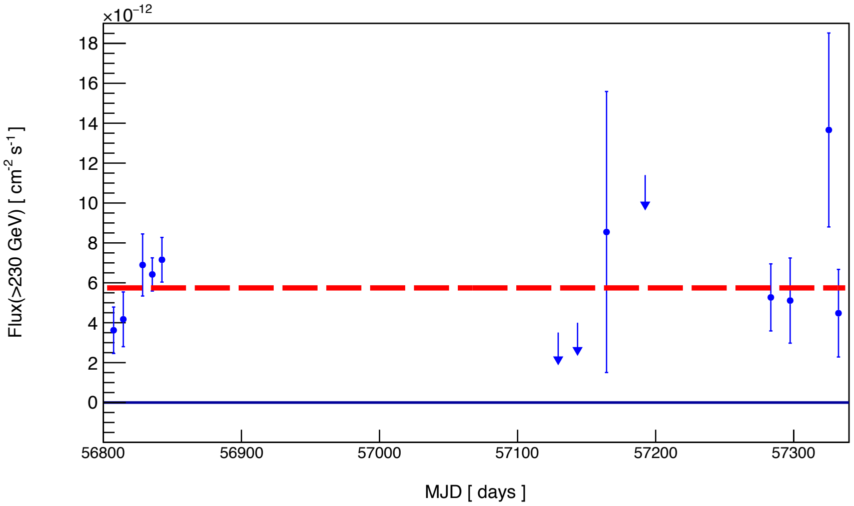

Figure 3.2: VERITAS light curve of HESS J1943+213 above 230 GeV. The red dashed line is a fit of a constant to the data. 68% upper limits are derived for time bins in which the source flux is consistent with zero.

### 3.2.2 Improved Detection and Spectral Analysis with an 8-year *Fermi*-LAT Dataset

The Large Area Telescope (LAT) on board the *Fermi* Gamma-ray Space Telescope (*Fermi*-LAT) is a pair-conversion $\gamma$-ray instrument sensitive to high energy (HE) $\gamma$-rays with energies between 20 MeV and 300 GeV. The LAT has a field of view that covers ~20% of the sky at any given time in survey mode, providing 30 minutes of live time on each point in the sky every two orbits (~3 hours).

A source associated with HESS J1943+213 is included in the Second Catalog of Hard *Fermi*-LAT Sources (2FHL) (Ackermann et al., 2016a) within the 50 GeV – 2 TeV energy range, with a TS = 39.6 and a power-law spectral index of 2.73 ± 0.66. In addition, the source is included in the preliminary Third Catalog of Hard *Fermi*-LAT Sources (3FHL) (The Fermi-LAT Collaboration, 2017) in the 10 GeV – 2 TeV range, with a TS = 127.7 and a spectral index of 1.45 ± 0.29. HESS J1943+213 has been previously detected at 5.1 $\sigma$ significance through an analysis of 5 years of *Fermi*-LAT data in the 1–100 GeV energy range, producing a spectrum well fit by a power-law with normalization of $(3.0 \pm 0.8_{\mathrm{(stat)}} \pm 0.6_{\mathrm{(sys)}}) \times 10^{-15}$ cm$^2$ s$^{-1}$ MeV$^{-1}$ at 15.1 GeV and spectral index, $\Gamma = 1.59 \pm 0.19_{\rm (stat)} \pm 0.13_{\rm (sys)}$ (Peter et al., 2014).

In this work, the Fermi Science Tools[2] version *v10r0p5* and the P8R2_SOURCE_V6 instrument response functions are used for analyzing *Fermi*-LAT observations, with the assistance of Fermipy (Wood et al., 2017) - a python package with a high-level interface for Fermi-LAT analysis. Eight years of PASS8 *Fermi*-LAT data are selected for the analysis between 2008 August 04 and 2016 August 04. The region of interest (RoI) is defined within a 10° radius of the catalog position of HESS J1943+213 ($\alpha$: $19^h43^m55^s$, $\delta$: $21^\circ18'8''$). SOURCE class events with energies in the 3 – 300 GeV range are selected. The 3 GeV lower bound on the energy is chosen to decrease the contribution from the Galactic diffuse background. In addition, only events with zenith angles $< 100^\circ$ and rocking angles $< 52^\circ$ are included to avoid contamination from the Earth limb.

A model for the RoI is constructed by including all *Fermi*-LAT Third Source Catalog (3FGL) (Acero et al., 2015) sources within 15° radius of the source position and models for emission from the Galactic diffuse (gll_iem_v06.fits) and the isotropic (iso_P8R2_SOURCE_V6_v06.txt) backgrounds. In addition, a point source with a power-law spectrum is added at the catalog position of HESS J1943+213. A binned likelihood analysis is performed to find the optimal model for the RoI and extract the best-fit source parameters. The parameters of weak sources with test statistic (TS) $< 16$ and all sources located more than 7° away from the center of the RoI are frozen during this procedure.

A source at the position of HESS J1943+213 is detected with a TS value of 147.5 corresponding to a significance of $\sim$12 $\sigma$. The source is modeled as a power-law function with an index of $1.67 \pm 0.11_{\rm (stat)}$ and a flux of $(2.71 \pm 0.43_{\rm (stat)}) \times 10^{-10}$ cm$^{-2}$ s$^{-1}$ above 3 GeV. Spectral points are generated by repeating the *Fermi*-LAT analysis with events selected within the energy range of each spectral bin. In addition, different spectral shapes are explored for the HESS J1943+213 detection showing no statistically significant preference for a curved model over a power law.

### 3.2.3 *Swift*-XRT Observations Contemporanous with VERITAS

X-ray observations of HESS J1943+213 were obtained with the *Swift*-XRT instrument on 2014 June 17, 2014 June 19, and 2014 June 21, contemporaneous with VERITAS

---

[2] https://fermi.gsfc.nasa.gov/ssc/data/analysis

Table 3.2. Summary of *Swift*–XRT observations.

| Date | Observation ID | Exposure [seconds] | Log10 [Flux] (2–10 keV) Log10 [erg cm$^{-2}$ s$^{-1}$] | Index | $\chi^2$/NDF |
|---|---|---|---|---|---|
| 2014 June 17 | 00033319001 | 967 | -10.75±0.05 | 2.16±0.18 | 4.23/9 |
| 2014 June 19 | 00033319002 | 769 | -10.66±0.05 | 1.92±0.16 | 3.29/8 |
| 2014 June 21 | 00033319003 | 1156 | -10.53±0.04 | 1.77±0.13 | 12.15/17 |

observations. The XRT data analyzed here were collected in the *photon counting* mode, amounting to a total of 48.2 minutes of exposure time.

The XRT data analysis is performed with the standard XRTDAS v3.0.0 tools included in the HEASoft package Version 6.15.1, while Xspec (Arnaud, 1996) v12.8.1g is used for the spectral analysis.

XRT spectra are constructed by unfolding the counts spectra with instrument response functions included in CALDB 1.0.2 and by assuming an absorbed power-law functional form for the intrinsic spectrum: $\frac{dN}{dE} = \mathrm{N}_0(\frac{E}{E_0})^{-\Gamma} e^{-\mathrm{N_H}\sigma(E)}$, where $\sigma$(E) is the photo-electric cross-section and $\mathrm{N_H}$ is the HI column density. Spectra were first fit using absorbed power-law functions with the $\mathrm{N_H}$ parameter left free to search for excess over the Galactic $\mathrm{N_H}$ value obtained from the Leiden/Argentine/Bonn (LAB) survey, $\mathrm{N_H}$ = 0.82×10$^{22}$ cm$^{-2}$ (Kalberla et al., 2005). The fitted value of $\mathrm{N_H}$ is consistent with the value from the LAB survey for the observation on 2014 June 17 ($\mathrm{N_H}$ = (0.87±0.48)×10$^{22}$ cm$^{-2}$) and slightly exceeds the LAB survey value for observations on 2014 June 19 ($\mathrm{N_H}$ = (1.48±0.54)×10$^{22}$ cm$^{-2}$) and 2014 June 21 ($\mathrm{N_H}$ = (1.21±0.35)×10$^{22}$ cm$^{-2}$). The high-precision *Suzaku*-XIS and HXD/PIN spectrum from Tanaka et al. (2014) measured $\mathrm{N_H}$ = (1.38 ± 0.03)×10$^{22}$ cm$^{-2}$, also in excess of the LAB survey value.

The spectrum from each observation is shown in Figure 3.3. Spectra are again constructed assuming absorbed power-law functional forms; however, the $\mathrm{N_H}$ parameter is kept fixed to the value from Tanaka et al. (2014). The results from the spectral fits are included in Table 3.2. The uncertainties represent the 68% confidence intervals for the respective quantities. No significant spectral variability is detected between observations. Moreover, the results are comparable to measurements from 2006 October 10 observations of HESS J1943+213 with *Swift*-XRT, which reported a spectral index of 2.04 ± 0.12 and a flux of (1.83 ± 0.04) × 10$^{-11}$ erg cm$^{-2}$ s$^{-1}$ (Malizia et al., 2007;

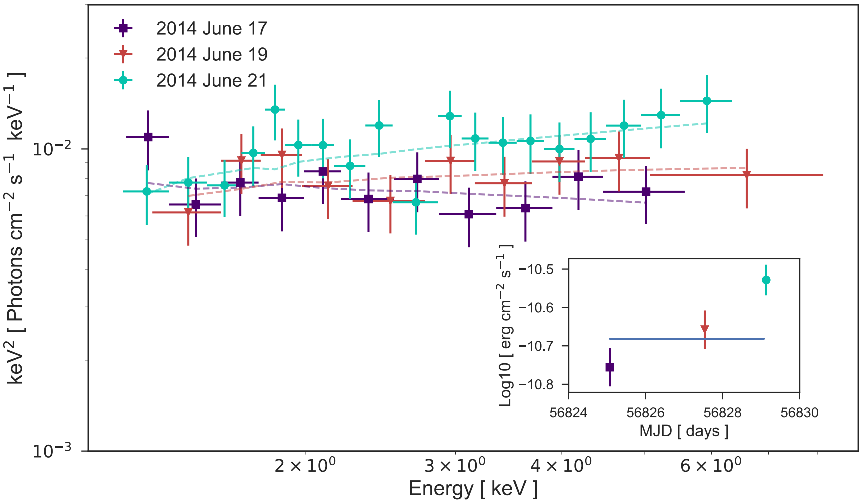

Figure 3.3: Spectra of HESS J1943+213 with *Swift*-XRT for the three observations taken in 2014. The dashed lines show the absorbed power-law models used for unfolding the spectra. The inset figure shows the 2–10 keV fluxes for the three observations.

Landi et al., 2009).

### 3.2.4 Long-Term Optical Observations with FLWO 48″

The FLWO 48″ (1.2 m) telescope is located on Mt. Hopkins in southern Arizona. As part of a long-term, multi-blazar observing program, optical photometry of HESS J1943+213 was obtained between 2013 September 27 and 2017 March 14 in SDSS r′ filter and between 2015 March 25 and 2017 March 14 in Harris V and SDSS i′ filters. The data reduction was performed using standard IDL tools. The magnitude zero-point was determined for each image by comparison to cataloged stars in order to derive the magnitude for HESS J1943+213 and a reference star located in the same field of view and only a few arcseconds from the source. The observations were not corrected for Galactic extinction, since extinction estimates at low Galactic latitudes are highly unreliable. Deviations of the reference star magnitude from the mean are used to reject observations from nights with poor weather. Magnitudes are converted to spectral flux densities assuming an AB magnitude system. The resulting light curves in the FLWO 48″ Harris V and SDSS r′ and i′ filters for HESS J1943+213 are presented in Figure 3.4. For brighter, non-variable objects, such as the reference star used in this analysis, the distribution of measured magnitudes is consistent with the calculated statistical errors. We find, however, that for fainter objects with magnitude similar to HESS J1943+213, there is scatter in the measurements exceeding the calculated errors, indicating a dominant source of systematic error that remains to be identified. Hence, the FLWO 48″ data are not used for a variability search. Average fluxes are derived for each band and included in the source SED in Section 3.3.3.

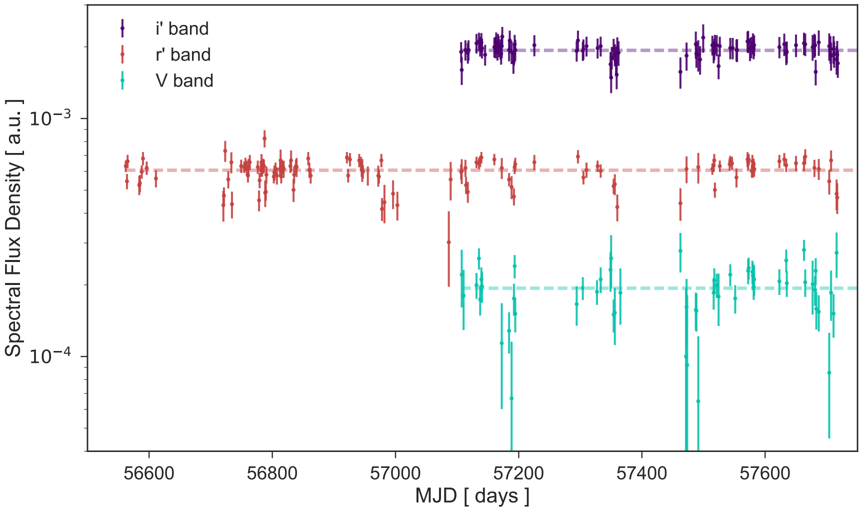

Figure 3.4: Light curves from FLWO 48″ observations with Harris V (teal), SDSS r′ (red) and SDSS i′ (purple) filters. The dashed lines show the average flux for each of the light curves.

### 3.2.5 Multi-frequency VLBA Observations in 2015 and 2016

The radio counterpart of HESS J1943+213 was observed by the authors using the VLBA. Observations took place over two epochs on 2015 August 11 (Project ID: BS246) and on 2016 August 08 (Project ID: BS253).

The 2015 observations (epoch I) were part of a request to follow up on the initial EVN detection and characterization of the source (Gabányi et al., 2013) by using four VLBA frequency bands (1.6 GHz, 4.3 GHz, 7.6 GHz, and 15 GHz). The epoch II observations taken in 2016 aimed to obtain deeper exposures of the source in C band (split into 4.3 GHz and 7.6 GHz bands) in order to characterize extended structures and measure polarization. The observations were targeted at the position reported from the EVN detection: $\alpha = 19^h43^m56^s2372$, $\delta = 21°18'23''402$. All 10 VLBA antennae participated in both sets of observations. The total length of the 2015 observations was 4 hours, which included exposures on a phase calibrator source, J1946+2300, and a bandpass calibrator source, 3C 345. The 2016 observations totaled 8 hours and included exposures on the same phase calibrator and bandpass calibrator sources, as well as an astrometric check source, J1935+2031, and a polarized calibrator, 3C380.

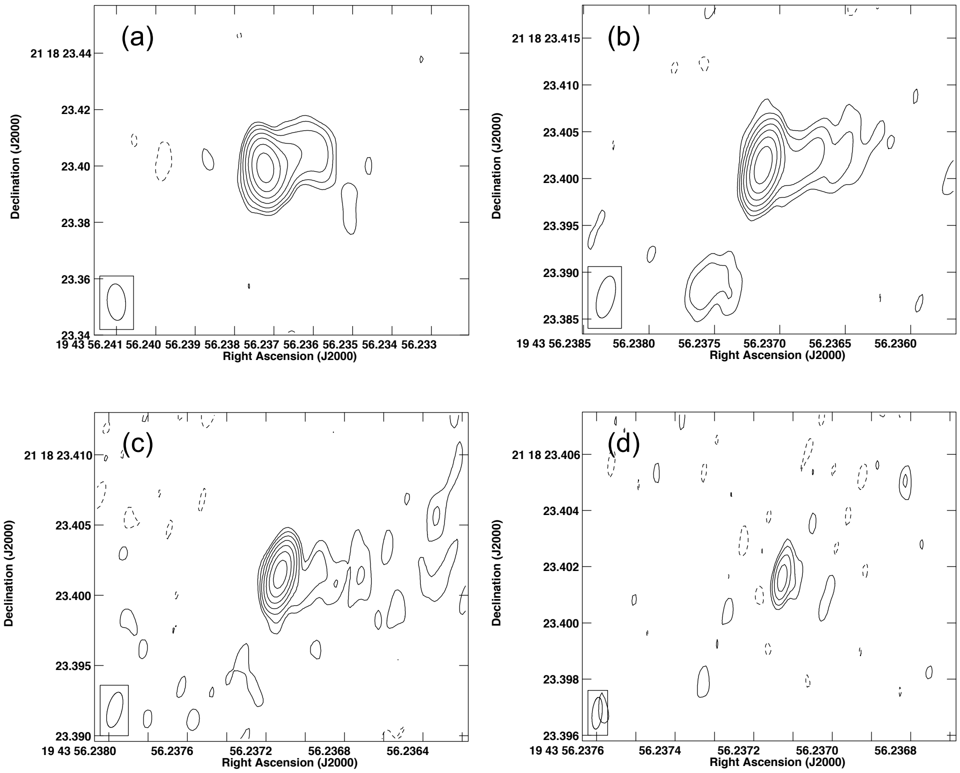

Figure 3.5: Contour images of HESS J1943+213 with VLBA (a) 1.6 GHz, (b) 4.3 GHz, (c) 7.6 GHz, and (d) 15 GHz bands. Contour levels plotted above 1% of the peak image intensity: −1, 1, 2, 4, 8, 16, 32, 64 (1.6 GHz); −2, −1, 1, 2, 4, 8, 16, 32, 64 (4.3 GHz and 7.6 GHz); −8, 8, 16, 32, 64 (15 GHz). Negative levels are shown with dashed lines.

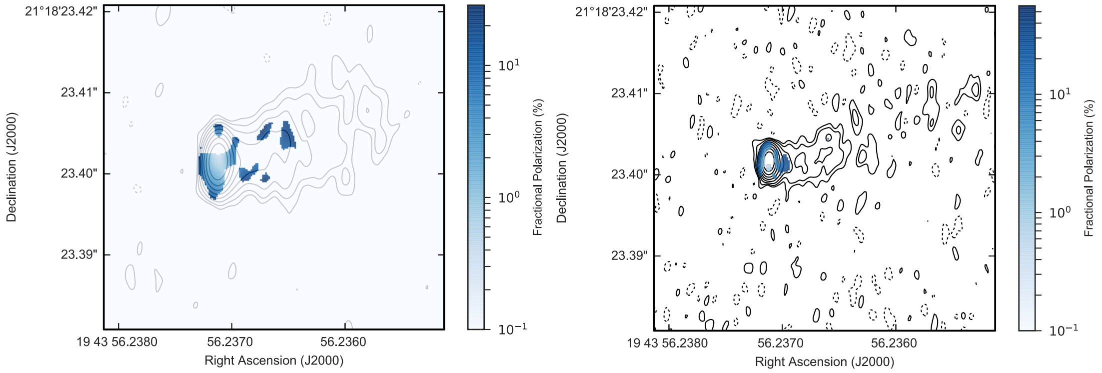

Figure 3.6: Epoch II VLBA 4.3 GHz (left) and 7.6 GHz (right) images of HESS J1943+213 radio counterpart. The contours represent the -1 (dashed), 1, 2, 4, 8, 16, 32, 64, 128 levels above 0.3% of the peak image intensity. The fractional polarization is illustrated with the color maps.

The NRAO Astronomical Image Processing System[3] (AIPS) (van Moorsel et al., 1996) is used to reduce and calibrate the VLBA data for HESS J1943+213. Images from the 2015 observations were produced for each band and are displayed in Figure 3.5. There is clear evidence for extended, jet-like emission in the 1.6 GHz, 4.3 GHz, and 7.6 GHz images. This is the first detection of the extended milliarcsecond-scale structure from the HESS J1943+213 counterpart in 4.3 GHz and 7.6 GHz bands, allowing multi-frequency exploration of its properties in VLBI. A similar core-jet structure has been previously detected with deep 1.6 GHz band observations with EVN (Akiyama et al., 2016). Images from the 2016 VLBA observations in 4.3 GHz and 7.6 GHz bands shown in Figure 3.6 reveal the source structure in more detail and provide fractional polarization measurements. The 1–3 % polarization of the core in both bands detected for the source is consistent with polarization levels seen in other $\gamma$-ray blazars (Linford et al., 2012). Quantitative results from the analysis of the two epochs of VLBA observations are provided in Table 3.3.

The core brightness temperature ($T_B$) of the HESS J1943+213 counterpart is estimated using images from all bands except for the 15 GHz band from 2015 observations, where the sensitivity was too low for phase and amplitude self-calibration. Lower limits to $T_B$ are derived due to a partially resolved core and the possibility of interstellar scattering, resulting in $T_B > 1.2\times10^9$ K in the most conservative case, measured with the

---

[3] http://www.aips.nrao.edu

Table 3.3. Measurements of HESS J1943+213 properties from phase and amplitude self-calibrated VLBA images.

| Band | Peak Intensity [mJy/beam] | Image Noise [mJy/beam] | Spectral Flux Density [mJy] | $T_B$ [K] |
|---|---|---|---|---|
| **2015** | | | | |
| 1.6 GHz | 18.564 | 0.073 | $23.31 \pm 0.15$ | $> 1.2 \times 10^9$ |
| 4.3 GHz | 15.252 | 0.065 | $16.25 \pm 0.12$ | $> 2.2 \times 10^9$ |
| 7.6 GHz | 15.032 | 0.071 | $16.23 \pm 0.13$ | $> 1.7 \times 10^9$ |
| $^a$15 GHz | 8.1059 | 0.16 | $10.51 \pm 0.32$ | N/A |
| **2016** | | | | |
| 4.3 GHz | 18.388 | 0.020 | $17.12 \pm 0.047$ | $> 2.2 \times 10^9$ |
| 7.6 GHz | 14.877 | 0.025 | $20.39 \pm 0.041$ | $> 1.5 \times 10^9$ |

$^a$Values are from phase-only self-calibrated images.

1.6 GHz image from the 2015 dataset. The brightness temperature values are well within the range for blazars. We do not confirm the significantly lower brightness temperature measurement of $T_B = 7.7\times10^7$ K, which was based on the EVN 1.6 GHz image (Gabányi et al., 2013) and which has subsequently been reanalyzed showing higher brightness temperature, $T_B > 1.8\times10^9$ K (Akiyama et al., 2016).

Using the 2015 observations and assuming a power law function of the form $S \propto \nu^{-\alpha}$, where S is the spectral flux density, a spectral index $\alpha_{\mathrm{core}} = 0.3 \pm 0.06$ is measured for the HESS J1943+213 core, determined from all 4 bands, and an index $\alpha_{\mathrm{jet}} = 1.1 \pm 0.4$ for the extended emission is calculated over 9.3 square milliarcseconds based on the 4.3 GHz and 7.6 GHz images. With the deeper 2016 dataset, we construct a spectral index map and present it in Figure 3.7. In order to construct the map, the 7.6 GHz image is convolved with a larger beam size to match the resolution of the 4.3 GHz image. There is a visible discrepancy between $\alpha_{\mathrm{core}} = 0.3 \pm 0.06$ determined from epoch I observations using the 1.6, 4.3, 7.6, and 15 GHz images and the values shown in the spectral index map that are near $\alpha = -0.3$ at the center of the core. This is largely a result of differing resolutions for the four bands involved in the spectral index calculation for epoch I data. The epoch II spectral index map, which uses images with matched resolutions is more robust and does not suffer from this issue.

Measurements of the spectral indices of the core and the extended structures from both epochs are consistent with reported values for blazar cores and jets from the

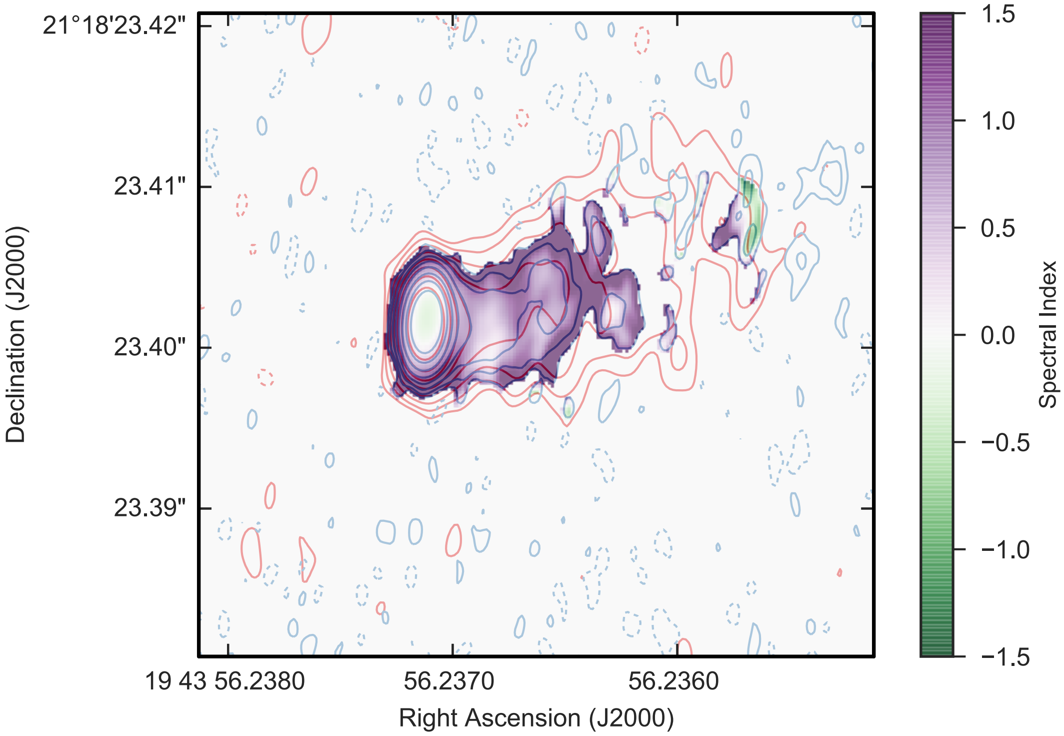

Figure 3.7: Spectral map of the core-jet structure of HESS J1943+213 radio counterpart made from epoch II VLBA 4.3 GHz and 7.6 GHz (degraded to 4.3 GHz resolution) band images, with contours for 4.3 GHz (red) and 7.6 GHz (blue) representing -1 (dotted), 1, 2, 4, 8, 16, 32, 64, 128 levels above 0.3% of the peak image intensity.

MOJAVE sample (Hovatta et al., 2014). The only available radio spectral index measurements of the core of this source come from e-MERLIN observations, which find an index of 0.03 ± 0.03 (Straal et al., 2016). The e-MERLIN observations do not resolve the source, however, and the core spectral index calculation using these observations is affected by emission from extended structures.

Comparisons between EVN and VLBA 1.6 GHz results show apparent changes in the core flux density. Gabányi et al. (2013) measured 31 ± 3 mJy for the source flux density with EVN, while the flux density measurement from our VLBA image is 23.6 ± 0.2 mJy. A similar change in the source flux density was reported by Straal et al.

(2016) between the 2011 EVN 1.6 GHz result and a lower resolution e-MERLIN 1.5 GHz detection in 2013 of the source with 22.2 ± 0.7 mJy, leading to the first variability claim for HESS J1943+213 or its counterparts in any band. As the core is not fully resolved in 1.6 GHz, however, and different configurations were used for the VLBA, EVN, and e-MERLIN observations, the claims for variability are not definitive.

e-MERLIN observations in the 5 GHz band were also obtained by Straal et al. (2016), resulting in a 22.4 ± 0.3 mJy flux density, which is significantly higher than the VLBA 4.3 GHz measurements of ∼16.2 mJy in 2015 and 17.1 mJy in 2016. The latter discrepancy could be explained by a change in the source flux density, but more likely by differences in *uv* coverage between VLBA and e-MERLIN observations and the inclusion of the jet feature in the core flux density measurement with e-MERLIN.

Despite the strong arguments for classifying HESS J1943+213 as an EHBL, a measurement of the proper motion can be a definitive discriminator between Galactic and extra-Galactic origin for the source. We attempt two sets of proper motion measurements of the HESS J1943+213 VLBI counterpart. In the first case, we compare the position measurement from our pure phase-referenced (no self-calibration) VLBA 15 GHz image from 2015 to the position reported from the Gabányi et al. (2013) EVN detection, and find a change in position of 1.1 mas. This is consistent with zero, given the ∼2.5 mas uncertainty in the position measurements, which is largely dominated by the uncertainty in the EVN position. Using this uncertainty and the ∼4.3-year time difference between the two observations, an upper limit of 47 km/s is calculated for the transverse velocity of the source at 17 kpc – the assumed distance if the source is a Galactic PWN (Abramowski et al., 2011; Gabányi et al., 2013).

In the second case, we compare the positions from our 2015 and 2016 VLBA observations using the phase-referenced 4.3 GHz images almost exactly a year apart. The 2015 VLBA observations lacked a reference source for determining an absolute source position. Hence, we make a conservative estimate of the uncertainty in the position measurements. The uncorrected atmosphere and ionosphere will contribute $< 0.1$ mas to the positional uncertainty (e.g., Hachisuka et al., 2015). The high image signal-to-noise ratio ($> 1000{:}1$) ensures that the statistical contribution to the uncertainty is well below 0.01 mas and is effectively negligible. The biggest source of uncertainty is the effect of source structure on the measurements. Source structure can complicate position measurement (1) through unmatched *uv* coverage of the two epochs leading to slight differences in reconstruction of the source and (2) through evolution of the source itself. The maximum contribution from source structure to the uncertainty in the position measurement can be estimated from the ratio of the core brightness to the local structure (in Jy/Beam). At worst, this ratio is 30:1 and the uncertainty from source structure is 1/30 of a beam width (3 × 1.5 mas), i.e. ∼0.1 mas. Thus, a conservative estimate of 0.1 mas is adopted as the uncertainty in the position measurements between the two VLBA observations.

The source position in the 4.3 GHz images is measured by fitting a Gaussian function to the core. The differences in the position measurements are 0.08 ± 0.04 mas, where the uncertainty is from the fit statistics alone. The measured difference in the position between the two epochs is smaller than the uncertainty in the position determination. We again set an upper limit on the transverse velocity. In this case, with the same source distance assumption of 17 kpc, the upper limit on the transverse velocity is 8 km/s.

The upper limits on the transverse velocity, especially the 8 km/s limit from the two epochs of VLBA observations, are much lower than typical Galactic pulsar velocities – between 100 and 300 km/s – obtained from VLBI proper motion measurements (Brisken et al., 2003). These velocity limits break the assumption that the source is located within the Galaxy and effectively rule out a Galactic origin for the source.

## 3.3 Results and Discussion

Recent publications have strongly argued that HESS J1943+213 is a blazar and results presented above, especially the VLBA measurements, firmly support and solidify this scenario. Based on the location of the synchrotron peak, HESS J1943+213 is characterized as an EHBL, a blazar subclass with very few detected members. HE $\gamma$-ray blazars behind the Galactic Plane have been previously identified with *Fermi*-LAT (Kara et al., 2012), but HESS J1943+213 is the first such blazar also seen in VHE $\gamma$-rays.

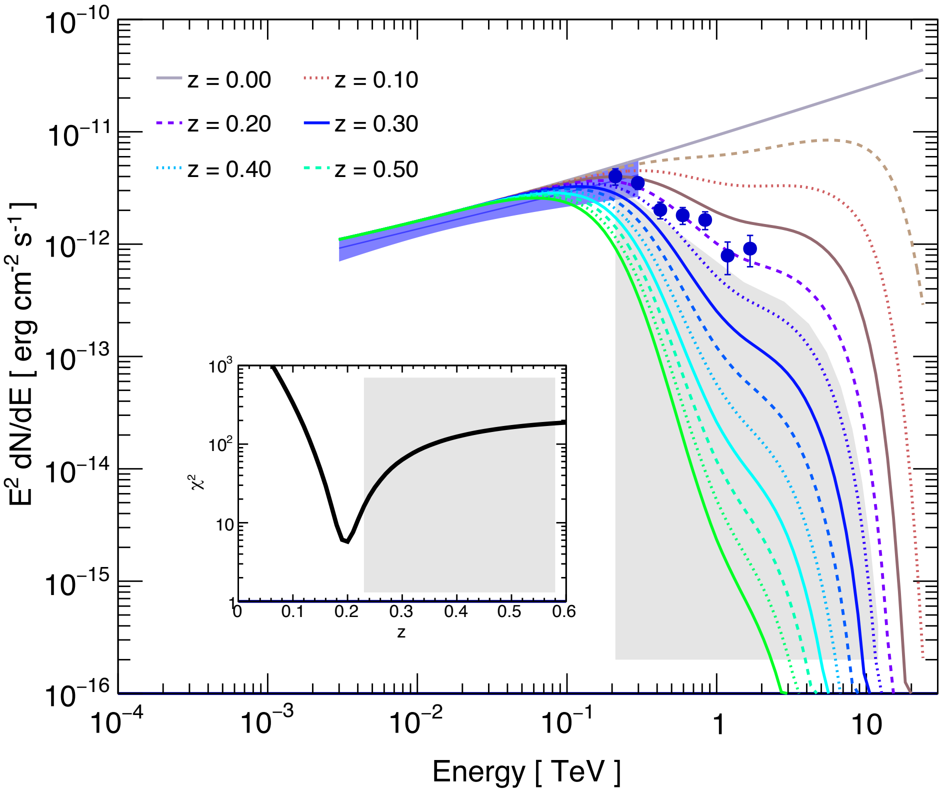

Figure 3.8: VERITAS observed spectrum (blue points) fit to upper bound of the *Fermi*-LAT spectrum absorbed by EBL for redshift values ranging from 0 to 0.6. The inset figure shows the $\chi^2$ distribution with redshift of the VERITAS spectrum fit to the EBL-absorbed extrapolations of the *Fermi*-LAT upper bound. The gray-shaded areas show the 95% rejection regions.

### 3.3.1 Redshift Constraints from Gamma-ray Spectra

The improved detection of the inverse-Compton peak with *Fermi*-LAT and VERITAS and the resulting higher-statistics spectra are used to set more robust upper limits on the redshift of the source. We use the same procedure for redshift estimation of HESS J1943+213 as Peter et al. (2014). In this method, the *Fermi*-LAT power-law spectrum is assumed to be the proxy for the intrinsic $\gamma$-ray spectrum and downwards deviations from a power-law shape are attributed to absorption effects from pair-production interactions between $\gamma$-rays and EBL photons.

Assuming a model of the EBL by Franceschini et al. (2008), the 68% upper bound of the *Fermi*-LAT spectrum is extrapolated into the VHE regime and absorbed for a range of redshift values. The upper bound of the *Fermi*-LAT spectrum is used in order for the upper limit on the redshift to be conservative. The $\chi^2$ value is calculated from the extrapolated *Fermi*-LAT upper bound and the VERITAS spectral points for each redshift value. The observed VERITAS spectrum along with the extrapolated *Fermi*-LAT upper bounds for a range of redshifts are shown in Figure 3.8. The figure also includes the resulting $\chi^2$ distribution, which shows a minimum $\chi^2$ value at $z \sim 0.20$. The 95% upper limit on the redshift derived from the $\chi^2$ distribution is $z < 0.23$, which is significantly more constraining than the existing $z < 0.45$ 95% upper limit from Peter et al. (2014).

### 3.3.2 Search for Flux Variability in X-rays and $\gamma$-rays

So far, the only claim of variability from HESS J1943+213 and its identified multi-wavelength counterparts comes from measurements of different flux densities of the radio core on milliarcsecond scales using VLBI observations (Akiyama et al., 2016).

Light curves from VERITAS and *Swift*-XRT are presented in Figure 3.2 and inset of Figure 3.3. A simple $\chi^2$ fit of a constant line to each light curve is used to test for flux variability. In addition, the fractional root mean square variability amplitude (Edelson et al., 1990; Rodríguez-Pascual et al., 1997) is calculated for each light curve, defined as $\mathrm{F}_{\mathrm{var}} = \sqrt{\frac{\sigma^2-\delta^2}{\langle f\rangle^2}}$, where $\sigma^2$ is the variance of the fluxes, $\delta^2$ is the mean square uncertainty of the fluxes, and $\langle \mathrm{f} \rangle$ is the mean flux. The uncertainty in $\mathrm{F}_{\mathrm{var}}$ is given by Equation B2 in Vaughan et al. (2003).

The long-term VERITAS light curve is stable, with $\mathrm{F}_{\mathrm{var}} = 0.23 \pm 0.37$ and $\chi^2$ / NDF = 15.6 / 12 corresponding to a p-value of 0.21 for a constant flux. There is no statistically significant evidence for variability in the *Swift*-XRT light curve composed of three observations with $\mathrm{F}_{\mathrm{var}} = 0.007 \pm 0.003$ and $\chi^2$ / NDF = 12.0 / 2 corresponding to a p-value of 0.003. In addition, there is no evidence of variability within individual XRT observations. HESS J1943+213 remains one of the most stable VHE-detected blazars.

Table 3.4. Parameters of the SSC models for the HESS J1943+213 broadband SED.

| | | |
|---|---|---|
| | GENERAL TRANSFORMATION PARAMETERS | |
| 0.16 | redshift | |
| 71 | Hubble Constant | km $s^{-1}$ $Mpc^{-1}$ |
| 2.0 | Angle to the Line of Sight | degrees |
| | BLOB PARAMETERS | |
| 26 | Doppler factor, $\delta$ | |
| $3.8\times10^{3}$ | Particle density, K | $cm^{-3}$ |
| 1.9 | First slope of particle energy spectrum, $\alpha_1$ | |
| 3.0 | Second slope of particle energy spectrum, $\alpha_2$ | |
| $8.0\times10^{3}$ | Minimum electron energy Lorentz factor, $\gamma_{\rm min}$ | |
| $5.0\times10^{6}$ | Maximum electron energy Lorentz factor, $\gamma_{\rm max}$ | |
| $2.0\times10^{5}$ | Break in electron energy spectrum, $\gamma_{\rm b}$ | |
| 0.1 | Magnetic field, B | G |
| $3.0\times10^{15}$ | Radius of emitting region, R | cm |
| | JET PARAMETERS | |
| 9 | Doppler factor | |
| $4.0\times10^{2}$ | Particle density | $cm^{-3}$ |
| 2.0 | Slope of particle energy spectrum | |
| $2.0\times10^{2}$ | Minimum electron energy Lorentz factor | |
| $1.1\times10^{4}$ | Maximum electron energy Lorentz factor | |
| 0.2 | Initial magnetic field | G |
| $7.5\times10^{15}$ | Inner radius (host galaxy frame) | cm |
| 50 | Jet length (host galaxy frame) | pc |
| 0.2 | Half opening angle of jet (host galaxy frame) | deg |
| 50 | Number of slices | |

### 3.3.3 Modeling the HESS J1943+213 Spectral Energy Distribution

The time-averaged broadband SED of HESS J1943+213 is displayed in Figure 3.9. The SED is assembled using data analyzed in this work from VERITAS, *Fermi*-LAT, *Swift*-XRT, FLWO 48″, and VLBA and archival SED points in the hard X-rays from the *Swift* Burst Alert Telescope (BAT) 70-month survey (Baumgartner et al., 2013a) and in the infrared from the Wide-field Infrared Survey Explorer (WISE) (Wright et al., 2010) all-sky survey and Calar Alto Astronomical Observatory (CAHA) 3.5 m Telescope observations (Peter et al., 2014). As noted in previous publications (Abramowski et al., 2011; Tanaka et al., 2014; Peter et al., 2014), there is no detected cutoff in hard X-rays up to an energy of 195 keV, supporting the classification of the source as an EHBL. With the improved HE and VHE spectra of the source from VERITAS and 8-year *Fermi*-LAT observations respectively, the inverse-Compton peak of the SED is well constrained.

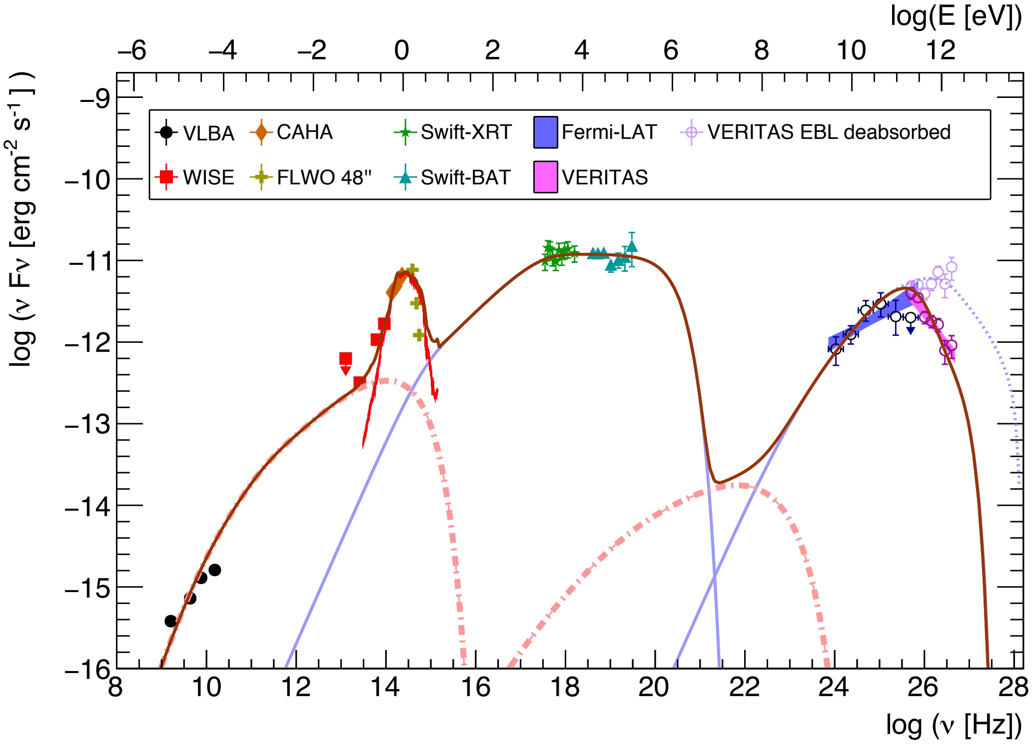

Figure 3.9: SED of HESS J1943+213, including the SSC model with components for a blob of relativistic particles (solid light blue curves) and a larger jet (dash-dotted red curves). The model for the host galaxy emission is shown in solid red, while the brown curve gives the summed emission from all model components. The flux points include data from VLA 1.4 GHz, VLBA 1.6, 4.3, 7.6, 15 GHz, WISE, CAHA 3.5 m (Peter et al., 2014), FLWO 48″, *Swift*-XRT and *Swift*-BAT, *Fermi*-LAT and VERITAS.

We attempt to model the HESS J1943+213 SED with a stationary SSC model described by a homogenous, compact blob in a conical wider jet (Katarzyński et al., 2001), assuming a source redshift of z = 0.16. The redshift value is derived by repeating the redshift estimation procedure in Section 3.3.1 with the nominal Fermi-LAT spectrum instead of the Fermi-LAT upper bound and selecting the redshift where the $\chi^2$ distribution reachers a minimum. This estimate assumes the Fermi-LAT spectrum does not deviate from a power-law function; hence, it is likely to be an overestimate if any downward curvature is present in the intrinsic source spectrum.

The SSC model assumes an emission region composed of a blob of relativistic particles containing tangled magnetic fields and moving towards Earth with a Doppler factor

$\delta$. The particle population is described by a broken power-law function with indices $\alpha_1$ and $\alpha_2$, and minimum, maximum, and break energies ($\gamma_{\rm min}$, $\gamma_{\rm max}$, and $\gamma_{\rm b}$). The size of the blob is chosen to best represent the multi-wavelength SED while staying close to equipartition and within the standard range of sizes for blazar models. The EBL model from Franceschini et al. (2008) is used to calculate the attenuation of $\gamma$-rays due to pair-production interactions for the SED model.

The SED model includes a near-IR and optical emission component from the host galaxy (using a PEGASE 2 template from Fioc & Rocca-Volmerange, 1999), which is characterized as a giant elliptical galaxy with a lower limit on the mass of $2.0 \times 10^{11}$ $M_{\odot}$. The host galaxy model fits the SED data well and is the preferred description for the near-IR SED points. A non-thermal origin for this emission is unlikely and would be impossible to accommodate within the broadband SSC model. An alternative explanation for the near-IR excess is that the emission comes from a dust torus around the central black hole. This is also unlikely, however, since strong dust torus emission is not expected for HBLs and EHBLs (e.g., Meyer et al., 2011). In addition, a bright torus would induce an external-Compton signature in $\gamma$-ray energies, which we do not observe.

With only the blob emission region and the host galaxy components, the model represents the HESS J1943+213 SED well, with the exception of the VLBA flux points of the radio core and the lowest frequency mid-IR data point from WISE. The emission region responsible for the VLBA points, however, could be distinct from the region producing the rest of the SED (e.g., Marscher, 1980b).

We model the VLBA and the mid-IR points with an additional SSC emission component from a stratified, conical jet. We adopted a two-flow model representation in which there is a highly Doppler boosted inner jet region (blob) embedded in a wider structure with a lower Lorentz factor (jet). This type of model is supported by theoretical jet approaches (e.g., Sol et al., 1989), jet production mechanisms (Blandford & Znajek, 1977; Blandford & Payne, 1982), jet launching simulations (Ferreira et al., 2006), and radio VLBI imaging (Mertens & Lobanov, 2016).

The wider jet is modeled as a cone discretized into cylindrical slices. Absorption and emission coefficients are calculated for each slice. Radiation transfer is computed in the direction of the jet propagation. The jet speed is assumed to be constant along its propagation. Jet parameters such as the magnetic field strength and particle density are provided for the first slice in Table 3.4. These parameters are calculated for the other slices following an adiabatic expansion evolution. In addition, to simulate the wider jet emission, the following constraints are applied: (1) blob velocity is greater than jet velocity, (2) radius of the jet is larger than the radius of the blob, (3) blob $\gamma_{max}$ is greater than jet $\gamma_{max}$, and (4) the jet is very close to equipartition (Hervet et al., 2015, based on Katarzyński et al. (2001)).

The two-flow model is able to represent the SED very well, only slightly underestimating the lower energy VLBA point. The $\chi^2$/NDF goodness of fit values for the blob model are $\chi^2_{\mathrm{XRT}}/\mathrm{NDF} = 3.98/10$, $\chi^2_{\mathrm{BAT}}/\mathrm{NDF} = 3.42/7$, $\chi^2_{\mathrm{LAT}}/\mathrm{NDF} = 2.30/5$, and $\chi^2{}_{\mathrm{VERITAS}}/\mathrm{NDF} = 11.25/7$ (note that NDF does not include the number of free parameters of the SED model). The parameters governing the wider jet model are poorly constrained, given there is only one synchrotron slope. As such, the physical values and the energetics of this extended synchrotron emitting zone cannot be readily deduced from the model.

The full list of values of the SED model parameters can be found in Table 3.4. The synchrotron peak is very broad and is located between $10^{18}$ Hz and $10^{20}$ Hz according to the model. The minimum variability timescale predicted by the SED model is $\sim$1.24 hours for the blob and $\sim$8.96 hours for the jet. These timescales are not contradicted by the lack of variability detection in X-rays and $\gamma$-rays, especially if the system is in a thermal equilibrium with constant particle injection. The blob emission region is out of equipartition, with the energetics dominated by the kinetic energy of the particles and $\mathrm{u}_B/\mathrm{u}_e = 0.01$, where $\mathrm{u}_e$ is the energy density in the particles and $\mathrm{u}_B$ is the energy density in the magnetic fields. The jet emission region, on the other hand, is at equipartition.

The choice of parameters for the presented model is based on a good representation of the multi-wavelength SED. Once this is achieved, an effort is made to stay close to equipartition and to reduce the total jet energetics. Parameter degeneracies, intrinsic to SSC models, cannot be fully broken by this approach. With the strong observational constraints on the synchrotron and $\gamma$-ray peaks, however, significant changes to the presented parameters will require moving away from these modeling criteria.

Given the exact distance of the source is still uncertain, changing the assumed distance value will change the intrinsic power of the source; however, the effect on the energetics equilibria including equipartition will not be significant. A higher (lower) redshift value will yield a higher (lower) energy of the emitting particles, and imply a stronger (weaker) particle acceleration mechanism. We tested models with different source redshift assumptions ($z = 0.1 - 0.2$) and obtained a range of likely parameters. The blob parameters with most significant changes are the Doppler factor (18 – 30), particle density ($8\times10^2$ cm$^{-3}$ – $4\times10^3$ cm$^{-3}$), and radius ($3\times10^{15}$ cm – $7\times10^{15}$ cm).

There have been two previous efforts to model the SED of this source. Tanaka et al. (2014) modeled the IR-to-$\gamma$-ray SED using a blackbody component for the host galaxy and an SSC component. Their SSC model includes magnetic fields with a strength of 0.78 mG, a Doppler factor of 70, and a single power-law electron distribution characterized by a spectral index of 3, $\gamma_{min} = 10^5$, $\gamma_{max} = 3 \times 10^7$. The derived variability timescale in this case is ∼28 hours and the model is far from equipartition with $u_B/u_e = 0.001$. The other SED model for the source comes from Peter et al. (2014), which represents the entire SED including the radio regime with emission from a single population of electrons and a blackbody component for the host galaxy. In this case, the magnetic field strength is 0.05 G, the electron population is described as an exponential cut-off power-law function with $\gamma_{min} = 1$, $\gamma_{max} = 10^{10}$ and the energetics are out of equipartition and dominated by kinetic energy of particles with $u_B/u_e = 0.08$.

In terms of energy requirements, our model is able to reproduce the SED with a significantly lower value for the $\gamma_{max}$ than Tanaka et al. (2014) and Peter et al. (2014) and a much lower value of the Doppler factor than Tanaka et al. (2014). The magnetic field strength in the Tanaka et al. (2014) model is lower than ours; however, this results in an emission zone that is very far from equipartition. Overall, the SED model presented in this work is able to fit the data well using more standard parameters for HBLs. In addition, the more constraining $\gamma$-ray data makes our model more robust than previous attempts.

### 3.3.4 The Role of UHECR Cascade Emission

Despite the SSC scenario providing a good description for the HESS J1943+213 $\gamma$-ray emission, and in light of HESS J1943+213 being identified as an EHBL – a promising class of objects for hadronic emission – we investigate the possibility that the VHE $\gamma$-rays originate instead from electromagnetic cascades produced by interactions of UHECRs

Table 3.5. Parameters used in modeling the $\gamma$-ray data with UHECR-induced cascade emission.

| GENERAL PARAMETERS | | |
|---|---|---|
| 124 – 1387 | Source Distance | Mpc |
| 71 | Hubble Constant | km $s^{-1}$ $Mpc^{-1}$ |
| 10 | Intergalactic magnetic field strength | fG |
| | COSMIC RAY PARAMETERS | |
| Protons only | Composition | |
| 2.0 | Index of cosmic ray spectrum | |
| 0.7 | Minimum cosmic ray energy | EeV |
| 300 | Maximum cosmic ray energy | EeV |
| 6.0 | Jet opening angle for cosmic rays | degrees |

with background photon fields. To estimate the secondary $\gamma$-ray emission from such a scenario, we simulate the propagation of UHECRs and calculate all relevant interactions using publicly-available software, CRPropa3 (for details of the software package see Alves Batista et al., 2016, or Section 3.5 for application of the code to gamma-ray spectra of blazars.).

Due to the uncertain distance of the source, multiple redshifts within the range defined by the lower and upper redshift limits are explored. The two parameters that largely determine the shape of the secondary $\gamma$-ray spectrum are the redshift of the source and the shape of the EBL spectrum. To represent the EBL, the model by Franceschini et al. (2008) is employed. The list of parameter values used for the simulation is provided in Table 3.5. The choice of intergalactic magnetic field (IGMF) strength, proton spectrum index, and maximum proton energy do not significantly affect the shape of the predicted secondary $\gamma$-ray spectrum, but can change the total cosmic ray power required to produce the secondary $\gamma$-rays by an order of magnitude. Following Essey & Kusenko (2010) a Lorentz factor of 10 is assumed, corresponding to a cosmic ray jet opening angle of 6°. If, instead, the cosmic ray emission is assumed to be isotropic, the power in cosmic rays required to generate the same flux of secondary $\gamma$-rays increases by a factor of 365.

Figure 3.10 illustrates the predicted secondary $\gamma$-ray spectra fit to the VERITAS data, with the condition that the VERITAS and *Fermi*-LAT data are not exceeded by the predicted secondary $\gamma$-ray emission. The resulting requirements on the cosmic

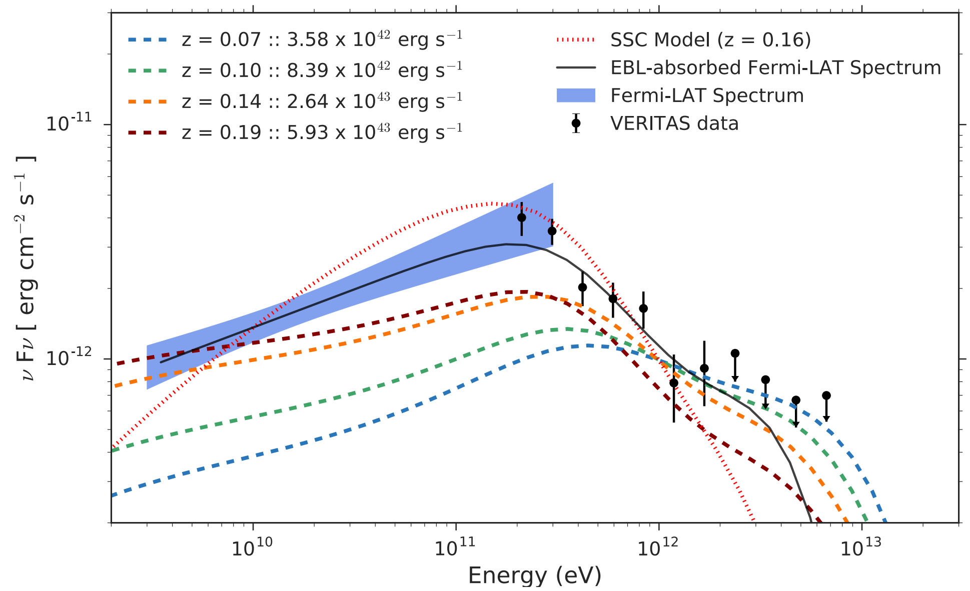

Figure 3.10: Predicted secondary $\gamma$-ray spectra from cascades initiated by UHECRs shown in dashed lines. The legend specifies the assumed distance and the UHECR power required to produce each spectrum. The solid black line shows the *Fermi*-LAT spectrum extrapolated to VHE energies and absorbed by the EBL using the model from Franceschini et al. (2008), assuming a source redshift of z = 0.16 (near the best-fit redshift value from the redshift estimation procedure in Section 3.3.1). The dotted red line is the SSC model from Section 3.3.3.

ray power for producing the secondary spectra are modest compared to the energy budgets of blazars (the Eddington luminosity of a typical $10^9$ $M_\odot$ super-massive black hole powering a blazar is $10^{47}$ erg $s^{-1}$). The shapes of the predicted secondary $\gamma$-ray spectra, however, imply that only the highest-energy end of the VERITAS spectrum – energies $> 1$ TeV – can be represented with this type of emission mechanism and only for source distances closer than z $\sim$ 0.14.

## 3.4 Summary and Conclusions

HESS J1943+213 is a new addition to the rare class of EHBLs with a strong detection in both HE and VHE $\gamma$-rays. The uncertainty over the source classification has been largely settled in favor of an EHBL with support from results presented here. The detection of a jet-like structure in VLBA 1.6 GHz, 4.3 GHz, and 7.6 GHz bands and the measurements of spectral indices comparable to other known blazars for both the radio core and the jet are strong evidence in support of this position. In addition, the lack of detectable proper motion between EVN and VLBA observations and the two epochs of VLBA observations set constraining upper limits on the transverse velocity as low as 8 km/s if the source is of Galactic origin, essentially ruling out this possibility.

Deep observations with VERITAS detect a source at the HESS J1943+213 position with $\sim$20 $\sigma$ significance, producing a high-statistics spectrum. The VHE spectral properties are consistent with the measurement from H.E.S.S.; however, the VERITAS spectrum extends down to 180 GeV energies, providing an overlap with the *Fermi*-LAT spectrum from eight years of observations. The VERITAS and the *Fermi*-LAT spectra together give an accurate description of the $\gamma$-ray peak of the source SED. These spectra are used to derive more stringent upper limits on the source redshift of $z < 0.23$.

No statistically significant evidence of flux or spectral variability is found in data from long-term VERITAS observations, as well as in *Swift*-XRT observations over the course of 4 days. As EHBLs are not known for strong variability, the stability of the source is not surprising, but still unusual.

The improved $\gamma$-ray data are used to update and model the broadband SED of HESS J1943+213. An SSC model with a component for the infrared-to-optical light from the host galaxy describes the SED very well, while keeping model parameters to standard values for HBLs. The VLBA data can also be accommodated in the model with the addition of a stratified, conical jet component. Since EHBLs are candidates for hadronic emission, a possible contribution to the $\gamma$-ray portion of the SED from secondary photons produced along the line-of-sight by UHECR-induced cascades is explored for a range of allowed distances for the source. The shape of the secondary $\gamma$-ray spectra, however, makes them viable only for >1 TeV energies and only if the source is located closer than $z \sim 0.14$.

There is still much to learn from HESS J1943+213. High-sensitivity observations of HESS J1943+213 in the hard X-ray band with an instrument like NuSTAR would be valuable for characterizing both the spectral shape and the variability of the emission produced by the higher-energy particles and would help pinpoint the emission mechanism of the source. Moreover, a precise measurement of the distance to HESS J1943+213 would be of great benefit for pinning down its physical properties. With a known distance, the stability of the source combined with its spectral properties in X-rays and $\gamma$-rays would make it an ideal target for studies aiming to constrain the strength of the IGMF and to measure the density of the EBL.

## 3.5 Application of UHECR-cascade models to blazar PKS 1424+240

**Context**: The following study was performed in collaboration with Dr. Matteo Cerruti for an in-depth SED modeling analysis of blazar, PKS 1424+240. Dr. Cerruti modeled the full SED with primary (near-source) emission models, while I modeled the gamma-ray spectrum with secondary gamma-ray emission from UHECR interactions along the line of sight.

### 3.5.1 The Distant Blazar PKS 1424+240

PKS 1424+240 is an HBL detected in VHE gamma rays by both VERITAS (Acciari et al., 2010; Archambault et al., 2014) and MAGIC (Aleksić et al., 2010). At the time of the discovery of the source in VHE gamma rays, its redshift was unknown with only a model-dependent 95% upper limit of $z < 0.66$ derived from VERITAS observations (Acciari et al., 2010). A firm lower limit of $z > 0.6035$, derived from observations of absorption lines in its UV spectrum (Furniss et al., 2013) (and later measurements of the source redshift $z \sim 0.6$ by Rovero et al. (2016); Paiano et al. (2017)), made PKS 1424+240 the most distant VHE gamma-ray emitter at the time. PKS 1424+240 is still the most distant, *persistent* emitter detected in VHE gamma-rays, though it has been surpassed by flaring-state detections of PKS 1441+25 (Abeysekara et al., 2015; Ahnen et al., 2015) and S3 0218+35 (Ahnen et al., 2016), with $z = 0.939$ and $z = 0.944$ respectively.

The VERITAS spectra of PKS 1424+240 - displayed in Figure 3.11 along with multi-wavelength SEDs for both the 2009 and 2013 observing campaigns - exhibit unusual behavior when corrected for the expected amount of gamma-ray absorption from interactions with the EBL (insets of Figure 3.11). In particular, there is a significant uptick

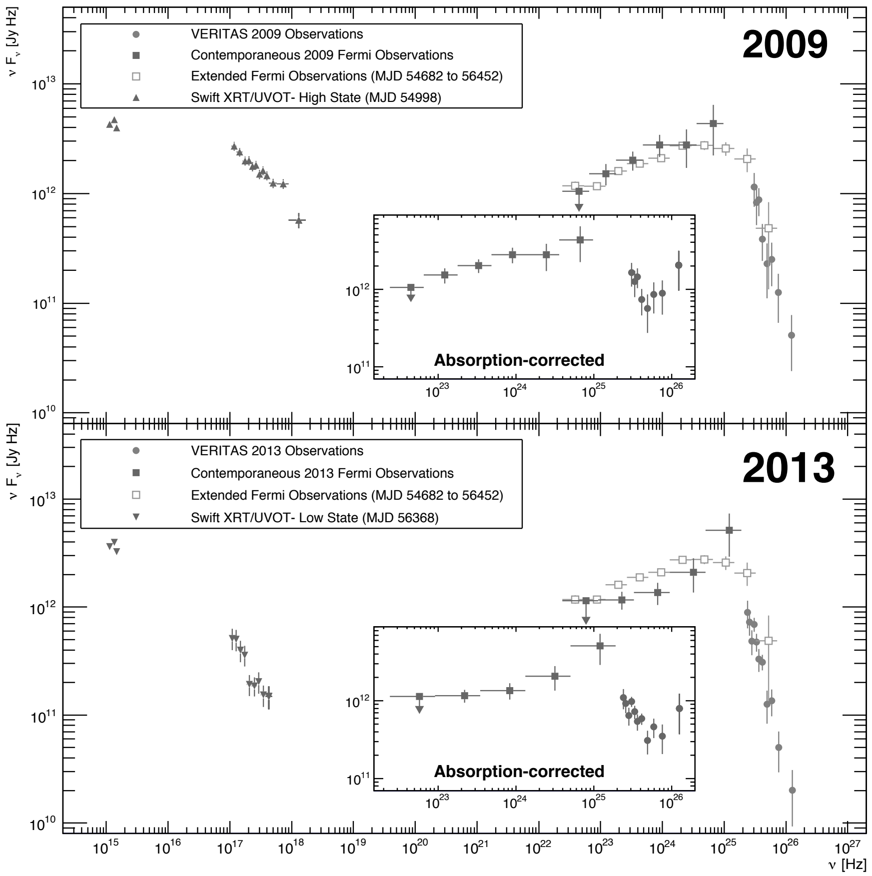

Figure 3.11: [**From Archambault et al. (2014)**] Spectral energy distributions of PKS 1424+240 from *Swift*-UVOT, -XRT, *Fermi*-LAT and VERITAS observations in 2009 (*top*) and 2013 (*bot*), with inset figures showing EBL absorption-corrected gamma-ray spectra using Gilmore et al. (2012) EBL model.

at the higher energy spectral points, which was seen as a sign for a number of emission scenarios or cosmological implications (Amy Furniss for the VERITAS Collaboration, 2015). Models were proposed to explain these observations through lepto-hadronic emission (Yan & Zhang, 2015), UHECR line-of-sight interactions with background radiation fields (Essey & Kusenko, 2014), combination of hadronic emission from the source and UHECR line-of-sight interactions (Yan et al., 2015), and even through oscillations of gamma rays into axion-like particles (Meyer & Horns, 2013).

### 3.5.2 CRPropa3

CRPropa3 (CRPropa version 3) (Alves Batista et al., 2016) is a tool to propagate UHECRs through the intergalactic medium and account for all relevant sources of energy loss. CRPropa3 is able to simulate the propagation of UHECRs and calculate their interactions along the way, including pair production, photo-pion production, photodisintegration, and nuclear decay. In addition, it can track the production and propagation of the byproducts of these interactions (secondary photons, neutrinos, and electron-positron pairs) and output spectra for the primary and the secondary particles

A Monte Carlo approach is used for propagating UHECRs in a one-dimensional (1D) or a three-dimensional (3D) environment in CRPropa3. UHECRs can be injected with a user-specified distribution in energy (power-law (with spectral index $\beta$) distribution in our case), where emission is isotropic around the source. The maximum energy of injected nuclei is given by, $E_{\max} = A \times 10^{22}$ eV, where A is the mass number. Propagation is handled step-by-step, where at each step Lorentz equations are solved and possible interactions are carried out, tracking any resulting secondary particles. CRPropa3 has functionality to model propagation in a 3D environment, which allows modeling a spatial distribution of sources and deflection effects from cosmic-ray interactions with the IGMF. In 1D mode, the code successfully models redshift evolution, but the IGMF is simplified and limited to effecting synchrotron losses from $e^+e^-$ pairs (Armengaud et al., 2007).

To model effects of cosmic-ray composition, injection of nuclei up to iron is allowed. In the case of an injected proton, the main interactions with background radiation considered by CRPropa3 are pion production and pair production by protons. Pion production is modeled using the SOPHIA package (Mücke et al., 2000), modified to encompass interactions with the EBL in addition to the CMB. Neutrinos from charged pion decay are assumed to propagate with energy loss only due to redshift, while the electromagnetic cascades are handled with code from Lee (1998). This takes care of single, double, and triplet pair-production and inverse-Compton scattering between electromagnetic products and background radiation (Armengaud et al., 2007). In addition to the above interactions, heavier nuclei can undergo photodisintegration from background photons with energies, in the nucleus rest frame, greater than the nuclear binding energy. For photodisintegration cross sections, CRPropa relies on the TALYS framework, version

1.6[4] (Koning A. J. & C., 2008) and for effects of propagating nuclei, it follows Khan et al. (2005). Nuclear decay is also accounted for in cases where photodisintegration or pion production leave behind an unstable nucleus.

### 3.5.3 Modeling Gamma-ray Spectra of PKS 1424+240 with CRPropa3

For consistency with the models of primary emission in Cerruti et al. (2017), a small modification is made by the author to the CRPropa3 code to include the Franceschini et al. (2008) EBL model in the photon propagation chain.

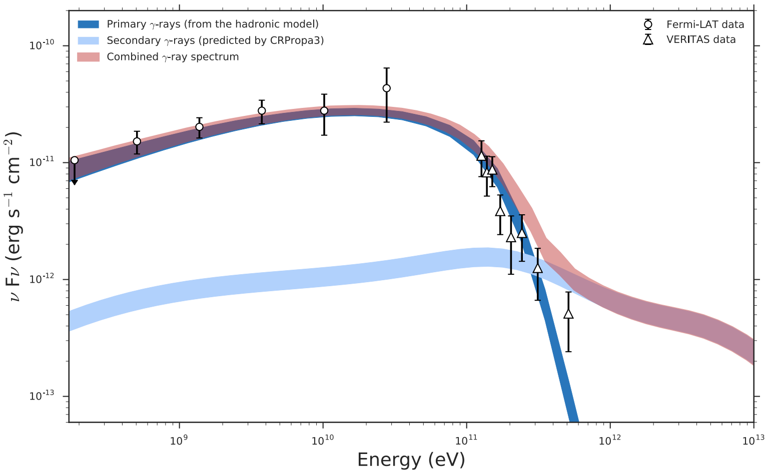

Figure 3.12: Gamma-ray emission described by the hadronic scenario together with the predicted secondary $\gamma$-ray spectra from UHECR-initiated cascades along the line of sight for the 2009 campaign.

Using CRPropa3, cosmic rays are propagated from the PKS 1424+240 distance of z = 0.6 within the 1D environment. A pure-proton composition is assumed. For the secondary $\gamma$-ray emission to be viable, the strength of the intergalactic magnetic fields ($B_{IGMF}$) cannot exceed $\sim 1.4 \times 10^{-14}$G; otherwise, deflections of the primary cosmic rays away from the line of sight are large enough for the emission from the secondary $\gamma$-rays to extend beyond the angular resolution of VERITAS and become lost in the background. Following Essey & Kusenko (2014); Yan et al. (2015), we adopt magnetic fields with a strength $B = 10^{-15}$G and a correlation length of 1 Mpc. To be consistent

---

[4] http://www.talys.eu

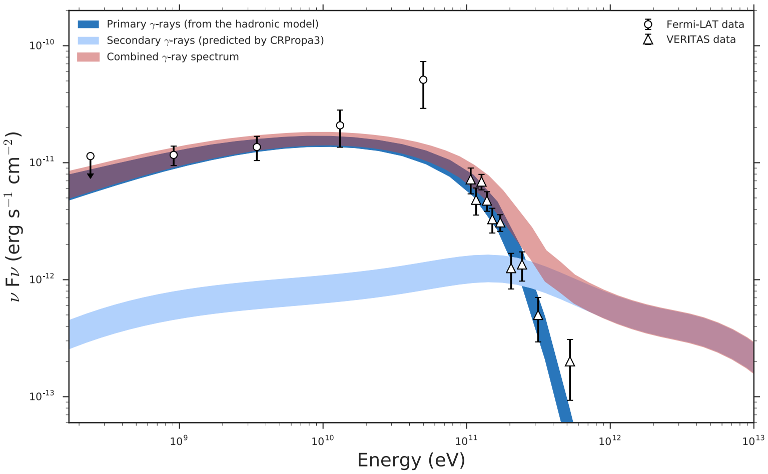

Figure 3.13: Gamma-ray emission described by the hadronic scenario together with the predicted secondary $\gamma$-ray spectra from UHECR-initiated cascades along the line of sight for the 2013 campaign.

with the treatment of the primary emission, the EBL model from Franceschini et al. (2008) is used.

The spectrum of the secondary $\gamma$-rays is calculated for two scenarios, with line-of-sight UHECR cascade emission as (1) an extension of a hadronic model of the primary emission and (2) as an additional component to a single-zone SSC model. The values of parameters used for both scenarios are listed in Table 3.6. Under the first scenario, the aim is to produce a self-consistent model of the primary and the secondary emissions from PKS 1424+240. The UHECR-generated secondary $\gamma$-rays are considered within the context of the hadronic model presented in Section 3.1 of Cerruti et al. (2017), with parameters for the secondary emission derived from the primary model. Specifically, the bulk Lorentz factor ($\Gamma$), the spectral properties ($\gamma_{min}$, $\gamma_{max}$, $\alpha_p$), and the total power of the protons (L$_p$) are taken from the hadronic model and are used to constrain the range of possible normalization of the secondary $\gamma$-ray spectra. L$_p$ is calculated using the total luminosity of the emitting region (L) and the equipartition parameter (u$_p$/u$_B$). It represents the isotropic power from a stationary spectrum of hadrons in the emitting region and accounts for energy losses at the source, including energy required for the production of the primary $\gamma$-rays. During the simulation, the UHECR spectrum is cut

Table 3.6. Parameters used in modeling the $\gamma$-ray data with UHECR-induced cascade emission.

| | Hadronic 2009 | Hadronic 2013 | SSC 2013 |
|---|---|---|---|
| z | 0.6 | 0.6 | 0.6 |
| $B_{IGMF}$ $[10^{-15}$ G] | 1 | 1 | 1 |
| Composition | protons only | protons only | protons only |
| $\alpha_p$ | -1.8 | -1.8 | -1.8 |
| $E_{min}$ $[10^{18}$ eV] 0.07 | 0.07 | 0.07 | |
| $E_{max}$ $[10^{18}$ eV] | 5.8 – 9.0 | 4.7 – 7.7 | 8 |
| $\theta_p$ [°] | 1.9 | 1.9 | 1.9 |
| $L_p$ $[10^{45}$ erg $s^{-1}]$ | 3.125 – 4.5 | 2.5 – 3.75 | 1.5 – 2.4 |

off at 0.07 EeV at the lower energy end (due to memory concerns), below which the contribution to the secondary $\gamma$-ray emission is negligible. However, the full spectrum of the UHECR extending down to 1 GeV is used for calculating the power of the UHECRs required for the production of the secondary $\gamma$-rays. The Lorentz factor, $\Gamma = 15$ determines the opening angle of the UHECRs following $\theta_p = 1/\Gamma = 3.8°$, which translates to a factor of 900 amplification of the secondary $\gamma$-ray emission over the case where UHECR are emitted isotropically. Figures 3.12 and 3.13 present the full range of possible secondary $\gamma$-ray spectra calculated for $\gamma_{max}$ and $L_p$ values from the hadronic model applied to data from 2009 and 2013 campaigns.

The second scenario treats the secondary $\gamma$-rays as an additional component to the best-fit SSC model from Section 2.1 of Cerruti et al. (2017) for describing the VHE emission. The normalization of the secondary $\gamma$-ray spectrum is far less constrained under this scenario, as the parameters of the UHECR spectrum are not predetermined. The choices for $\alpha_p$, $E_{max}$, and $\Gamma$ can vary the normalization of the secondaries by orders of magnitude while keeping the requirement on the power of the UHECRs within an acceptable range (less than the Eddington luminosity). Hence, in this scenario, we focus on the shape of the secondary $\gamma$-ray spectrum, which for a given redshift is primarily affected by the choice of the EBL model (Essey et al., 2011). For a selection of three EBL models that span the range of secondary spectrum shapes, the secondary $\gamma$-ray spectra are calculated and fit to the VERITAS spectral points with the requirement that the secondaries do not overshoot the VERITAS spectral points. The result for the

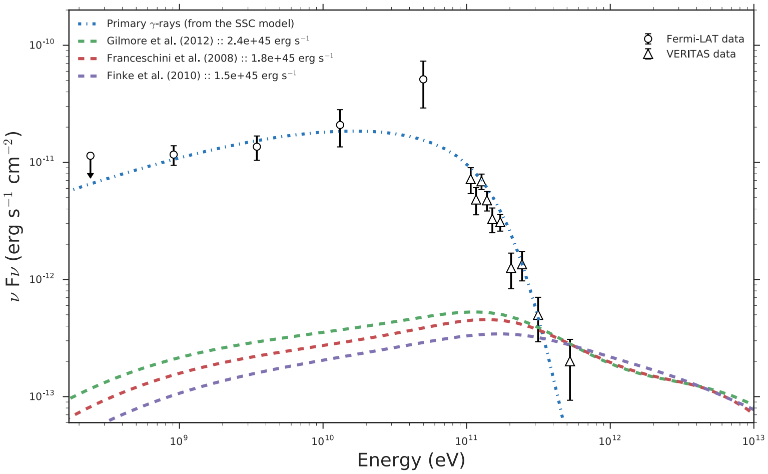

Figure 3.14: Predictions for secondary $\gamma$-ray spectra using different EBL models within the SSC scenario for the 2013 campaign. The required UHECR power for producing the secondary $\gamma$-rays is included in the legend for each EBL model.

2013 campaign shown in Figure 3.14 implies that the secondary $\gamma$-rays at best can only be responsible for the two highest energy VERITAS spectral points (results for the 2009 campaign are qualitatively identical).

# Chapter 4

# Multi-wavelength Study of Rapid Variability During the Giant Flare of Mrk 421 in February, 2010

## 4.1 Background

Markarian 421 (Mrk 421) was the first extra-galactic object seen in VHE gamma rays, discovered by the Whipple 10 m IACT in 1992 (Punch et al., 1992). It is one of the brightest objects in the VHE gamma-ray sky, even when it is in a relatively quiet state. Mrk 421 has exhibited flux variability in all observed bands (e.g., Aleksić et al., 2015). When it flares, it regularly outshines the Crab Nebula by factors of 2 – 3 and at times by an order of magnitude (e.g., Acciari et al., 2014; Aleksić et al., 2015).

Located at a redshift of $z = 0.03$, Mrk 421 is classified as a blazar (Ulrich et al., 1975). Based on the location of its synchrotron emission peak, it belongs to the HBL subclass of blazars.

Despite being one of the most studied VHE sources, Mrk 421 still offers insights and puzzles related to the mechanisms and the production location of VHE gamma rays. This chapter details the observations and data analysis of Mrk 421 during one of the brightest blazar flares observed with VERITAS, along with multi-band variability studies of the source.

Timing analysis techniques are applied to this dataset to investigate physical properties of the emission region. With the current (and the next) generation of gamma-ray instruments, the poor angular resolution makes identification of the location of gamma-ray emission in blazars impossible with direct imaging. Flux and spectral variability patterns of blazars, however, can set stringent constraints on the sizes and locations of gamma-ray emission regions and even discriminate between possible emission mechanisms.

## 4.2 The Flare

VERITAS observed an extraordinary flare from Mrk 421 on 17 February, 2010 (henceforth, referred to as *the giant flare*). This event occurred during a coordinated observing campaign led by members of the *Fermi*-LAT team. In addition to Fermi-LAT, the observing campaign included VHE facilities: VERITAS, MAGIC, and HESS; X-ray and UV observations with *Swift*, and monitoring observations by a number of ground-based optical and radio telescopes.

On 17 February 2010, VERITAS initiated observations of Mrk 421 after an alert of significant elevation of the source flux in X-rays. The real-time analysis tool QuickLook measured a gamma-ray rate of >100 gammas per minutes (corresponding to $> 10$ Crab Units) at the beginning of the Mrk 421 observations. The source remained at a similar flux level in QuickLook throughout the rest of the observations on that night.

VERITAS continued observations of Mrk 421 for the subsequent three nights (18 February – 20 February, 2010), measuring the gradual decline in flux of the source.

## 4.3 VERITAS Observations and Data Analysis

On the night of the 17 February, 2010, VERITAS observed Mrk 421 continuously for a total of 5.2 hours. Observations took place at a large range of elevations, between 83 and 34 degrees. All observations from this night were taken with only 3 telescopes in the array, due to hardware issues in T1.

For the three nights following the giant flare, a total of ∼12 hours of 4-telescope observations were obtained (5.3 hours, 3.75 hours, and 3 hours for 18, 19, 20 February, 2010 respectively). All of the temporal analysis in this chapter, however, will focus on data from 17 February, 2010, where there are sufficient statistics in the VHE observations and extended strictly simultaneous optical observations ripe for robust correlation studies.

### 4.3.1 Spectral Analysis

VERITAS observations from the night of the giant flare (17 February, 2010), as well as observations from the three following nights are used to construct time-averaged nightly spectra of Mrk 421. Together with these spectra, the spectrum from MAGIC probing the baseline state of the source before the flare is included in Figure 4.1. MAGIC had observed the source prior to the giant flare, between 6 February and 14 February, 2010.

#### Data Selection

Before analyzing VERITAS data, the quality of the observations are assessed using the VERITAS log-generator, *loggen*[1] and Data Quality Monitoring (DQM) tools. Specifically, the L3 rate and the Far-Infrared Monitor (FIR) data are used to identify time segments affected by sub-optimal weather conditions, including presence of clouds during the observations. These time segments are marked and omitted during the data analysis.

The full list of runs included in this analysis, along with information about each run, such as quality-selected livetime, On and Off counts, source significance, and gamma-ray rate are provided in Table 4.1.

#### Analysis Parameters

The VERITAS data is analyzed using the VEGAS analysis package (Cogan, 2008). Standard procedures detailed in Section 2.4 are employed for the initial stages of the analysis. These include the calculation and application of calibration information to Mrk 421 data, charge integration and image parameterization.

---

[1] https://veritasm.sao.arizona.edu/DQM/loggen.html

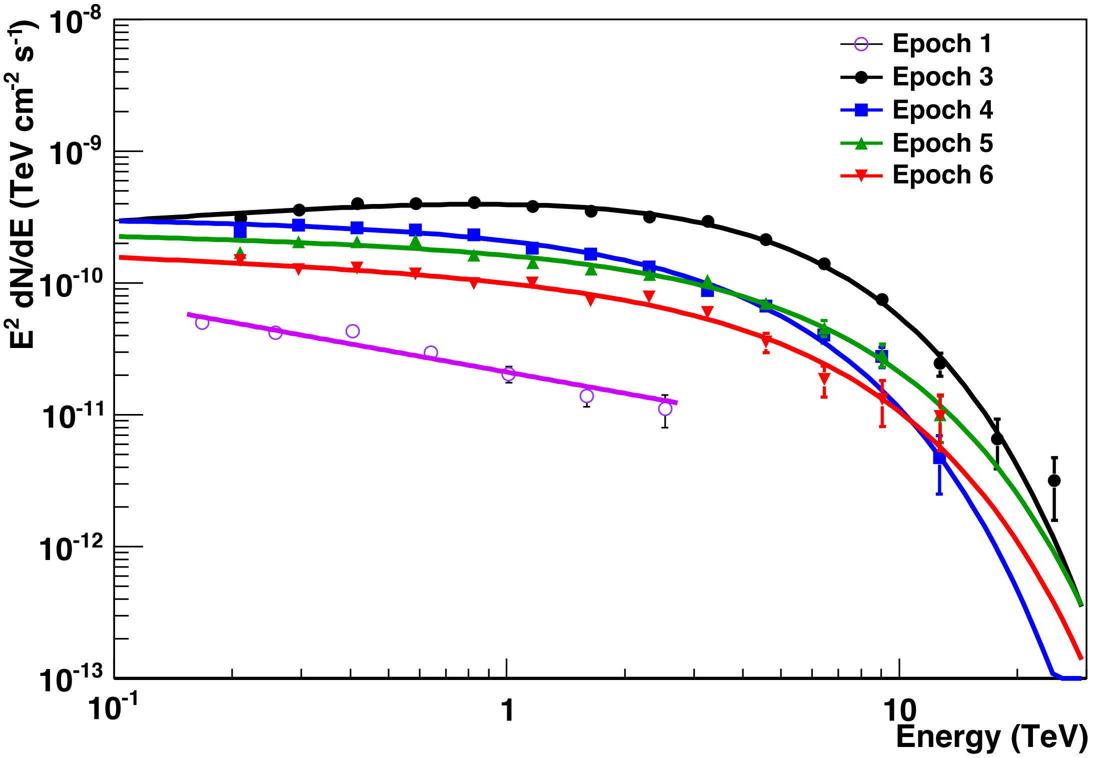

Figure 4.1: Nightly-averaged VERITAS flux spectra from the night of the giant flare (Epoch 3) and the following three (decline) nights (Epoch 4, 5, 6, respectively), along with the spectrum from MAGIC before the flare, representing the baseline state (Epoch 1). The spectral fit parameters are provided in Table 4.3 *Credit: Dr. Jon Dumm.*

As the flare is one of the brightest observed events with VERITAS, *loose cuts* are adopted for image cleaning, event separation, and size of the source region (defined by $\theta^2$ - square of the distance from the target location). The criteria associated with *loose cuts* allow the retention of more showers from high-energy events at the cost of a higher cosmic-ray background. The higher cosmic-ray rate is dwarfed by the rate of gamma rays during this event, however. The *loose cuts* criteria include a lower image size (total charge within image pixels), wider range for mean reduced scaled width and length parameters used for selecting gamma rays, and a larger $\theta^2$ cut, corresponding to a larger region for associating events with the source than in a standard analysis. Table 4.2 lists the values of the selection criteria used in the analysis.

In order to reconstruct a spectrum with VEGAS, an initial guess (a priori) of the

Table 4.1. Summary of VERITAS observations of Mrk 421 on the night of the giant flare (17 February, 2010).

| Run ID | Livetime [minutes] | On Counts | Off Counts | $\alpha^{a}$ | $\sigma$ | $\gamma$-ray rate [$s^{-1}$] |
|---|---|---|---|---|---|---|
| 50099 | 18.75 | 1461 | 94 | 0.20 | 67.5 | $76.9 \pm 2.0$ |
| 50100 | 18.74 | 1374 | 129 | 0.14 | 69.8 | $72.3 \pm 2.0$ |
| 50101 | 18.74 | 1979 | 174 | 0.14 | 84.1 | $104.3 \pm 2.4$ |
| 50102 | 18.75 | 1665 | 195 | 0.14 | 75.7 | $87.3 \pm 2.2$ |
| 50103 | 28.13 | 1849 | 194 | 0.20 | 73.6 | $64.6 \pm 1.5$ |
| 50104 | 28.13 | 1616 | 184 | 0.14 | 74.7 | $56.5 \pm 1.4$ |
| 50105 | 28.16 | 1810 | 325 | 0.14 | 76.1 | $62.6 \pm 1.5$ |
| 50106 | 28.21 | 1193 | 256 | 0.14 | 60.7 | $41.0 \pm 1.2$ |
| 50107 | 28.26 | 1770 | 177 | 0.20 | 72.3 | $61.4 \pm 1.5$ |
| 50108 | 28.33 | 1699 | 219 | 0.14 | 75.9 | $58.9 \pm 1.5$ |
| 50109 | 28.43 | 1200 | 124 | 0.14 | 67.2 | $44.4 \pm 1.3$ |
| 50110 | 19.47 | 809 | 149 | 0.14 | 50.8 | $40.5 \pm 1.5$ |

[a] Off region-source normalization.

Table 4.2. Data selection criteria used for the analysis of Mrk 421 giant flare observations.

| Criterion | Loose Cuts | Standard Cuts |
|---|---|---|
| Distance [degrees] | $< 1.43$ | $< 1.43$ |
| Size [digital counts] | $> 200$ | $> 700$ |
| Number of Pixels in Image | $> 5$ | $> 5$ |
| Mean Scaled Width | 0.05 – 1.15 | 0.05 – 1.10 |
| Mean Scaled Length | 0.05 – 1.40 | 0.05 – 1.30 |
| Shower Maximum Height [km] | N/A | 7 |
| $\theta^2$ [degrees$^2$] | 0.0256 | 0.0100 |

spectral shape is required. The spectral shape is convolved with the effective area associated with the observations to convert the distribution of excess counts with energy into the reconstructed flux spectrum. The reconstruction process is iterated until the input spectral shape matches the shape of the reconstructed spectrum. For most source detections, a power-law function is sufficient to describe the observed spectrum, with the spectral index of the power law determining its shape. The spectral reconstruction process converges to a power-law with a specific spectral index after one or two iterations.

An initial attempt to reconstruct the Mrk 421 spectrum using a power-law function of the form,

$$\frac{d\mathrm{N}}{d\mathrm{E}} = \mathrm{N}_0 \left(\frac{\mathrm{E}}{\mathrm{E}_0}\right)^{-\alpha}, \tag{4.1}$$

where $\mathrm{N}_0$ is the normalization, $\mathrm{E}_0$ is the normalization energy, and $\alpha$ is the spectral index, resulted in a strong indication of downwards spectral curvature at the higher energies. A power-law spectral shape assumption in this case biases higher energy spectral points towards higher fluxes. In order to avoid such a bias, a power-law with an exponential cutoff function is used, given by

$$\frac{d\mathrm{N}}{d\mathrm{E}} = \mathrm{N}_0 \left(\frac{\mathrm{E}}{\mathrm{E}_0}\right)^{-\alpha} e^{(-\mathrm{E}/\mathrm{E}_{cutoff})}, \tag{4.2}$$

where $\mathrm{E}_{cutoff}$ is the cutoff energy. The more complicated function requires a higher number of iterations for the spectral reconstruction to converge to a set of parameters.

With T1 out of the array during these observations, the effective areas for the 3-telescope array are modified, with some sensitivity loss at the highest energies and a higher low-energy threshold compared to 4-telescope observations. Custom 3-telescope effective area lookup tables are generated for the spectral analysis of the dataset from the night of the giant flare.

Moreover, the large range of elevation angles covered by the observations of the giant flare results in a wide range of low-energy thresholds. As Mrk 421 drops in elevation and the path length through the atmosphere grows, the fainter showers corresponding to lower energy gamma-ray events are preferentially lost, necessitating a higher low-energy threshold. A common low-energy threshold of 420 GeV is determined and used for the combined (averaged) flare-night spectrum. The same energy threshold is used for generating light curves.

### Diagnostics and Results

The analysis of VERITAS observations from the Mrk 421 17 February, 2010 flare produces one of the strongest VERITAS detections of a source in a single night.

The $\theta^2$ distribution from a *wobble* analysis is included in Figure 4.2, showing a well-contained source at the center of the field of view (in the On counts) and a well-measured background (in Off counts) used for the spectral analysis.

The excess counts map and the significance map displayed in Figure 4.4 are produced with the ring background model (RBM) analysis. Due to the extraordinary brightness of the source, the source exclusion (from background analysis) region needs to be increased to 0.6 degrees from the 0.3 degrees typically used for an average-strength source. With a smaller exclusion region, when sky maps are smoothed by a Gaussian kernel, the source leaks into regions considered for background analysis. The significance distributions (Figure 4.3) confirm that the backgrounds used in the RBM analysis are clean, with a featureless Gaussian distribution of the background left over after subtracting contributions from excluded regions (*bottom-right panel*).

The result is an incredible detection of Mrk 421 during the night of the giant flare, with 18285 excess counts (18646 On counts − 361 Off counts), corresponding to 260 $\sigma$ significance.

### Spectra

Results from the spectral analysis of 17–20 February, 2010 observations with VERITAS are provided in Table 4.3 and Figure 4.1. The spectra exhibit a cutoff at the higher energies and largely follow a trend of decreasing hardness with lower overall flux level.

## 4.3.2 Light Curve Generation

The high-statistics VERITAS data of the Mrk 421 giant flare enables construction of a finely-binned light curve, with 2-minute time bins. In order to investigate energy-dependent correlations within the VERITAS data, separate light curves are constructed

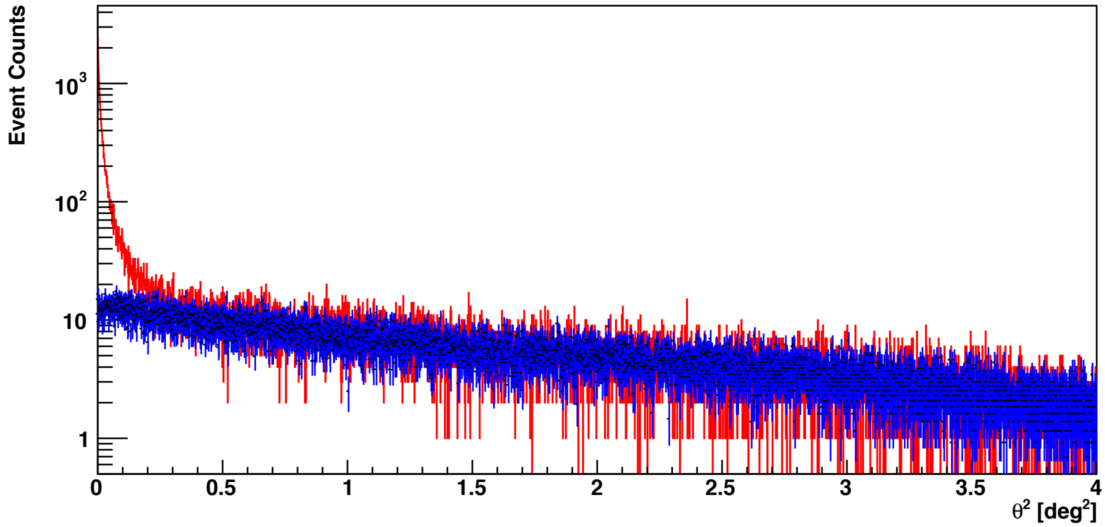

Figure 4.2: $\theta^2$ distribution of the VERITAS Mrk 421 giant flare night observations. The distribution of the On counts is shown in red, while the Off counts distribution is in blue.

for a lower-energy band, defined as 420 GeV<E<1 TeV, and a >1 TeV higher-energy band. The division at 1 TeV produces a pair of light curves with roughly equal statistics.

Within each 2-minute time bin, there are sufficient statistics to reliably reconstruct spectra and measure a spectral index. The range of energies for the spectral reconstruction for the individual time bins is limited to 420 GeV to 4 TeV and a power-law function is assumed for the spectral shape. The full light curve, without a division into two bands is used for measuring the time-resolved spectral indices.

The VERITAS light curves constructed for the lower-energy and the higher-energy

Table 4.3. Results from fits to reconstructed spectra for VERITAS observations of Mrk 421 from 17 February, 2010 to 20 February, 2010.

| Date | Flux Normalization ($N_0$) [$m^{-2}$ $s^{-1}$ $TeV^{-1}$] | Spectral Index ($\Gamma$) | Cutoff Energy ($E_c$) [TeV] | $\chi^2$/NDF |
|---|---|---|---|---|
| 17 February (giant flare) | $(5.3 \pm 0.6) \times 10^{-6}$ | $-1.76 \pm 0.02$ | $3.6 \pm 0.13$ | 34.9/12 |
| 18 February | $(2.9 \pm 0.09) \times 10^{-6}$ | $-2.03 \pm 0.03$ | $3.16 \pm 0.23$ | 36.9/10 |
| 19 February | $(2.4 \pm 0.08) \times 10^{-6}$ | $-2.23 \pm 0.03$ | $6.47 \pm 0.87$ | 23.6/10 |
| 20 February | $(1.2 \pm 0.07) \times 10^{-6}$ | $-2.11 \pm 0.05$ | $4.55 \pm 0.73$ | 12.9/10 |

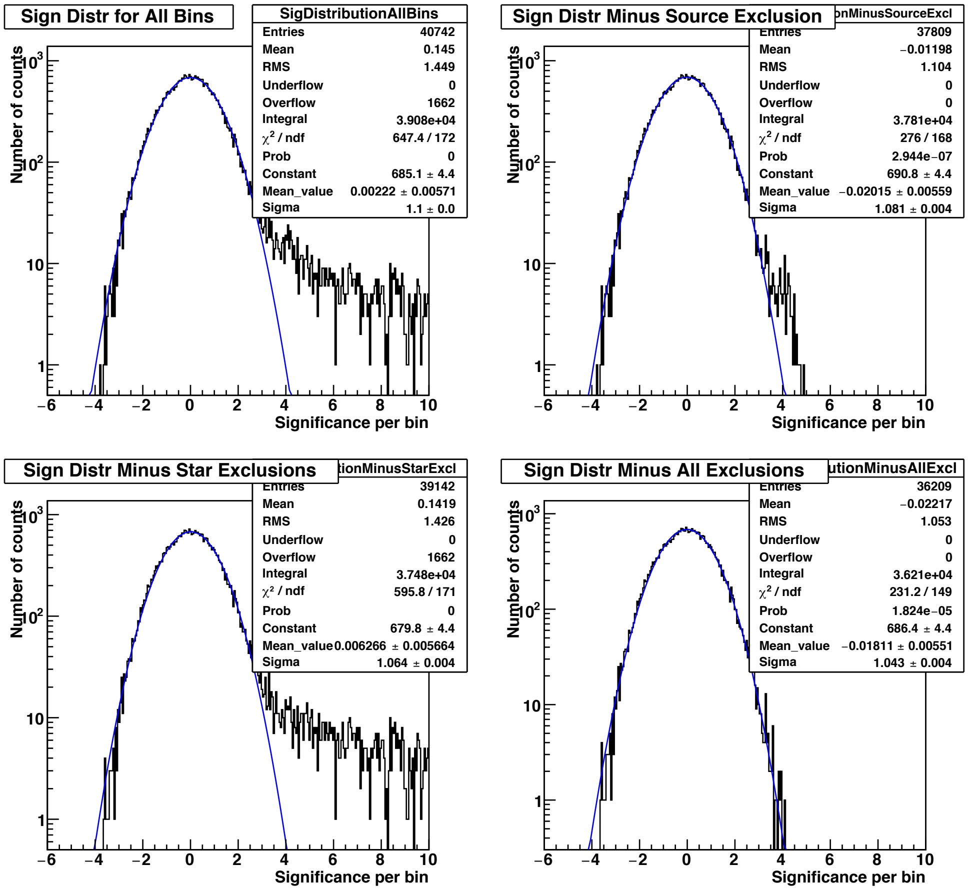

Figure 4.3: Significance distributions of the VERITAS Mrk 421 giant flare night observations.

bands, along with hardness ratio (i.e., high energy to low energy flux ratio) and spectral index are plotted in Figure 4.5.

The multi-wavelength light curves covering VHE-to-radio observations around the time of the Mrk 421 February, 2010 flare are shown in Figure 4.6. The light curves demonstrate the full breadth of the campaign on this source and give an idea of the progression of the flare. The timing analyses in this work, however, will only focus on the VERITAS and optical observations from 17 February, 2010.

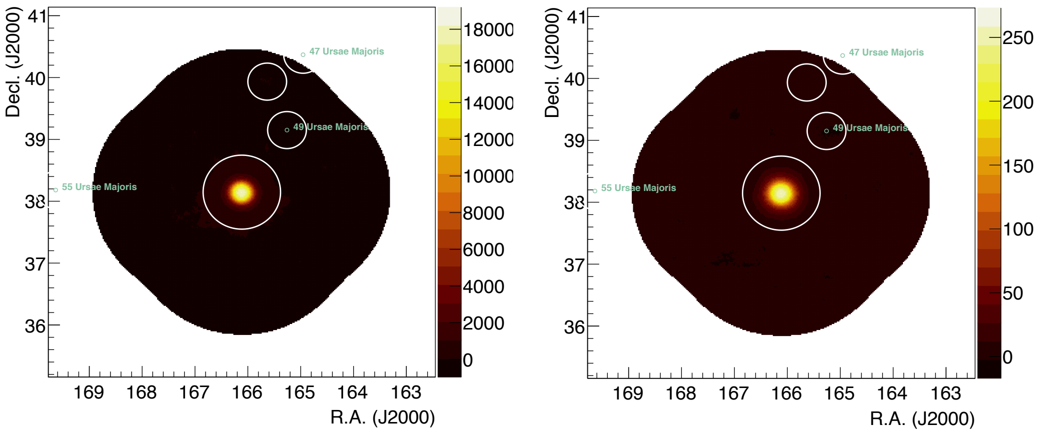

(a) Excess Map

(b) Significance Map

Figure 4.4: VERITAS excess (*left*) and significance maps (*right*) of the Mrk 421 giant flare night observations. The white circles indicate regions excluded from background estimation. The color bars display counts for the excess map and detection $\sigma$.

### Low Gain Saturation Problem

In the course of the spectral analysis of the Mrk 421 giant flare dataset, a significant problem was discovered with the pixel charge integration step of the analysis, primarily affecting the brighter and higher energy events (>3 TeV).

The spectral analysis of Mrk 421 giant flare presented here suffers from this problem. The fix to the problem is implemented and is currently in validation stage. Once the validation is completed, the data will be reanalyzed.

Note, however, that despite a significant effect on spectral reconstruction, the effect is negligible for the variability analysis presented in Section 4.4.

## 4.3.3 Optical Observations

Optical R-band observations near-simultaneous with VERITAS were obtained on 17 February, 2010 with the 1.3 m Robotically Controlled Telescope (RCT) located at Kitt Peak National Observatory and with the Crimean Astrophysical Observatory (CRAO) Shain 2.6 m telescope.

The combination of the two telescopes provides a high-cadence coverage of Mrk 421 during the giant flare, with observations occurring once every two minutes.

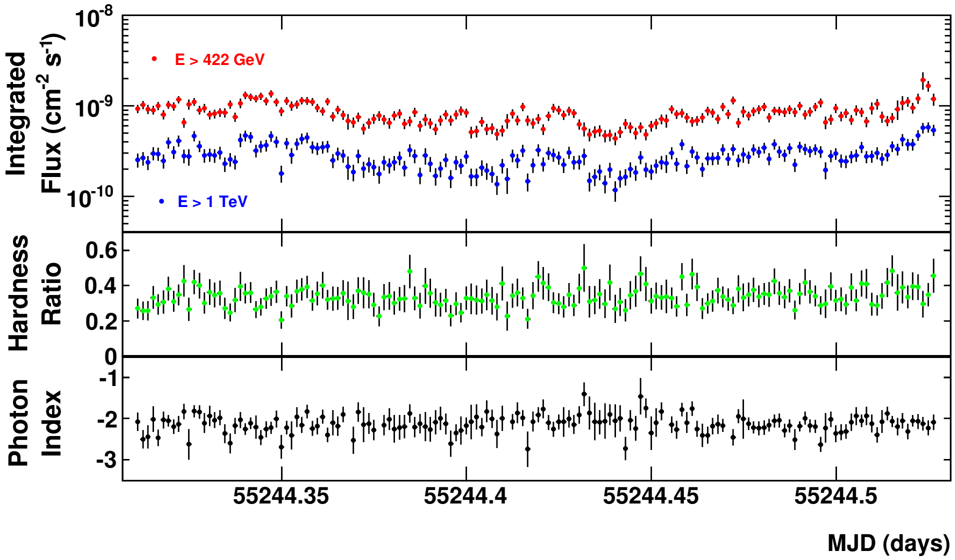

Figure 4.5: *Top panel*: 2-minute binned VERITAS light curves of Mrk 421 during the giant flare on 17 February, 2010, split into higher-energy >1 TeV band and a lower-energy 420 GeV – 1 TeV band. *Middle panel*: Hardness ratio calculating between >1 TeV and 420 GeV – 1 TeV light curves. *Bottom panel*: Photon index derived from reconstructing VERITAS spectra of Mrk 421 within each time bin.

The optical observations started ∼50 minutes after the beginning VERITAS observations and ended ∼15 minutes after VERITAS stopped observing. The 2-minute binned VERITAS and optical light curves are displayed in the *left panel* of Figure 4.12. These light curves are used in the Discrete Cross-Correlation analysis detailed in Section 4.4.2.

## 4.4 Variability Analysis of Mrk 421 Giant Flare of February, 2010

The emission regions responsible for blazar emission are typically small, located near the central black hole, and unresolvable with almost all current facilities, except perhaps with Very Long Baseline Interferometry (VLBI) (e.g., Ojha et al., 2010). Variability and timing analyses in general are powerful and at times the most effective tools for studying properties of emission regions in blazars. A number of timing analysis techniques,

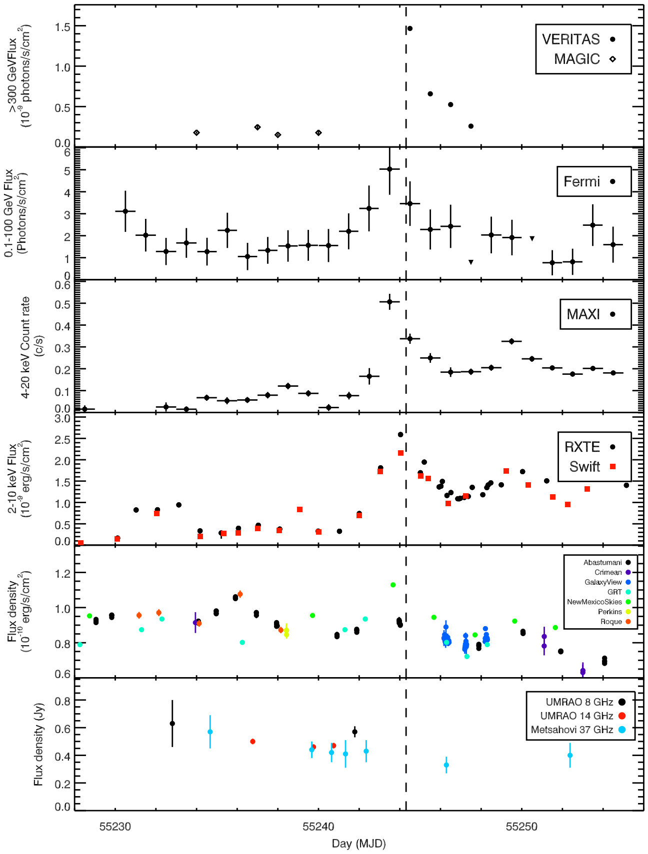

Figure 4.6: Light curves VERITAS, MAGIC, MAXI, *Swift*, RXTE, and ground-based optical and radio observatories of Mrk 421 around the time of the giant VHE flare (dashed vertical line). Credit: Dr. Tommy Nelson.

described below, are applied to the Mrk 421 giant flare dataset.

### 4.4.1 Analysis Techniques

The emission from AGN, including blazars is typically stochastic in nature. Correlation analyses can be used to characterize such signals and derive physical interpretations. The classical correlation function (CF) is defined as,

$$CF(\tau) = \frac{E\left\{[x_1(t) - \bar{x_1}][x_2(t+\tau) - \bar{x_2}]\right\}}{\sigma_1 \sigma_2}, \tag{4.3}$$

where $x$ is a function (for our use cases, typically a light curve), $E\left\{x\right\}$ is the expectation value of $x$, $\bar{x}$ is its mean and $\sigma$ is the standard deviation of $x$ (Oppenheim & Schafer, 1975). When $x_1$ and $x_2$ are distinct functions, the CF is a cross-correlation function (CCF) and can be used to measure relative lags between the two functions. Whereas, if $x_1 = x_2$, CF becomes an autocorrelation function (ACF) and measures a characteristic timescale for the function. In AGN, a lag can represent a separation between two emissions while a timescale measured from an ACF can be tied to the light-crossing time in the emitting region providing the size of the region.

For data from observations, the function $x$ is sampled within specific time bins, $t_i$ and is represented by discrete points in a light curve. The CF is then the sum of CF$_i$ computed for each time bin,

$$CF(k) = \sum_i \frac{[x_1(i) - \bar{x_1}][x_2(i+k) - \bar{x_2}]}{\sigma_1 \sigma_2}, \tag{4.4}$$

where $x(i)$ is the measurement of function $x$ in the time bin $t_i$, $k$ is an integer for shifting light curves with respect to each other ($k = 0,\ \pm1,\ \pm2,\ \dots$), and the lag timescale $\tau$ is given in terms of the light curve bin size, $\Delta t$ as $\tau = k\Delta t$.

Correlation and timing analysis techniques in general analyze a time series directly in the time domain or transform the series into the frequency domain before extracting information. Significant challenges in analyzing time series data from blazar observations (and Astronomical observations at large) are presented by uneven sampling of data, presence of gaps between observations, or differences in sensitivity between instruments or observations. The classical correlation techniques for timing analysis fail or produce faulty results for such data. Modified correlation analysis techniques have been developed to address these challenges. Below are descriptions of timing analysis techniques deemed appropriate and employed for the Mrk 421 giant flare dataset.

### Power Spectral Density

Power Spectral Density (PSD) is the distribution of power within frequency regimes (or bins, for a discrete dataset) for a given time series. The PSD of a time series data from a physical process can extract crucial information about the nature and characteristics of the process. PSDs of even poorly sampled periodic signals can provide the period or frequency for the underlying process. For stochastic processes, which have PSDs well-described by power-law functions, the power-law index characterizes the type of the signal. The non-thermal emission from AGN, and by extension blazars, is known to be stochastic in nature. In the gamma-ray regime, blazar PSDs typically have indices in the $< 1$ (pink noise or flicker noise) – 2 (red noise or random-walk noise) range (Abdo et al., 2010).

In addition to using PSDs of Mrk 421 flare light curves to characterize the associated colors of noise, PSDs are employed in this work to generate simulated light curves, necessary for assessing the significance of correlation signals.

PSDs can be expressed as the truncated Fourier transforms of finite time series. For a continuous time series, $x$, the PSD is given as,

$$\mathrm{PSD}(x) = \lim_{T\to\infty} \frac{1}{T} \int_0^T \int_0^T \mathbf{E}[x^*(t)x(t')]e^{iw(t-t')}dtdt', \tag{4.5}$$

where $T$ is the total duration of the time series, $w$ is angular frequency, $x^*$ is the complex conjugate of $x$, and $\mathbf{E}$ gives the expectation value.

The more applicable definition for real datasets is the PSD of a discrete time series. For a discrete time series, $\tilde{x}$, the PSD takes the form,

$$\mathrm{PSD}(\tilde{x}) = \frac{(\Delta t)^2}{T} \left| \sum_n^N x_n e^{-iwn} \right|^2, \tag{4.6}$$

where $\Delta t$ is the time between time series elements or the bin size of a light curve, and $N$ is the total number of samples or light curve points, such that $\mathrm{T} = \Delta t \times N$.

In practice, PSDs are usually calculated in the frequency domain, using a Fast Fourier Transform (FFT) or a direct slow Fourier algorithm. There are more advanced techniques for calculating PSDs – typically relying on the construction of periodograms (Bartlett, 1950) – that aim to accommodate unevenly sampled time series. Two of the more ubiquitous methods are Welch's method (Welch, 1967) and the Lomb-Scargle periodogram (Lomb, 1976; Scargle, 1982). Welch's method can be applied to a wide array of signal types. It splits a time series into overlapping chunks and calculates and averages periodograms within each chunk. Whereas, the Lomb-Scargle periodogram is ideal for measuring a weak periodic signal from an unevenly sampled time series.

Alternatively, PSDs can be measured directly in the time domain. Li (2001) proposed an approach that avoids Fourier transforms and periodograms, and calculates PSDs in the time domain. The promise of this approach is that it performs significantly better at the shorter timescales compared to frequency-domain methods.

For the Mrk 421 VERITAS and optical time-series data (i.e., light curves), PSDs are calculated using the *POWSPEC* program within the **XANADU** X-ray astronomical spectral, timing, and imaging software package.[2]

*POWSPEC* includes both FFT and slow Fourier techniques for calculating PSDs. The FFT method is used for the Mrk 421 data. The entirety of both VERITAS and optical light curves are used, without filtering out any part of them. Light curves are split into intervals, however, within which the power spectra are independently calculated and later averaged.

No trend removal (detrending) procedure is applied to the light curves for the final PSD constructions. For use in Section 4.4.2, this is the most appropriate approach, as the goal is to use the PSD to simulate the observed light curve, including any potential trends. The uncertainties on power in individual frequency bins are calculated as the standard deviation of the average of the power from different intervals. The resulting VERITAS and optical PSDs are displayed in Figure 4.7. The power-law fits to the VERITAS and optical PSDs give indices of $-0.9$ and $-1.3$, respectively.

The time-domain PSD estimation method from Li (2001) is implemented (in `python`) and applied to the Mrk 421 VERITAS time-series data. Preliminary results are shown in Figure 4.8. The best-fit power-law index is $-0.95$.

The time-domain PSD construction method and its implementation are not sufficiently tested and verified, however. In addition, the method requires counts data, which in this case is only available from VERITAS. Hence, the PSD construction and measurement of VERITAS and optical Mrk 421 giant flare data using *POWSPEC* are adopted for the analyses in the rest of this chapter.

### Discrete Correlation Analysis

The Discrete Correlation Function (DCF) is a workaround for applying correlation analysis to unevenly sampled time series data (Edelson et al., 1990). Unlike the classical

---

[2] https://heasarc.gsfc.nasa.gov/xanadu/xanadu.html

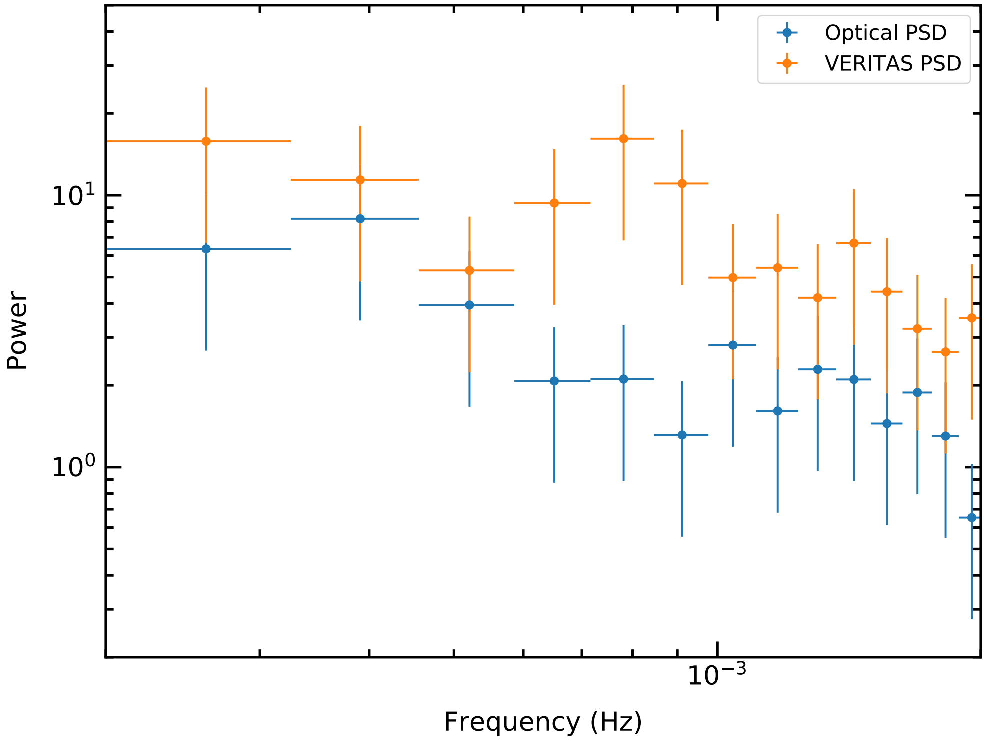

Figure 4.7: VERITAS and optical PSDs constructed from the Mrk 421 giant flare light curves.

correlation approach that uses interpolation to fill gaps within a dataset and suffers from correlated measurement errors, the DCF provides reliable estimation of uncertainties and avoids spurious power at zero lag due to these correlated errors.

For two light curves, $x_1$ and $x_2$ composed from discrete flux points, the DCF is defined as,

$$\mathrm{DCF}(\tau) = \frac{1}{M}\sum_{i,j}\mathrm{UDCF}_{i,j}, \tag{4.7}$$

with,

$$\mathrm{UDCF}_{i,j} = \frac{(x_{1,i} - \bar{x_1})(x_{2,j} - \bar{x_2})}{\sqrt{(\sigma_1^2 - e_1^2)(\sigma_2^2 - e_2^2)}}. \tag{4.8}$$

$\mathrm{UDCF}_{i,j}$ gives the unbinned pair-wise discrete correlation for individual pairs ($x_{1,i}$, $x_{2,j}$) derived from $x_1$ and $x_2$ light curves. Each pair represents a time lag, $\tau_{i,j}$ = t$_j$ - t$_i$ and

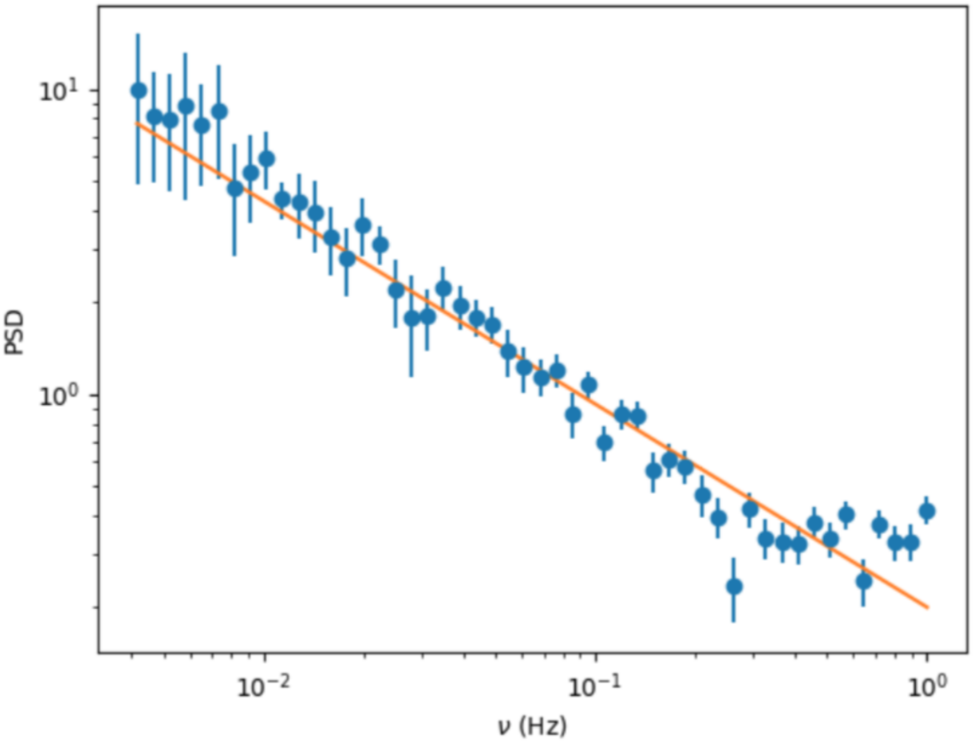

Figure 4.8: VERITAS PSD of the Mrk 421 giant flare light curve estimated in the time domain using a method from Li (2001).

the corresponding $\mathrm{UDCF}_{i,j}$ provides the pair's contribution to the correlation value on that timescale. $e_1$ and $e_2$ are the measurement uncertainties for the respective light curves and their inclusion makes the correlation calculation robust even for noisy data.

The DCF is the average over $\mathrm{UDCF}_{i,j}$ for M pairs falling within a lag bin $\Delta\tau$. It can probe time lag values at integer multiples of the light curve bins sizes, with $\tau = m\Delta t$. In the process of calculating the DCF, $\mathrm{UDCF}_{i,j}$ from pairs where $i = j$ are excluded. This guards against potential correlated errors and spurious power at zero lag time.

The uncertainty in DCF is given by,

$$\sigma_{\mathrm{DCF}}(\tau) = \frac{1}{M-1}\sqrt{\sum[\mathrm{UDCF}_{i,j} - \mathrm{DCF},(\tau)]^2} \tag{4.9}$$

with the assumption that $\mathrm{UDCF}_{i,j}$ contributing to a given bin are uncorrelated. If correlation exists, which can occur if one or both of the light curves have significant autocorrelation on timescales larger than the lag bin size, the denominator $(M-1)$ is replaced with $\sqrt{[(M-1)(M'-1)]}$, where $M'$ gives the number of uncorrelated $\mathrm{UDCF}_{i,j}$.

The DCF calculation is performed using code from Robertson et al. (2015). In order to apply the DCF method to the Mrk 421 February 2010 flare data, DCF is first used on simulated light curves to calibrate confidence levels for different lag times.

The minimum time bin size is set by the 2-minute binned optical light curve. The VERITAS data has a much finer time resolution (∼0.0025 seconds), with time tags available for individual gamma-ray events. For calculating the DCF, the VERITAS light curve is constructed with 2-minute bins to match the optical. Simulated light curves are fixed to 2-minute bins as well.

### Modified Correlation Analysis

A modified correlation analysis was proposed by Li (2001) and aims to perform timing analysis directly within the time domain. The primary advantage of this approach is greater sensitivity and reliability on shorter timescales, down to the time resolution of an instrument. The method can be applied to a single light curve to obtain an autocorrelation function and measure the duration of variability or to pairs of light curves to derive the cross-correlation function and look for lags. In addition, Li (2001) rederive other temporal properties, such as hardness ratio, and coherence in the timing domain.

The modified cross-correlation function ($MCCF$) is obtained from the classical correlation function given in Equation 4.4 by redefining it as a function of the lag time $\tau$, with $\tau = k\Delta t$,

$$MCCF(\tau) = \sum_i \frac{(x_1(i\Delta t) - \bar{x_1})(x_2(i\Delta t + \tau) - \bar{x_2})}{\sigma_1 \sigma_2}, \tag{4.10}$$

where $x(t)$ is the number of counts in time bin $(t, t+\Delta t)$. For this modified correlation function, however, $\tau$ is no longer constrained to be an integer multiple of the light curve bin size, $\Delta t$ and can be incremented by the time resolution element, $\delta t$. The $MCCF$ can then be calculated for lag times, $\tau = m\delta t$ (with $m = 0, \pm1, \pm2, \ldots$) for

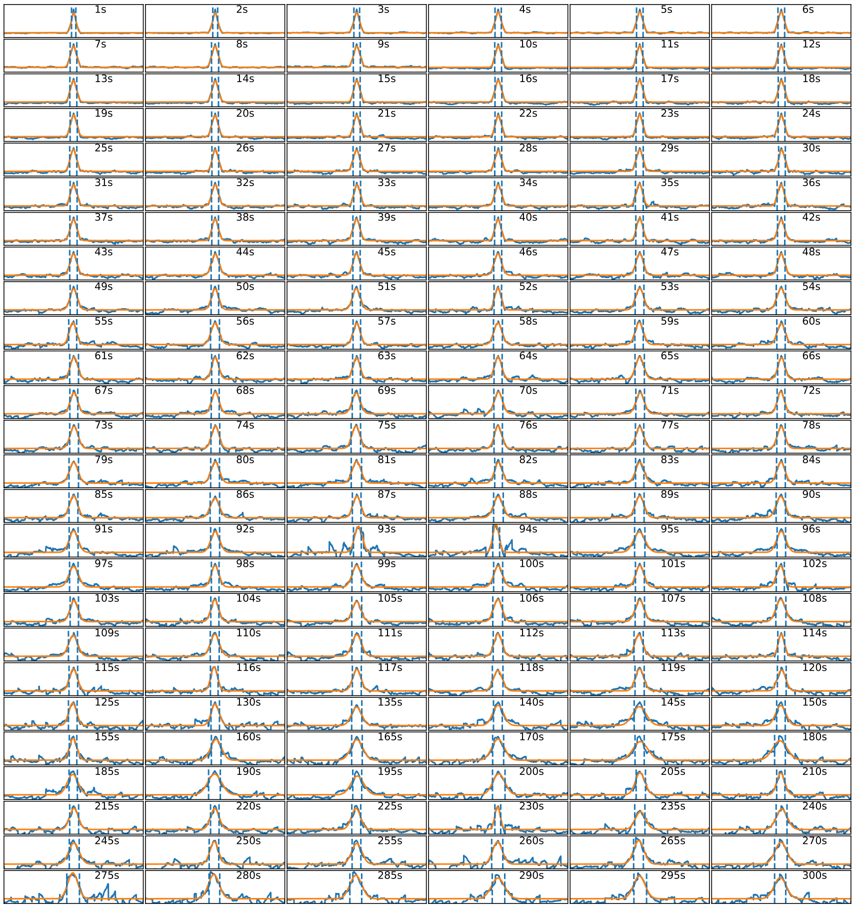

Figure 4.9: MACFs calculated for timescales between 1 s and 300 s in solid blue curves. Each MACF is fit to a Gaussian function in solid orange, from which FWHM is estimated. Dashed blue vertical lines show the FWHM calculated directly from each MACF.

light curves with a given timescale $\Delta t$. The timescale corresponding to the maximum of $MCCF(k\delta t)/MCCF(0)$ gives the lag time between $x_1$ and $x_2$.

From the definition of $MCCF$, the modified autocorrelation function ($MACF$) is obtained by setting $x_1 = x_2$,

$$MACF(\tau) = \sum_i \frac{(x(i\Delta t) - \bar{x})(x(i\Delta t + \tau) - \bar{x})}{\sigma^2}. \tag{4.11}$$

The FWHM (full-width at half maximum) of the $MACF$ is a measurement of the variability duration. The maximum of FWHM$_{MACF}/\Delta t$ may be treated as a characteristic timescale for the time series.

The MACF calculation is implemented in `python` for use in this analysis.

### 4.4.2 Results from Correlation Analyses

#### Modified Autocorrelation Analysis of VERITAS Observations

MACFs described in Section 4.4.1 are calculated for the VERITAS time-series data to investigate variability properties on short timescales.

In order to apply the technique, a time-tagged list of VERITAS events is extracted for the source region. As background subtraction is not possible on individual event basis for VERITAS data, the list of events is inevitably contaminated by background events. Based on the count rates of source and background regions for this dataset, on average only ∼3% of the events are from background and are likely to be negligible in the MACF calculation. Background events will not create any spurious correlations; however, in significant quantities they can dampen a potential correlation signal from the source events.

MACFs are calculated for 1–300 seconds timescales for the VERITAS events. The resulting MACFs along with Gaussian fits and FWHM estimations are displayed in Figure 4.9. The distribution of MACF FWHM measurements for the sampled timescales are presented in Figure 4.10, showing potential hints of *excess variability* on timescales greater than 50 seconds. There are no obvious peaks, however, to associate with a characteristic variability timescale. Moreover, the significance of any signal will need to be assessed by a Monte Carlo treatment, which is beyond the scope of this chapter.

#### Discrete Autocorrelation Analysis of VERITAS and Optical Observations

The VERITAS and optical light curves along with their discrete autocorrelation functions (DACFs) are displayed in Figure 4.11. Before calculating the autocorrelation functions, the light curves are mean-subtracted; however, no additional detrending is performed.

The presence of any significant autocorrelation is important to identify and account

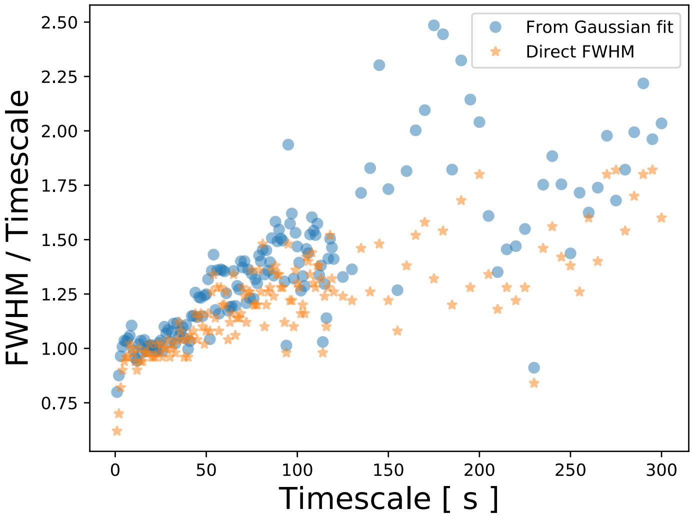

Figure 4.10: Distribution of FWHMs of MACFs (estimated directly or by fitting Gaussian functions as shown in Figure 4.9) for sampled timescales.

for before investigating the cross-correlation function to avoid spurious signals in the latter. As there are no obvious peaks in the DACFs, except at zero lag, we can proceed with cross-correlation analyses.

### VERITAS-optical Discrete Cross-Correlation

The VERITAS and optical light curves, as well as the discrete cross-correlation function (DCCF) of the two are shown in Figure 4.12. The DCCF is calculated after subtracting the mean from each light curve and dividing the result by the standard deviation. No additional detrending is performed. There is a broad peak apparent in the DCCF, including a bump at a time lag of roughly 35 minutes, with VERITAS leading the optical. For qualitative assessment purposes, the VERITAS light curve is delayed by 35 minutes and overlaid on top of the optical light curve (bottom-right panel of Figure 4.12).

In order to assess the significance of any features in the DCCF, including the broad peak, a method similar to (Max-Moerbeck et al., 2014) is employed. The method involves performing Monte Carlo simulations of the DCCF to assemble a probability density function of the correlation coefficient for uncorrelated light curves.

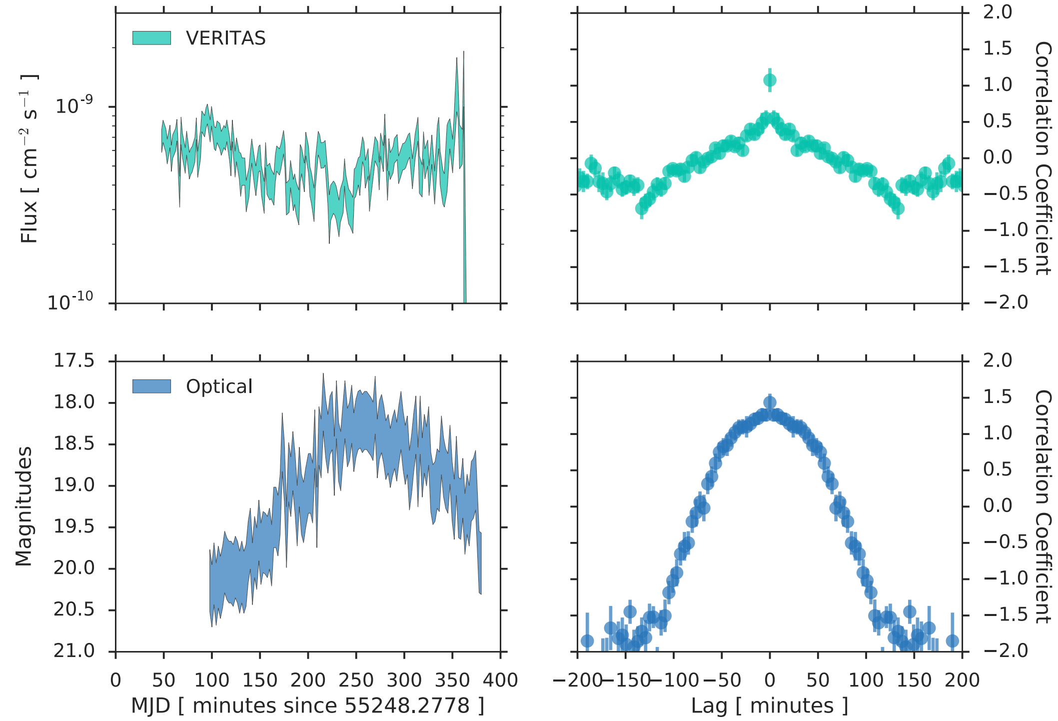

Figure 4.11: *Left panels*: 2-minute binned VERITAS and optical light curves. *Right panels*: The discrete autocorrelation functions for the VERITAS and optical light curves.

Simulated light curves representing the VERITAS light curve are constructed using the power spectrum of flicker noise (or pink noise) with $P(f) \propto f^{-0.9}$. The spectral index is from the best-fit power-law function for the PSD constructed from the VERITAS light curve in Section 4.4.1. Since the uncertainties in the VERITAS PSD are substantial, the effect of using different power-law index for the PSD to simulate VERITAS light curves were explored. Lowering the magnitude of the index (approaching white noise) has the effect of increasing the significance of the cross-correlation signal in the observed DCCF; while increasing the magnitude of the index (approaching red noise) lowers the significance.

Instead of using the power spectrum to generate simulated light curves, the optical light curve is rearranged or scrambled by cutting a randomly-sized chunk from its end and moving it to the beginning. The latter is not strictly necessary, since a simulated VERITAS light curve should not be correlated with the original optical light curve. In

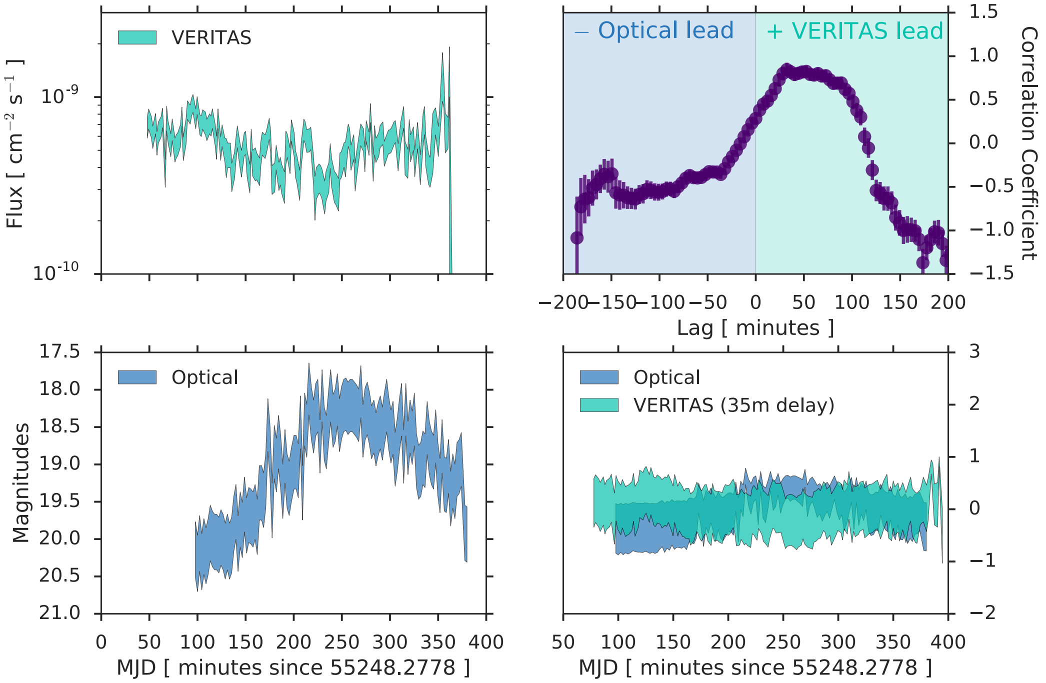

Figure 4.12: *Left panels*: 2-minute binned VERITAS and optical (RCT and CRAO) light curves. *Top right panel*: The discrete cross-correlation function for the VERITAS and optical light curves. *Bottom right panel*: Same VERITAS and optical light curves as on the left, but scaled to a mean of zero. The VERITAS light curve is lagged by 35 minutes, corresponding to the bump in the DCCF. The uncertainties of the optical light curve are inflated within this panel for better visualization.

addition, using the original optical light curve gives the more conservative estimates of the significance levels, as any trends in the observed optical light curve that may give rise to spurious cross-correlation power will be accounted for in the simulated DCCFs.

The DCCF is calculated for 100,000 simulated light-curve pairs. To obtain matched data pairs for a given lag a weighting by a Gaussian or a "top-hat" kernel is applied. The Gaussian weighting has an effect of smoothing the resulting DCCF, which can be useful for identifying features in noisy data. Figure 4.13 shows the resulting DCCFs binned into a 2D histogram of lag time bins along with the DCCF calculated from VERITAS and optical data for both weighting schemes. In this iteration, the optical light curve is scrambled. The vertical bins of the binned DCCFs from simulated light

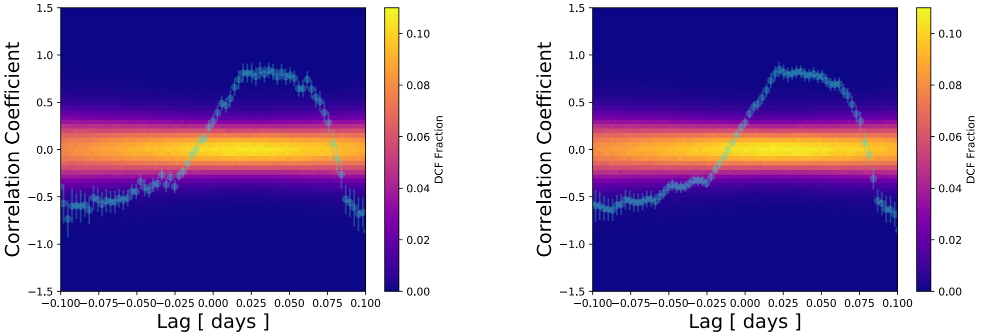

Figure 4.13: Simulated DCCFs binned in 2D using scrambled optical light curves (*left* – top-hat weighted, *right* – Gaussian weighted). The DCCF from observations is in light blue.

curves are normalized such that each bin gives the fraction of all DCCFs falling within the bin, and for a given lag (horizontal) bin, the vertical bins will sum to 1. Using the simulated DCCFs, the significance of correlation can be estimated for each of the points in the DCCF from the VERITAS and optical data. This is done by integrating the probability density function represented by the simulated DCCFs from a correlation coefficient of 0 up to bins located within the $1\sigma$ range of the observed DCCF point. The results are shown in Figure 4.14. The VERITAS-optical DCCF shows a potential signal at lag times of 30–70 minutes. The significance of the correlation is $3$–$4\sigma$. With the more conservative approach of pairing the original optical light curve with simulated VERITAS light curves, the confidence level calibration is qualitatively similar to the scrambled optical light curve case, but with more modest cross-correlation significance ranging between $2.5\sigma$ and $3\sigma$ (see Figure 4.15).

A $\sim 3\sigma$ significance of VERITAS-optical discrete cross-correlation is not a definitive evidence for a real signal. Autocorrelated signal in either VERITAS or optical light curves can contaminate the cross-correlation measurement. No such signal is apparent in the discrete autocorrelation of the VERITAS light curve, however. Moreover, using the original optical light curve for confidence interval calibration should negate contribution from any autocorrelated optical signal.

Time lags between optical and gamma-ray have previously been previously reported. Cohen et al. (2014) detected lags between optical and *Fermi*-LAT light curves

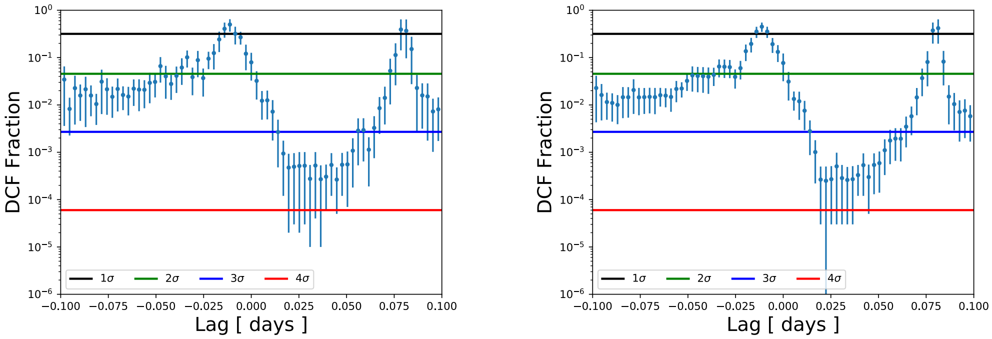

Figure 4.14: Significance of VERITAS-optical cross-correlation with simulations using scrambled optical light curves (*left* – top-hat weighted, *right* – Gaussian weighted). The black, green, blue, and red lines show the $1\sigma$, $2\sigma$, $3\sigma$, and $4\sigma$ levels respectively.

of blazars, with lag timescales on the order of ∼1 day to ∼10 days. Lags on timescales of tens of minutes observed for the giant flare of Mrk 421 are unique. It should be noted that this flaring episode of Mrk 421 and the VHE gamma-ray statistics of the resulting dataset are extraordinary, with the only comparable dataset available from the July, 2006 flare of blazar, PKS 2155-304 (Aharonian et al., 2009). In this case, strong correlations were found between the VHE and X-ray bands, but no time lags were observed.

Lags between radio and gamma rays have been associated with the motion of the emitting region responsible for both bands, with a corresponding distance traveled expressed as,

$$d = \frac{\Gamma \delta v \Delta t}{1+z}, \tag{4.12}$$

where $\Gamma$ is the bulk Lorentz factor, $\delta$ is the Doppler factor, $v$ is the velocity of the region, $z$ is the source redshift, and $\Delta t$ is the observed time lag between bands (Pushkarev et al., 2009).

To properly apply this estimate to the observed time lag, an SED model of the flare dataset would be required to constrain $\delta$. $\beta$ can be measured with VLBI monitoring or it can be approximated if the jet angle to the line of sight is known. Neither quantity is available for the night of the giant flare. However, models of the Mrk 421 SED from the decline period indicate that $\delta \sim 25$. The resulting distance is $d = 0.01 - 0.025$ pc,

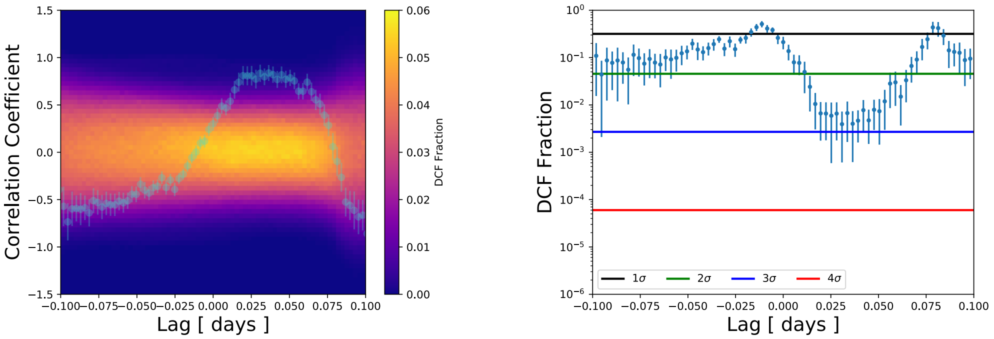

Figure 4.15: *Left*: Simulated DCCFs for VERITAS and unscrambled optical light curves binned in 2D, with top-hat weighting. The DCCF from observations is in light blue. *Right*: Significance of VERITAS-optical discrete cross-correlation. The black, green, blue, and red lines show the $1\sigma$, $2\sigma$, $3\sigma$, and $4\sigma$ levels respectively.

for the 30–70-minute time lag. This distance is significantly larger than the size of the emission region from the same SED models, $r_e = 0.001$ pc.

The more likely cause of the time lag, assuming a an SSC scenario, is the faster cooling rate of the higher energy electrons through inverse-Compton scattering compared to the slower cooling rate of the lower-energy electrons through synchrotron radiation.

# Chapter 5

# MS1221.8+2452: Flaring Blazar Detection

## 5.1 Introduction

MS 1221.8+2452 is classified as a high-frequency peaked BL Lac object (HBL) (Sbarufatti et al., 2005). It is one of a handful blazars imaged by the Hubble Space Telescope (Jannuzi et al., 1997). The high resolution HST imaging detected the host, which is an isolated, elliptical type galaxy. At a moderate redshift of z=0.218 (Stocke et al., 1991; Sbarufatti et al., 2005; Ahn et al., 2014), MS 1221.8+2452 is a promising source for EBL studies that rely on gamma-ray spectra of blazars.

In the VHE gamma rays, MS 1221.8+2452 has been previously detected by the MAGIC Collaboration (Cortina, 2013) over the course of 4 hours of observations at greater than $5\sigma$ significance and $\sim$4% Crab Nebula flux above 200 GeV. No published VHE spectrum exists for this source, however.

This chapter presents observations of MS 1221.8+2452 during a VHE gamma-ray flare event. Over the course of this flare, the source is detected in VERITAS with 16.5 $\sigma$ significance, leading to the first VHE gamma-ray spectrum of the source. Moreover, using contemporaneous multi-wavelength observations, the observed broadband SED of the source around the time of the VHE flare is constructed, showing that a simple SSC model can sufficiently characterize the emission. The variability characteristics of MS 1221.8+2452 during the flare are also investigated, with a focus on the X-ray emission.

Table 5.1. Summary of VERITAS observations.

| Exposure Range (MJD) | RunID | Exposure (min) | On Counts | OFF counts | $\alpha$ | Significance |
|---|---|---|---|---|---|---|
| 56686.4835 – 56686.4946 | 71886 | 16 | 28 | 27 | 0.10 | 7.95 |
| 56687.4269 – 56687.4478 | 71906 | 30 | 28 | 86 | 0.09 | 5.20 |
| 56687.4484 – 56687.4693 | 71907 | 30 | 29 | 66 | 0.11 | 5.53 |
| 56687.4696 – 56687.4904 | 71908 | 30 | 25 | 76 | 0.09 | 4.94 |
| 56687.4954 – 56687.5163 | 71909 | 30 | 36 | 61 | 0.11 | 7.12 |
| 56687.5170 – 56687.5379 | 71910 | 30 | 46 | 63 | 0.09 | 9.55 |

## 5.2 Multi-wavelength Observations

MS 1221.8+2452 gamma-ray data from VERITAS and *Fermi*-LAT, X-ray data from *Swift*-XRT, ultraviolet and optical data from *Swift*-UVOT are available for the VHE flaring period. This section briefly details properties of instruments used for observing the source and describes the available data, the data analysis, and the results obtained for observations with each of these instruments.

### 5.2.1 VERITAS

VERITAS first observed MS 1221.8+2452 for 960 seconds on 29 January, 2014 as part of an observing program aiming to catch blazars in elevated states with 15-minute snapshots. The source was seen at ∼20% Crab Nebula flux state in the next-day automated pipeline and confirmed through a dedicated analysis. Target-of-opportunity observations were triggered for the following three days, though only data from 30 January was usable due to poor weather conditions at the VERITAS site on 31 January and 1 February. VERITAS performed subsequent observations of MS 1221.8+2452 on 3 February, at which point the source no longer appeared to be in an elevated state. This remained unchanged in snapshot observations over the course of the next two months. VERITAS has observed MS 1221.8+2452 for over 10 hours since the 2014 flaring episode, with no indications of a signal.

All observations were made in the "wobble" mode (see Section 2.2), with a tracking position offset by 0.5° from the source position, and changing offset direction (N, E, S, W) for successive exposures of the source.

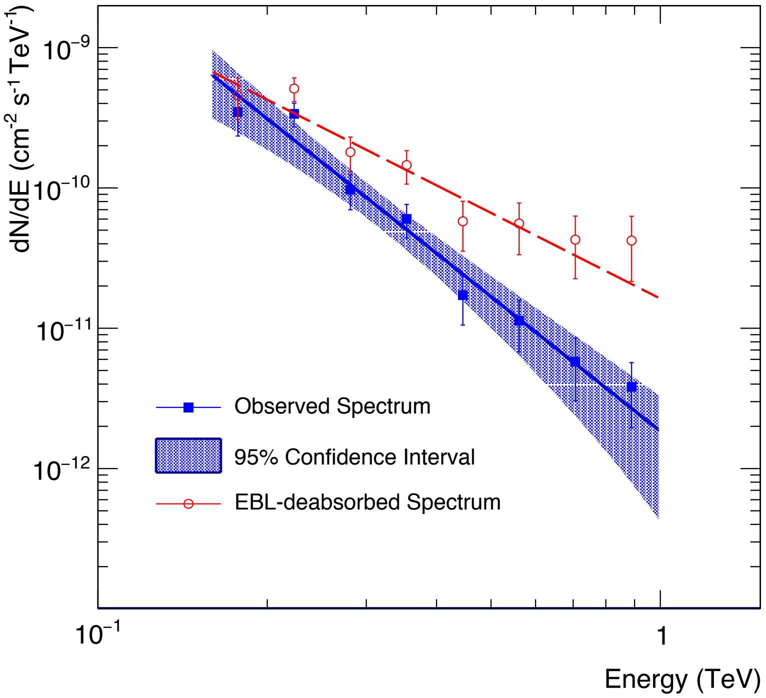

Figure 5.1: Observed VERITAS spectrum of MS 1221.8+2452 with 95% confidence interval for a power-law fit in blue and EBL absorption-corrected spectrum using Gilmore et al. (2012) in red.

VERITAS observations of MS 1221.8+2452 are analyzed using VEGAS, following analysis methods described in Section 2.4. Camera images of Cherenkov showers are parameterized in terms of the standard Hillas parameters (Hillas, 1985). Comparisons of these parameters to simulations are used to reconstruct shower properties, which in turn are used to estimate the energy and arrival direction of primary particles (Section 2.4.4). Gamma-ray showers are separated from hadronic ones using the standard VEGAS cuts on shower properties and the arrival direction of the primary particle, optimized for a moderate source flux and spectral properties (Section 2.4.6).

Spectral reconstruction is performed with source counts measured from a circular region centered on the position of MS 1221.8+2452. For each exposure, background counts are determined from identically-sized circular regions arranged at the same distance (0.5°) from the tracking position as the source region. The background estimation with this method ensures that both source counts and background counts are taken from regions with similar gamma-ray detection efficiency. Source significance is calculated with the binned likelihood ratio method from Li & Ma (1983) (Section 2.4.7).

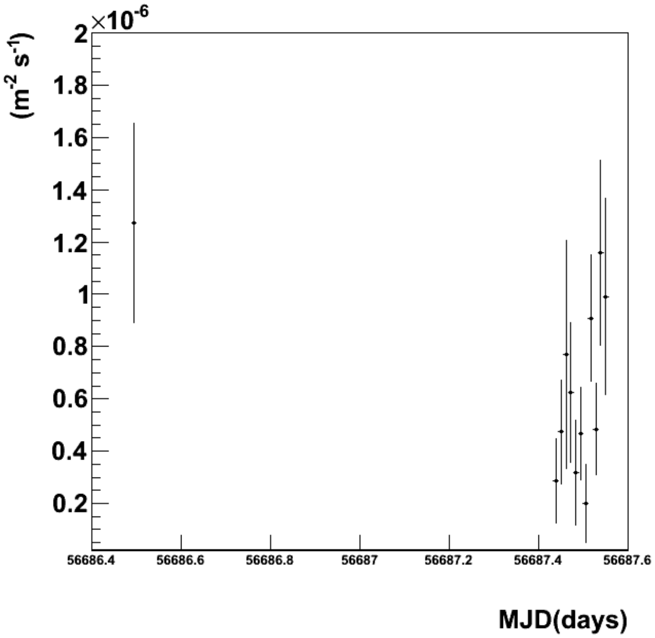

Figure 5.2: VERITAS 16-minute binned light curve with flux above 200 GeV of MS 1221.8+2452 during the flaring episode in 2014.

The VERITAS data analysis is cross checked with a secondary analysis package by a collaborator, Dr. Pat Moriarty from Galway-Mayo Institute of Technology, producing consistent results.

The summary of results from the analysis of VERITAS observations is provided in Table 5.1. The source is detected at a $5\sigma$ or greater significance in all individual runs. A combined analysis produces a detection with $16.5\sigma$ significance.

The averaged VHE gamma-ray spectrum of MS 1221.8+2452 from VERITAS observations obtained on 29 and 30 January, 2014 is shown in Figure 5.1. The spectrum is well fit by a power-law function ($\chi^2$/DOF = 6.2 / 6 DOF), with an index $\Gamma = -3.2 \pm 0.3$ in the 200–900 GeV energy range. The fitting function is normalized at the decorrelated energy

Table 5.2. *Fermi*-LAT detections of MS 1221.8+2452.

| Analysis | Duration | Energy Range | Significance | Flux [$\mathrm{cm}^{-2}\ \mathrm{s}^{-1}$] | Index | Variability |
|---|---|---|---|---|---|---|
| 2FGL | 2 years | 1–100 GeV | 7.7 | $6.3 \pm 1.2 \times 10^{-10}$ | $2.04 \pm 0.19$ | none |
| 1FHL | 3 years | 10–500 GeV | 6.3 | $7.7 \pm 3.1 \times 10^{-11}$ | $1.26 \pm 0.38$ | none |
| 2FHL | 6.7 years | 50–2000 GeV | 9.1 | $3.7 \pm 1.1 \times 10^{-11}$ | $2.33 \pm 0.44$ | none |
| 3FGL | 4 years | 1–100 GeV | 13.4 | $7.0 \pm 0.9 \times 10^{-10}$ | $1.89 \pm 0.09$ | none |
| Flare Analysis | 4 days | 0.1–100 GeV | 6.3 | $2.8 \pm 0.6 \times 10^{-08}$ | $1.12 \pm 0.32$ | some |

of 320 GeV. In addition, Figure 5.1 illustrates the EBL absorption-corrected VERITAS spectrum of the source using the Gilmore et al. (2012) EBL model. The highest energy spectral point is at an EBL optical depth of $\tau \sim 2.4$. The best-fit power-law function to the absorption-corrected spectrum yields a spectral index of $\Gamma_{deab} = -2.1 \pm 0.3$.

The light curve of MS 1221.8+2452 from VERITAS observations in January and February of 2014 is included in Figure 5.2, with the source flux above 200 GeV ranging between 7% and 50% of Crab Nebula flux.

### 5.2.2 *Fermi*-LAT

In addition to the analysis of the VERITAS observations, the *Fermi*-LAT data is analyzed following standard analysis threads and with tools included in ScienceTools-v9r32p5. Pass 8 data and instrument response functions were used. Data contemporaneous with VERITAS and *Swift* observations of the VHE flare were selected, spanning a four-day period from January 29, 2014 through 1 February, 2014.

An unbinned likelihood analysis was applied to events within a 20° region of interest (RoI) centered on the source position, using only *SOURCE* class events that have a zenith angle of less than 100° and energies between 100 MeV and 300 GeV. Sources from *Fermi*-LAT 4-Year Point Source Catalog (3FGL) (Acero et al., 2015) located within 25° from RoI center, a galactic diffuse emission model (*gll_iem_v05.fits*), and an isotropic diffuse emission model (*iso_source_v05.txt*) were used to compose the background model. Normalization and spectral index model parameters for sources within 10° of RoI center and the normalization parameter for the diffuse component models were left free, while spectral parameters were fixed to the 3FGL catalog values for sources further away from

Table 5.3. Summary of *Swift*-XRT observations.

| Exposure Range [MJD] | Observation ID | Exposure [minutes] | Flux (0.3–10 keV) $10^{-11}$ erg cm$^{-2}$ s$^{-1}$ | Index | $\chi^2$/NDF |
|---|---|---|---|---|---|
| 56687.4402–56687.4604 | 000327430**20** | 30.3 | 3.08±0.11 | 2.10±0.05 | 399.0/307 |
| 56687.5111–56687.5701 | 000327430**21** | 29.9 | 3.83±0.13 | 1.95±0.05 | 384.2/327 |
| 56688.4389–56688.4583 | 000327430**22** | 29.8 | 3.98±0.16 | 2.26±0.06 | 324.2/242 |
| 56689.4333–56689.4530 | 000327430**23** | 28.3 | 2.73±0.10 | 2.35±0.06 | 337.9/248 |

RoI center. The background model was fit to the data. Any sources with negative test statistic (TS) value were removed from the model and the fit was repeated.

The optimized background model resulting from the likelihood fit includes a source consistent with the position of MS 1221.8+2452. This source was detected with a significance $\sim 6.6\sigma$ (TS=43.23) and a flux (0.1–300GeV) of $4.8 \pm 3.6 \times 10^{-8}$ cm$^{-2}$ s$^{-1}$. The source is modeled as a power-law function, $\frac{dN}{dE} = N(\frac{E}{E_o})^{-\Gamma}$, where $N$ is the flux normalization and $\Gamma$ is the spectral index with a best-fit value of 1.12±0.33.

MS 1221.8+2452 is also detected and included in the *Fermi*-LAT 2-Year Point Source Catalog (2FGL) (Nolan et al., 2012), 3FGL, the First *Fermi*-LAT Catalog of Sources above 10 GeV (1FHL) (The Fermi-LAT Collaboration, 2013), and the Second Catalog of Hard *Fermi*-LAT Sources (2FHL) (Ackermann et al., 2016a). Table 5.2 lists the detection significance and spectral parameters for MS 1221.8+2452 from 2FGL and 1FHL, as well as results from my dedicated analysis of the source within the 4-day period encompassing the VHE flare. Neither 2FGL nor 1FHL classify MS 1221.8+2452 as a variable source. The detection of the source within a 4-day period around the time of the VHE flare alone, however, suggests MS 1221.8+2452 was in an elevated state, as the significance is comparable to the detection significance in 2FGL and 1FHL, both of which utilize multiyear datasets.

### 5.2.3 *Swift* XRT and UVOT

*Swift* X-ray Telescope (XRT) and Ultraviolet Optical Telescope (UVOT) target-of-opportunity (ToO) observations were triggered for dates between 30 January and 1 February, 2014, resulting in four observations over the course of three days following the VERITAS snapshot of the VHE flare on 29 January. Observations numbered 20 and 21 were taken ~75 minutes apart on 30 January; whereas, observations 22 and 23 were taken a day apart on 31 January and 1 February, respectively.

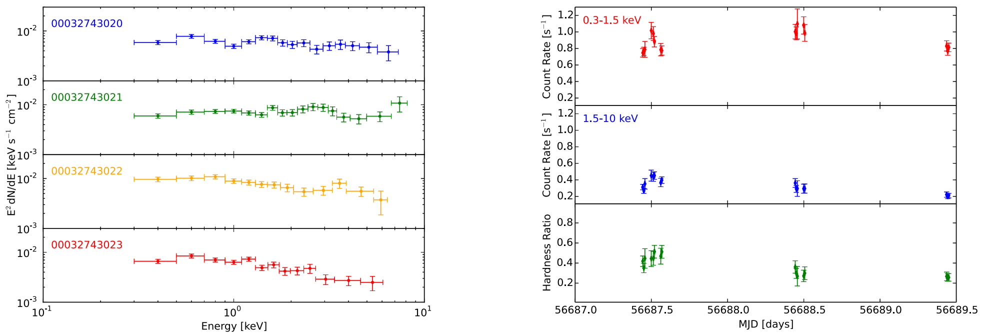

Figure 5.3: (*Left*:) *Swift*-XRT spectra for individual observation, corrected for Galactic neutral Hydrogen absorption. (*Right*:)*Swift*-XRT 5-minute binned soft (0.3-1.5keV), hard (1.5-10keV) X-ray band light curves and hardness ratio, from top to bottom.

The *Swift*-XRT data were analyzed using the standard tools provided in HEASoft package Version 6.15.1. XRT data were analyzed with XRTDAS v3.0.0 tools, with spectral analysis and fitting performed using Xspec v12.8.1g.

All XRT observations of MS 1221.8+2452 were affected by pile-up (registering multiple lower energy photons as a single higher energy photon) due to the high count rate of the source. Pile-up occurs only in the innermost pixels covered by the source. To correct for this effect, the XRT PSF is fit to the outer source pixels. The counts in the inner pixels are then replaced with values from the PSF fit.

XRT flux spectra are obtained by unfolding the counts spectra with instrument response functions included in CALDB 1.0.2, and assuming an absorbed power-law functional form for the intrinsic spectrum. The unfolded XRT spectra are corrected for Galactic absorption by neutral Hydrogen. Neutral Hydrogen column density for the absorber is taken from the LAB survey (Kalberla et al., 2005), with a value $N_H$=1.68×$10^{20}$ cm$^{-2}$. Spectra from individual observations are shown in the left panel of Figure 5.3.

Soft (0.3–1.5 keV) and hard (1.5–10 keV) X-ray band light curves, along with the hardness ratio (hard rate / soft rate) are constructed from the MS 1221.8+2452 XRT observations and included in the right panel of Figure 5.3.

MS 1221.8+2452 was in an elevated state in *Swift*-XRT ToO observations, with fluxes ranging between $5.21 \times 10^{-11}$ erg cm$^{-2}$ s$^{-1}$ and the historically highest flux value of $6.68 \times 10^{-11}$ erg cm$^{-2}$ s$^{-1}$, which the source reached on January 31. Details of XRT observations and analysis results are summarized in Table 5.3.

For analyzing *Swift*-UVOT data, *uvotsource* tool is used to perform aperture photometry on individual bands (UVW1, UVM2, UVW2, U, B, V) and measure the source flux in each exposure. A circular region with $5''$ radius centered on MS 1221.8+2452 coordinates is used for the source region, while a background region is defined within a $15''$-radius circle located in a source-free area near the MS 1221.8+2452 location. Extinction correction is applied with $E(B-V) = 0.0116$ (Schlafly & Finkbeiner, 2011) and extinction coefficients derived for individual bands using the Fitzpatrick (1999) reddening law. The effective wavelength for each band is taken from Breeveld et al. (2011).

MS 1221.8+2452 is not detected in the *Swift*-BAT 70-month catalogue and has not been identified as a *Swift*-BAT transient source (Baumgartner et al., 2013b).

## 5.3 SED Construction and Modeling

Figure 5.4 shows 5-minute bin light curves for VERITAS and *Swift* 30 January, 2014 observations of MS 1221.8+2452. This dataset contains ∼70 minutes of strictly simultaneous data. The simultaneous data are used to construct averaged VERITAS, *Swift*-XRT, *Swift*-UVOT SEDs, which in conjunction with the contemporaneous *Fermi*-LAT spectrum is used to construct the broadband, multi-wavelength SED.

The broadband SED for MS 1221.8+2452 encompassing VERITAS, *Fermi*-LAT, *Swift*-XRT, and *Swift*-UVOT observations around the time of the VHE flare is presented in Figure 5.5.

VERITAS, *Swift*-XRT, and *Swift*-UVOT data are near-simultaneous, whereas the *Fermi*-LAT data is only contemporaneous extending over the 4-day period during which the source was observed with either VERITAS or *Swift*.

The SED modeling is performed by a VERITAS collaborator, Dr. Matteo Cerruti. A stationary, one-zone SSC model is used (Cerruti et al., 2013) The model assumes emission from a spherical blob relativistically propagating in the blazar jet. The blob is parametrized by a radius R, a Doppler factor $\delta$ and homogeneous, tangled, magnetic

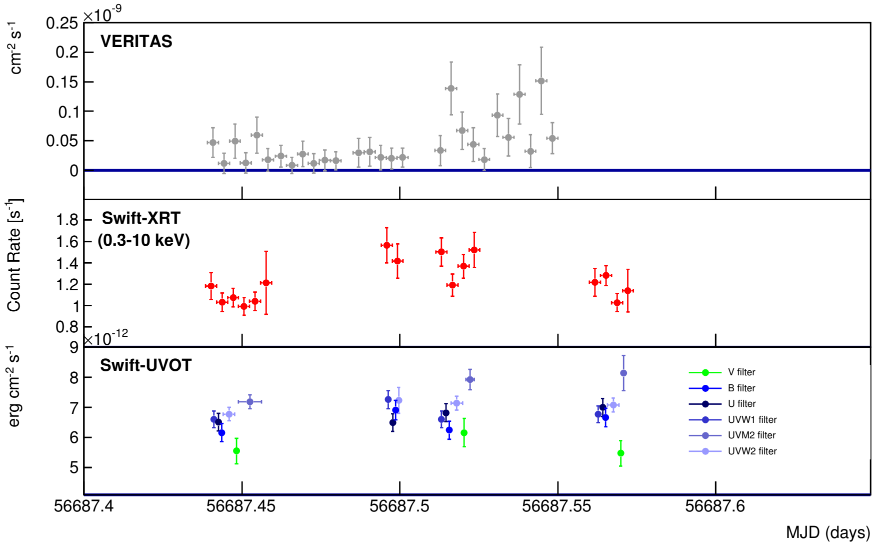

Figure 5.4: VERITAS, *Swift*-XRT, and *Swift*-UVOT contemporaneous light curve in 5-min bins.

fields of strength $B$. The particle population is described by a broken power-law energy distribution with indices $\alpha_1$, $\alpha_2$, the Lorentz factors $\gamma_{min}$, $\gamma_{break}$, $\gamma_{max}$ and a density, $K$.

The observed SED is compatible with a single zone SSC model. The parameters for the SSC model used to characterize the broadband SED are listed in Table 5.4. The MS 1221.8+2452 averaged flare SED is described within standard parameters for HBLs. The blob energetics are somewhat out of equipartition and are particle dominated, with $u_e/u_B = 158$. The predicted minimum variability timescale from the model is 4.7 hours.

This stationary SSC model provides an averaged representation of the flare state. A possible conflict can be seen between the rapid, ~0.5-hours variability observed in VERITAS and the variability timescale from the model. A more complete treatment would require a time-dependent SSC model. Such a model, however, is not likely to be viable for the current dataset due to low gamma-ray statistics.

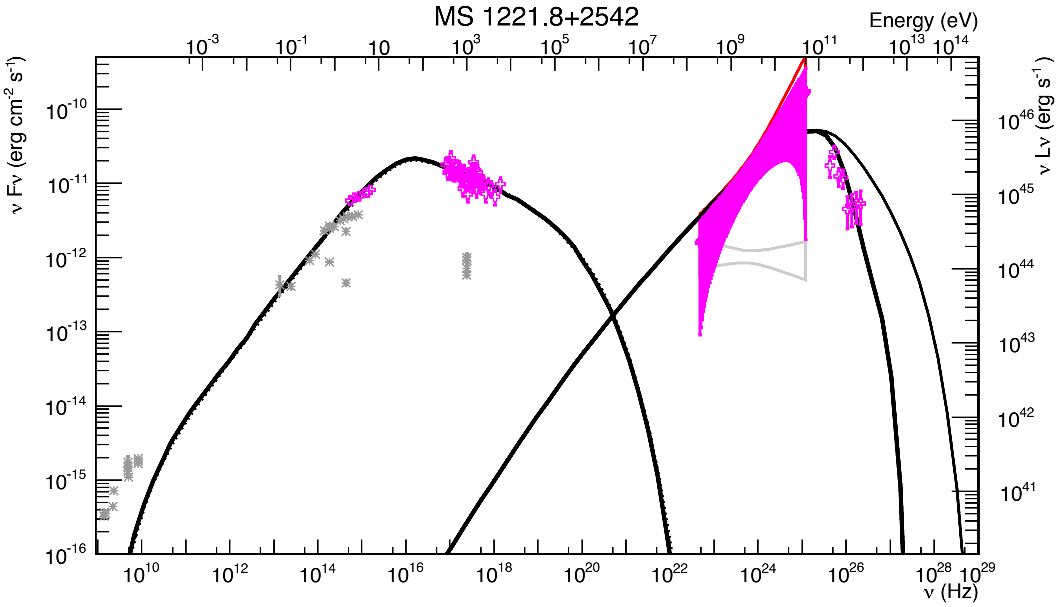

Figure 5.5: Broadband SED of MS 1221.8+2452 with a stationary, one-zone SSC model compatible with the data. The flare SED is shown in pink, while the average state SED from archival data is shown in grey. The higher curve in the VHE gamma-ray regime shows the SED model corrected for EBL absorption with Gilmore et al. (2012) EBL model.

## 5.4 Variability

### 5.4.1 VHE Gamma rays

MS 1221.8+2452 shows significant flux variability in VERITAS observations. A constant flux for the light curve is ruled out at a 99% confidence level based on a fit to a constant line ($\chi^2$/NDF = 26.2/12). In addition, in 30 January, 2014 observations alone, there is a significant increase in flux with time towards the end of the observations, with a flux doubling time of ~30 minutes in the last 90 minutes.

Spectral variability in MS 1221.8+2452 VERITAS observations is also investigated, with spectra reconstructed from individual VERITAS exposures using a forward folding technique (implemented by the author), similar to Albert et al. (2007). The technique is a generalization of the standard spectral reconstruction method described in Section 2.4.8. Unlike the standard spectral reconstruction, however, no thresholding is

Table 5.4. Parameters of the SSC models for the MS 1221.8+2452 broadband SED.

| | GENERAL TRANSFORMATION PARAMETERS | |
|---|---|---|
| 30 | Doppler Factor, $\delta$ | |
| 0.218 | redshift, $z$, | |
| $1.25 \times 10^{16}$ | Radius of emitting region, $R_{src}$ | cm |
| | BLOB PARAMETERS | |
| 100 | Minimum electron energy Lorentz factor, $\gamma_{\min}$ | |
| $4.3 \times 10^{4}$ | Break in electron energy spectrum, $\gamma_{\mathrm{break}}$ | |
| $3 \times 10^{6}$ | Maximum electron energy Lorentz factor, $\gamma_{\max}$ | |
| 1.4 | First slope of particle energy spectrum, $\alpha_{e,1}$ | |
| 3.4 | Second slope of particle energy spectrum, $\alpha_{e,2}$ | |
| 13.8 | Particle density, K$_e$ | cm$^{-3}$ |
| 50 | Magnetic field strength, $B$ | mG |

applied at the lower energies and potential issues related to binning (e.g., cross-talk between bins due to energy resolution) are robustly accounted for. Forward folding is a parameterized solution. It is applied by assuming a spectral shape for the intrinsic source counts spectrum (typically parameterized as a power-law function), convolving this spectrum with the migration matrix (a matrix calculated from simulations, containing the probabilities of detecting photons with a *true* energy at a given *reconstructed* energy), and comparing the resulting spectrum to the observed counts spectrum using a $\chi^2$ fit.

The resulting spectra from the forward folding technique applied to individual VERITAS exposures of MS 1221.8+2452 are displayed in Figure 5.6. The parameter contours from a grid scan across normalization and index parameters of power-law fits to the observed data are presented in Figure 5.7. Unfortunately, the low statistics of the individual spectra prevent any claims of significant spectral variability. This is also the case for standard spectral reconstruction with VEGAS, as illustrated in Figure 5.8, where the best-fit spectral index measured with VEGAS for each VERITAS exposure is plotted as a function of the source flux.

### 5.4.2 X-rays: Spectral Hysteresis

A possible spectral hysteresis is apparent in the *Swift*-XRT MS1221.8+2452 data on daily timescales. The XRT spectral index is plotted against the 0.3-10 keV band flux for the 4 XRT observations in Figure 5.9. Observations 21, 22, and 23 are separated by

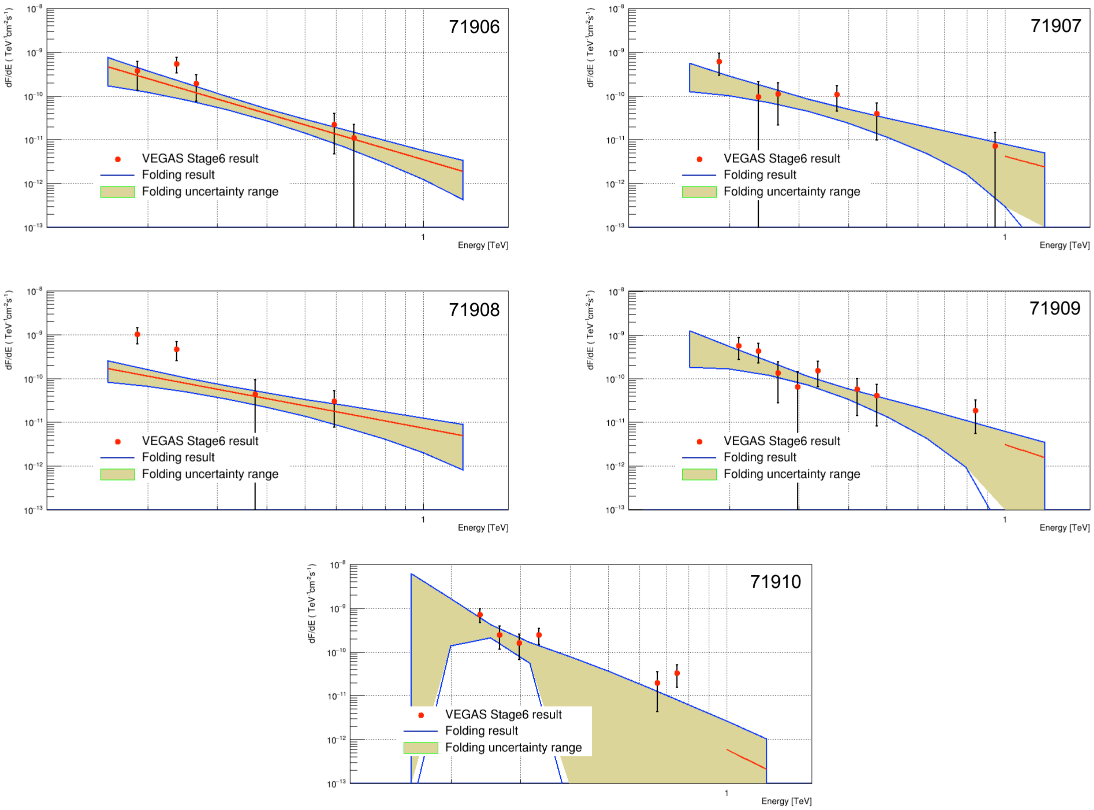

Figure 5.6: VERITAS spectra reconstructed for individual runs with a forward-folding technique are shown in (bands). Red points are the VERITAS spectra from standard analysis with VEGAS.

approximately a day, whereas observations 20 and 21, obtained on 30 January, are only 70 minutes apart. Thus, there is evidence for both intranight variability on 30 January and internight variability. A simple harder-when-brighter trend does not represent the data well, with a $\chi^2/\mathrm{NDF} = 5/2$ for a fit to a straight line, corresponding to a p-value of 0.08.

Spectral hystereses have been observed for a number of blazars in X-rays, including Mrk 421 (Cui, 2004; Abeysekara et al., 2017), Mrk 501 (Catanese & Sambruna, 2000), PKS 2155-304 (Sembay et al., 1993; Kataoka et al., 2000), and H1426+428 (Falcone et al., 2004). Moreover, Nandikotkur et al. (2007) reported detections of spectral hystereses with counter-clockwise directions in gamma-ray data of three FSRQs (PKS

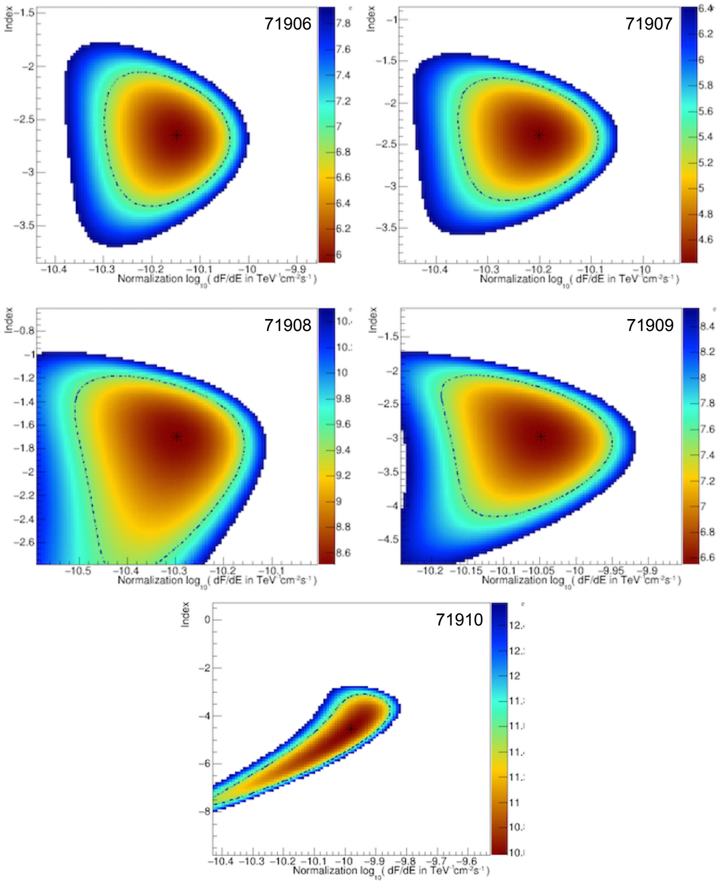

Figure 5.7: Power-law index and normalization parameter scan contours for each VERITAS exposure, with color indicating the $\chi^2$ value associated with the fit to spectral data for each parameter set.

1622−297, PKS 0528+134, PKS 1406−076) from The Energetic Gamma-Ray Experiment Telescope (EGRET).

Theoretical interpretations of X-ray spectral hysteresis observations during blazar flares have been developed by e.g., Kirk et al. (1998) and Böttcher & Chiang (2002). The loop-like pattern of the hysteresis is explained in terms of competing dynamical, acceleration, and radiative cooling timescales, which determine how the effects of an injection of particles propagate to the observed X-ray photons. The hardening (or softening) of the X-ray spectra are described in terms of soft (hard) photons "lagging" behind hard (soft) photons. If the acceleration timescales is much shorter than the cooling

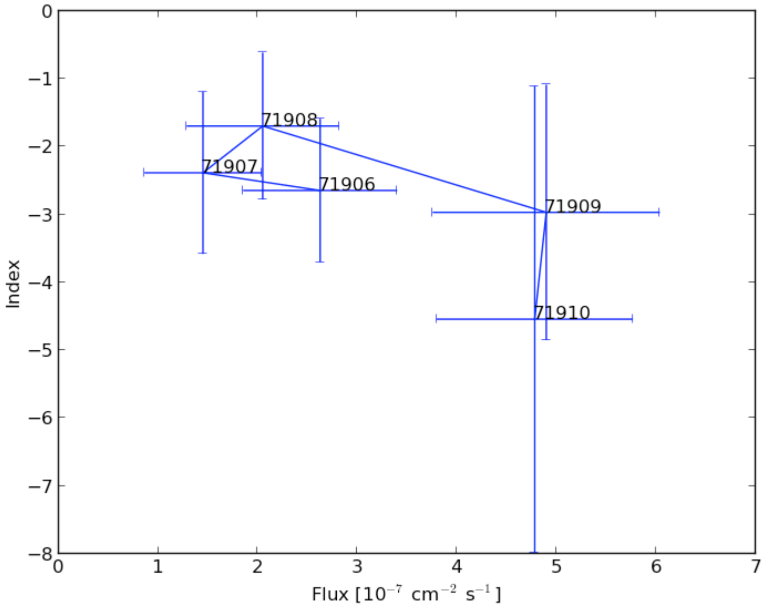

Figure 5.8: Best-fit power-law index vs. flux for spectra from individual VERITAS exposures.

timescale, soft photons will lag behind the hard photons (i.e., flux changes propagate to higher energy photons first). As the source brightens from injection and acceleration of particles into the emission zone, its spectrum will also get harder with higher-energy particles cooling first. With higher energy particles being depleted faster than lower energy particles, the source spectrum will become softer while the flux remains bright and proceeds to decline. Such a scenario produces a clockwise hysteresis. On the other hand, if the dynamical, acceleration, and cooling timescales are comparable, hard photons will lag behind the soft photons as the change in the number of emitting particles is determined by the acceleration process, which proceeds from lower to higher energies. The hysteresis will then follow a counter-clockwise direction.

The relations between dynamical, acceleration, and cooling timescales – and by extension, the direction of the hysteresis loop – are related to the dominant emission mechanism and the total injection power. Within the SSC paradigm (where particles are cooled by either synchrotron or Compton scattering), if observations probe energies below the synchrotron peak/cutoff energy, a clockwise hysteresis direction can be associated with a low injection energy and synchrotron-dominated emission; whereas a

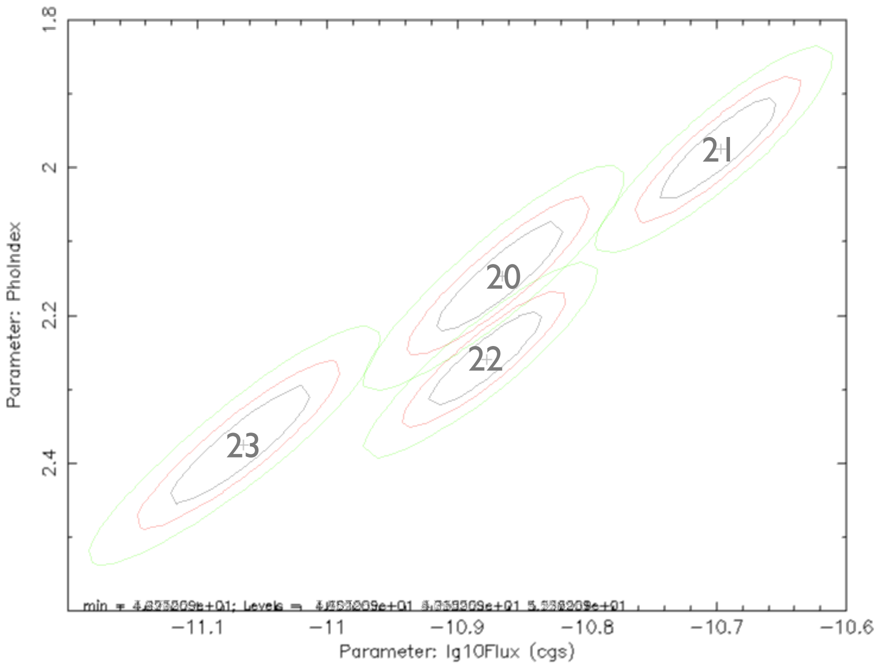

Figure 5.9: *Swift*-XRT spectral index plotted against flux in the full XRT band (0.3-10keV) for individual observations. The contours provide $1\sigma$, $2\sigma$, and $3\sigma$ confidence levels for parameter uncertainties.

counter-clockwise hysteresis is expected for high injection energy and Compton-dominated emission. At observed energies higher than the synchrotron peak, however, the direction of hysteresis can no longer be directly associated with a dominant emission mechanism, as it becomes degenerate with injection energy (Li & Kusunose, 2000).

The spectral hysteresis of MS 1221.8+2452 in XRT observations follows a clockwise direction, suggesting a scenario where the cooling timescale is much longer than the acceleration and dynamical timescales. However, as Figure 5.5 illustrates, the XRT observations appear to be originating at higher energies than the synchrotron peak. Thus, no firm conclusions can be made concerning the dominant cooling mechanism from the hysteresis direction.

### 5.4.3 The X-ray – Gamma-ray Relationship

The relationship between the VHE gamma-ray and X-ray fluxes can give insight into the details of the emission mechanism. For a single-zone SSC model, a roughly quadratic relationship is expected between fluxes from the two bands over the course of a flare, as emission depends on both the density of the electron population and the density of photons produced by the same electron population (Marscher & Gear, 1985). Such a behavior has been observed for Mrk 501 (e.g., Furniss et al., 2015). A linear relationship between VHE gamma-rays and X-rays is also possible during flares. This can occur if the inverse-Compton scattering takes place in the Klein-Nishina regime (e.g., Tavecchio et al., 1998) and the particle density and the strength of the magnetic field drop as a result of adiabatic expansion of the emitting region (Katarzyński et al., 2005).

The VHE gamma-ray and X-rays relationship is explored in Figure 5.10, where VERITAS $>$ 200 GeV flux is plotted against XRT 0.3–10keV count rate. The linear and quadratic fits perform equally well, with respective goodness of fit values $\chi^2$/NDF=12.2/11 and $\chi^2$/NDF=12.9/11. There are no obvious trends, with points exhibiting large amount of scatter in addition to the large uncertainties and no conclusions can be drawn based on this relationship.

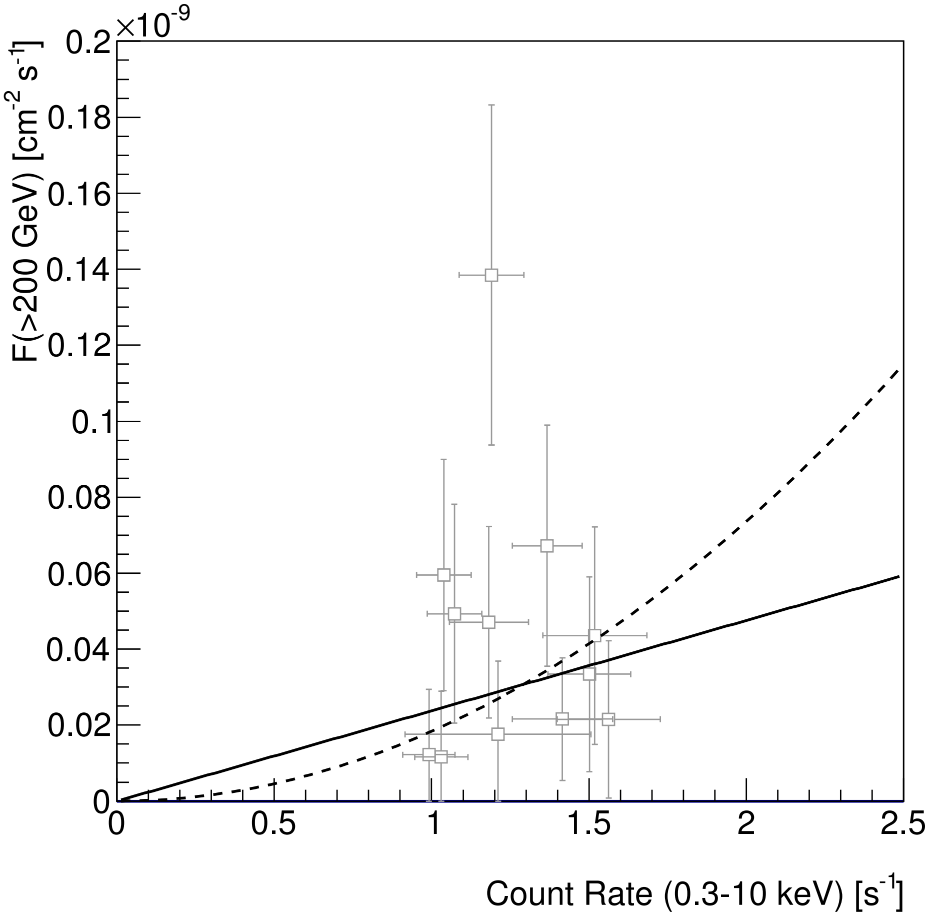

Figure 5.10: VHE gamma-ray flux from VERITAS plotted against X-ray flux from *Swift*-XRT from simultaneous observations. Linear (solid line) and quadratic (dashed curve) fits are shown as well.

# Chapter 6

# PG 1553+113: Periodic Variability

Detections of gamma-ray periodicity in blazars have been made possible only very recently, thanks to the availability of over 9 years of high-quality and high-cadence observations from *Fermi*-LAT. PG 1553+113 was one of the first blazars with confirmed quasi-periodic gamma-ray flux modulation at a 99% confidence level with a period of $2.18 \pm 0.08$ years (Ackermann et al., 2015). The same study found evidence for periodicity from this source in both optical and radio bands, with periods of $2.06 \pm 0.05$ years and $1.9 \pm 0.1$ years, respectively. Two other blazars have detections of periodicity in *Fermi*-LAT: PKS 2155−304 with a period of 1.7 years (Sandrinelli et al., 2014; Zhang et al., 2017) and BL Lac with a period of 1.9 years (Sandrinelli et al., 2017). A number of other blazars have recently been identified as candidates for periodic emission after an all-sky search within the *Fermi*-LAT data: 4C +01.28, S5 0716+71, PKS 0805-07, and PKS 2052−47 (Prokhorov & Moraghan, 2017).

The detection of periodic behavior of PG 1553+113 in gamma rays by *Fermi*-LAT led to a multi-wavelength observing campaign, including VERITAS over the 2016-2017 season. This corresponded to the time around the maximum brightness of the source predicted by *Fermi*-LAT. In addition, PG 1553+113 has been extensively observed with VERITAS since 2010, as one of the Blazar Science Working Group's long-term plan sources. A VERITAS publication concerning PG 1553+113 reported results from

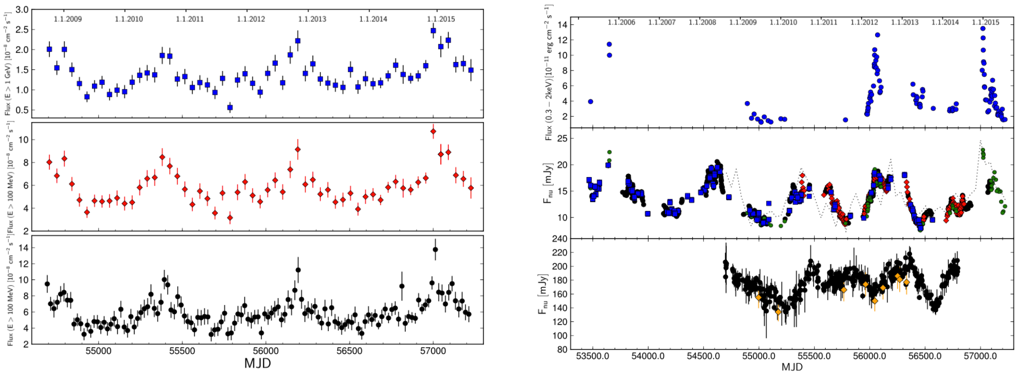

Figure 6.1: **(From Ackermann et al. (2015).)** *Left*: *Fermi*-LAT light curves of PG 1553+113 from. *Right*: Long-term multi-wavelength light curves.

observations between 2010 and 2012, along with an upper limit on the source redshift of $z < 0.62$ (Aliu et al., 2015). A robust lower limit on the redshift, $z > 0.4$ has been placed by Danforth et al. (2010) using Lyman alpha forest observations, with an estimate for the redshift, $z \sim 0.49$ based on EBL absorption derived by Abramowski et al. (2015).

This chapter analyzes over 8 years of VERITAS observations of PG 1553+113. The primary goal of this work is to construct the VERITAS light curve of PG 1553+113 to be included in a multi-collaboration publication – led by the MAGIC Collaboration – to search for periodic flux modulations in VHE gamma-ray, X-ray, and radio observations of this source. The periodicity searches performed on VERITAS data in this chapter are exploratory in nature, with a goal of spotting obvious signs of periodicity. More robust investigation is left for the eventual publication.

## 6.1 Periodic Variability and Blazar Emission Mechanisms

Observations of periodic or quasi-periodic behavior in the non-thermal emission of blazars is exciting as it can provide insights about the physical characteristics of the emission region. There are only a handful of viable scenarios for explaining periodicity in gamma rays, as any proposed mechanism needs to be tied to the non-thermal emission from the jet (Ackermann et al., 2015). The periodicity could be caused by (1) jet geometry (precession, rotation, or helical structure), (2) periodic changes in the accretion flow, or (3) presence of a supermassive black hole binary.

A precession or rotation of the blazar jet or a helical jet structure can periodically change the level of alignment (or viewing angle) of the relativistic outflow with respect to our line of sight, modulating the Doppler factor and the associated boosting and beaming effects (e.g., Ostorero et al., 2004; Rieger, 2004). A helical jet model has already been suggested for the PG 1553+113 emission, as an explanation for peculiarities in the synchrotron portion of its SED (Raiteri et al., 2015).

Periodic accretion flow instabilities, such as pulsational flow instability could be another explanation of the observed gamma-ray periodicity from PG 1553+113. Pulsational instability in an accretion disk can develop as a result of a rapid increase in viscosity with increase in density and temperature (Kato, 1979). With an efficient mechanism for transferring energy from the accretion disk to the jet, a pulsational flow instability can generate periodic changes in the gamma-ray brightness. A strong coupling between the inner accretion disk and the jet is expected in magnetically-dominated accretion flows, which can occur in radiatively inefficient accretion disks of blazars (e.g., Fragile & Meier, 2009). The HBL class of blazars, of which PG 1553+113 is a member are characterized by such radiatively inefficient accretion disks.

A third possibility is the presence of a close, milliparsec-separated SMBH binary. A SMBH binary can periodically perturb the accretion disk, inject blobs of plasma into the jet, cause jet precession, and modulate the viewing angle through the orbital motion of the jet (Rieger, 2007). A potentially discriminatory property of a close SMBH binary is that the observed periods are expected to be different for different energy bands, as the physical cause of the periodicity in different bands could be distinct. An argument against this case for PG 1553+113, however, is the small probability of observing a close binary pair with an orbital period of $\sim 1.5$ years required to explain a 2.18-year periodicity (Ackermann et al., 2015).

## 6.2 Search for Periodicity in VERITAS Observations of PG 1553+113

To date, there are no definitive detections of periodic or quasi-periodic modulations from AGN in VHE gamma rays. With the detection of quasi-periodic modulations by Ackermann et al. (2015), PG 1553+113 has become the most promising candidate, largely due to its brightness, for exhibiting a similar behavior in VHE gamma rays.

VERITAS observations of PG 1553+113 can potentially discriminate between scenarios responsible for the detected periodicity in *Fermi*-LAT, optical, and radio bands with or without a detection of periodic behavior. A detection of periodicity in VERITAS, however, and potential correlations with the other available bands would be a key piece of evidence for differentiating between geometric scenarios in which the Doppler factor is modulated due to the level of alignment of the jet with our line of sight and with scenarios requiring periodic changes to the energetic particle populations responsible for the jet emission.

A more robust investigation (beyond the scope of this chapter) will use the VHE spectra of PG 1553+113 to construct time-resolved multi-wavelength SEDs of the source. Models of the SEDs and exploration of their parameters, including Doppler factor and particle population parameters (e.g., emission region size, density, energy distribution) can then be used to test if periodic changes in the Doppler factor or alignment angle are sufficient or if changes to the properties of the particle populations (tied to details of the accretion flow) are necessary.

### 6.2.1 Observations

VERITAS has observed PG 1553+113 between 2010 and 2017. These observations span two major VERITAS hardware setups (New Array and Upgraded Array), with the camera upgrade in the Summer, 2012 dividing the dataset. Weather and data quality are assessed for all observations, removing poor quality data from the analysis. The remaining observations include over 120 hours of quality-cleaned livetime on PG 1553+113.

### 6.2.2 Data Analysis

PG 1553+113 VERITAS data are analyzed with the standard package, `VEGAS`. In VHE gamma rays, this source is known to have a very soft spectrum, with $\Gamma \sim 4$. VEGAS selection criteria optimized for soft sources, known as *soft cuts* are used. The criteria are listed in Table 6.1. The two values for the *image size* listed in the table provide the criteria separately for the New Array (NA) and the Upgraded Array (UA) data.

Table 6.1. Data selection criteria for analyzing PG 1553+113 observations.

| Criterion | Soft Cuts<br>NA \| UA | Standard Cuts<br>NA \| UA |
|---|---|---|
| Distance [degrees] | $< 1.43$ | $< 1.43$ |
| Size [digital counts] | $> 200 \mid > 400$ | $> 400 \mid > 700$ |
| Number of Pixels in Image | $> 5$ | $> 5$ |
| Mean Scaled Width | 0.05 – 1.10 | 0.05 – 1.10 |
| Mean Scaled Length | 0.05 – 1.30 | 0.05 – 1.30 |
| Shower Maximum Height [km] | 7 | 7 |
| $\theta^2$ [degrees$^2$] | 0.03 | 0.01 |

The primary difference from selection criteria for a standard analysis are (1) a lower minimum image size, preferentially allowing more faint and lower energy showers and (2) a larger $\theta^2$ (distance from field of view center) for associating events with a source, necessary to accommodate the higher uncertainty in the direction reconstruction from using fainter showers.

A common issue for a *soft cuts* analysis of VERITAS data is a non-negligible contamination of the background from stars within the field of view. For this reason, circular regions with 0.3° radii around bright stars (>8th magnitude) are excluded from the background estimation.

PG 1553+113 is a fairly bright source for VERITAS with an average of ∼7% of the Crab Nebula flux above 200 GeV (Aliu et al., 2015). At this flux state, it can be detected with $5\sigma$ significance in ∼50 minutes. For the purpose of investigating changes in the PG 1553+113 VERITAS spectrum, the dataset is separated by individual years or seasons of observation. The year-by-year analysis results are provided in Table 6.2. The source is detected with at least $15\sigma$ significance for each year of observation, allowing construction of high-quality spectra. The spectra from individual years are displayed in Figure 6.2, with best-fit spectral indices also listed in Table 6.2. There is no significant evidence for spectral variability.

### 6.2.3 Standard and Phase-Folded Light Curves

Light curves from VERITAS observations are constructed with the standard procedure in `VEGAS`, using the `vaMoonShine` tool. Spectral reconstruction is performed within

Table 6.2. Summary of results from VERITAS observations of PG 1553+113 between 2010 and 2017.

| Year | Livetime [minutes] | On Counts | Off Counts | $\alpha^{a}$ | $\sigma$ | $\Gamma$ |
|---|---|---|---|---|---|---|
| 2010 | 1890 | 11113 | 34870 | 0.17 – 0.50 | 28.5 | $3.7 \pm 0.12$ |
| 2011 | 2642 | 14122 | 44225 | 0.17 – 0.50 | 34.2 | $4.0 \pm 0.10$ |
| 2012 | 1229 | 6377 | 16079 | 0.17 – 0.50 | 36.8 | $4.0 \pm 0.10$ |
| 2013 | 291 | 1239 | 2653 | 0.17 – 0.50 | 16.5 | $3.5 \pm 0.24$ |
| 2014 | 504 | 1852 | 4692 | 0.17 – 0.50 | 18.4 | $3.8 \pm 0.23$ |
| 2015 | 524 | 1617 | 3850 | 0.17 – 0.50 | 17.7 | $4.1 \pm 0.20$ |
| 2016 | 368 | 1043 | 3697 | 0.14 – 0.17 | 15.6 | $3.8 \pm 0.23$ |
| 2017 | 957 | 3267 | 12206 | 0.14 – 0.17 | 24.7 | $3.7 \pm 0.14$ |

[a] Off region-source normalization.

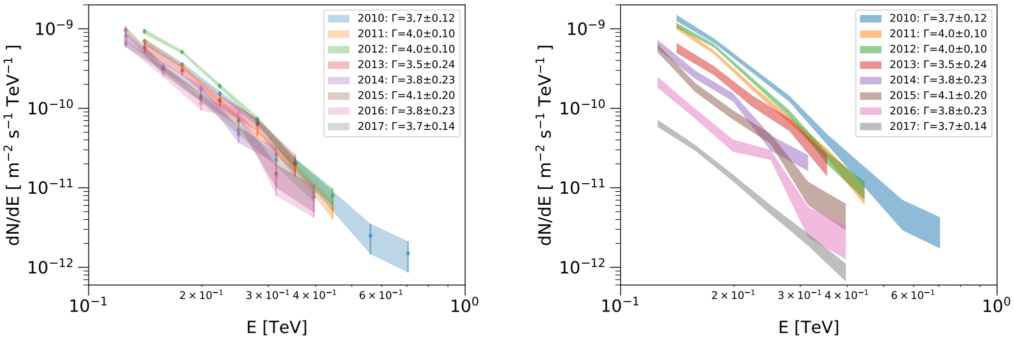

Figure 6.2: *Left*: VERITAS yearly-averaged spectra of PG 1553+113. *Right*: Same spectra, but artificially shifted for better visibility.

individual time bins and the resulting differential spectra are integrated above a specified threshold energy to calculate flux. For the 2017 multi-wavelength campaign on PG 1553+113, a daily-binned VERITAS light curve of the source is produced and compared with *Fermi*-LAT and *Swift*-XRT (Figure 6.3).

The *Swift*-XRT light curve of PG 1553+113 is borrowed from the *Swift*-XRT source monitoring website[1] maintained by Penn State University (Stroh & Falcone, 2013).

The *Fermi*-LAT light curve of the source is generated using the standard Fermi Science Tools[2] version *v10r0p5* and the P8R2_SOURCE_V6 instrument response functions.

---

[1] http://www.swift.psu.edu/monitoring/source.php?source=PG1553+113

[2] https://fermi.gsfc.nasa.gov/ssc/data/analysis

The light curve generation process is automated with the assistance of the `Fermipy` package. *PASS8 Fermi*-LAT data spanning the entire period of VERITAS and *Swift* observations are selected. The region of interest (RoI) is defined with a 20° radius, centered on the catalog position of PG 1553+113. *SOURCE* class events with energies in the 0.1 – 300 GeV range are selected, with events falling at zenith angles $> 100°$ and rocking angles $> 52°$ excluded to avoid contamination from the Earth limb. Unbinned likelihood analysis of the RoI is performed for each daily bin, with the spectral parameters of PG 1553+113 source model fixed to parameters from the 3FGL catalog (Acero et al., 2015) and with a fixed background model of the RoI derived from a likelihood analysis of the entire time period.

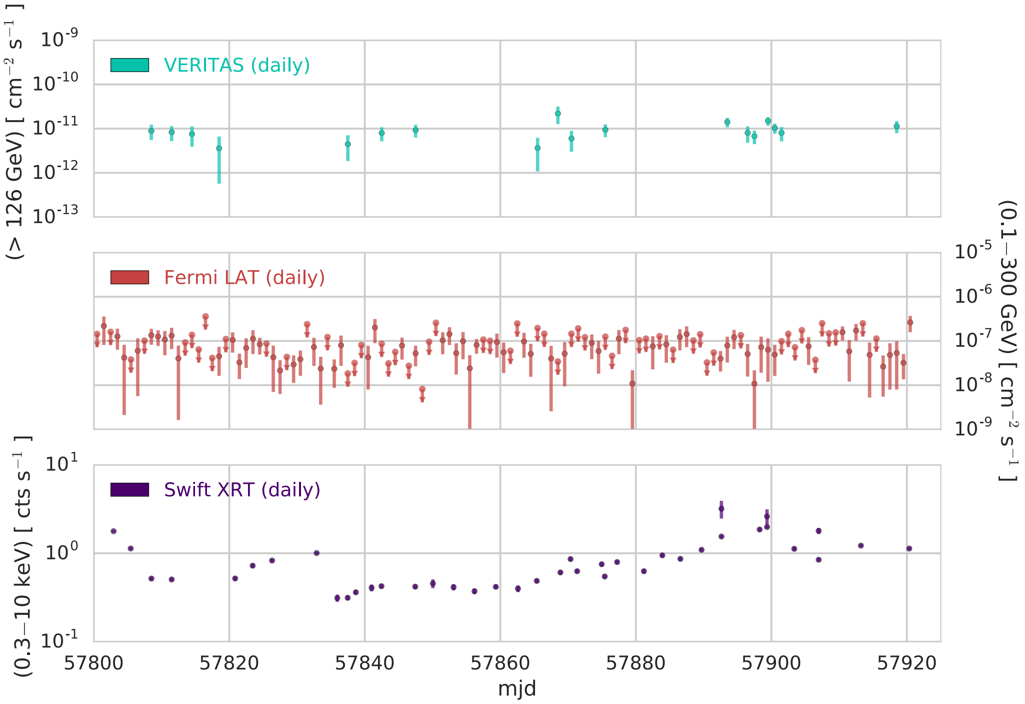

Figure 6.3: Daily light curves of PG 1553+113 from VERITAS (*top*), *Fermi* LAT (*middle*), and *Swift* XRT (*bottom*) during the 2016-2017 observing season multi-wavelength campaign.

No major flaring activity is present in the VERITAS and *Fermi*-LAT gamma-ray light curves; however, *Swift*-XRT shows substantial activity between MJD 57895 and

MJD 57900. In response, VERITAS increased its cadence of observations; however, no major increase in the VHE gamma-ray flux was observed.

A weekly-binned VERITAS light curve of PG 1553+113 for 2010–2017 observations is produced and included in Figure 6.4. This full light curve is used to search for periodicity. The light curve shows PG 1553+113 has a clearly variable flux in VERITAS observations, with $\chi^2/\text{NDF} = 282/73$ and a corresponding p-value for a constant flux of $2.5 \times 10^{-26}$.

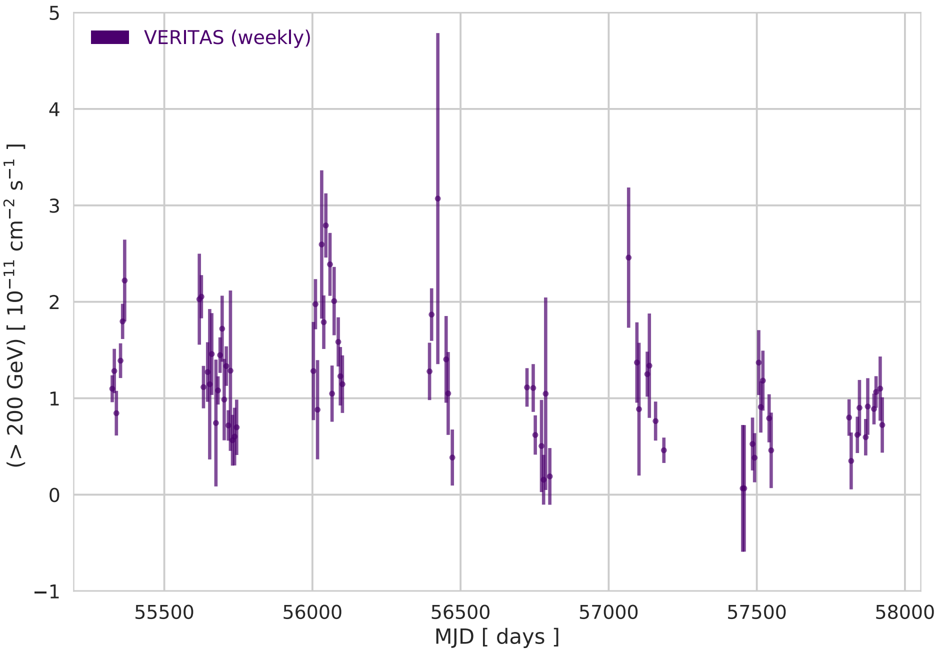

Figure 6.4: Weekly VERITAS light curve of PG 1553+113 for all observations from 2010 through 2017.

A phase-folded VERITAS light curve of PG 1553+113 is generated with the *Fermi*-LAT timing solution to search for the periodicity signatures detected in *Fermi*-LAT and optical observations. A period of 2.18 years is used for folding the VERITAS weekly light curve. The light curve is folded with reference to MJD 55400, where the *Fermi*-LAT light curves exhibit a peak. Thus, by construction, peaks are expected at phases of 0 and 1 in the folded VERITAS light curve, if a periodicity similar to *Fermi*-LAT is significant in the VERITAS data. The resulting folded light curve is displayed in Figure 6.5. A fit of a sinusoidal function with a period fixed to 2.18 years to the folded light curve is not preferred to a constant fit, indicating that there is no significant evidence of the *Fermi*-LAT-detected periodicity in the phase-folded VERITAS light curve.

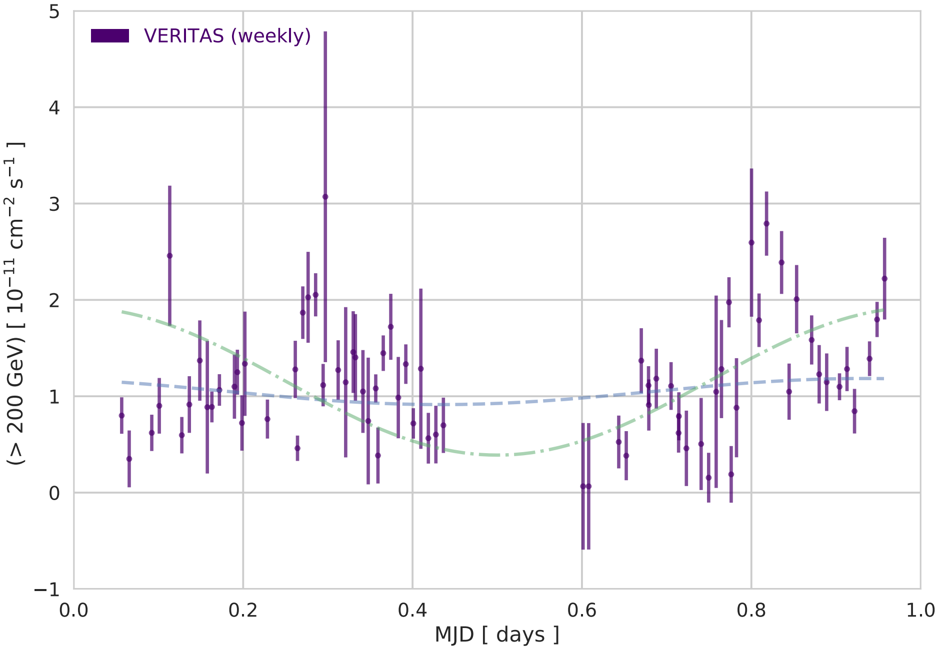

Figure 6.5: Phase-folded VERITAS light curve of PG 1553+113, using the *Fermi*-LAT timing solution. The dashed blue line shows a $\chi^2$ fit of a sinusoidal function, with a period fixed to 2.18 years – the period used for folding – and a fitted amplitude. The dash-dotted line shows a sinusoidal function with both the period and amplitude fixed to the *Fermi*-LAT solution.

### 6.2.4 Lomb-Scargle Periodogram

The VERITAS weekly light curve contains large gaps, making searches for periodicity rather difficult. There are existing time-series analysis techniques, however, that can overcome this difficulty. The Lomb-Scargle Periodogram (LSP) (Lomb, 1976; Scargle, 1982) is a widely used tool for detecting periodicity in unevenly-sampled time-series data, e.g., light curves with large gaps. Here, we apply the LSP to the VERITAS weekly-binned PG 1553+113 light curve to look for periodic flux modulations.

A `python` implementation of the LSP distributed along with the `AstroPy` package[3] is used to investigate periodicity in the VERITAS light curve of PG 1553+113.

The frequency grid for evaluating the LSP is determined following the prescription in (VanderPlas, 2017). The minimum frequency is determined by half of the total duration of the light curve ($[4 \text{ years}]^{-1}$), while the maximum frequency is constrained by the weekly binning ($[2 \text{ weeks}]^{-1}$). Since the computation time for a single light curve is very small, an overly fine sampling grid is chosen, with 100,000 evaluations of the LSP, to avoid missing any fine structure.

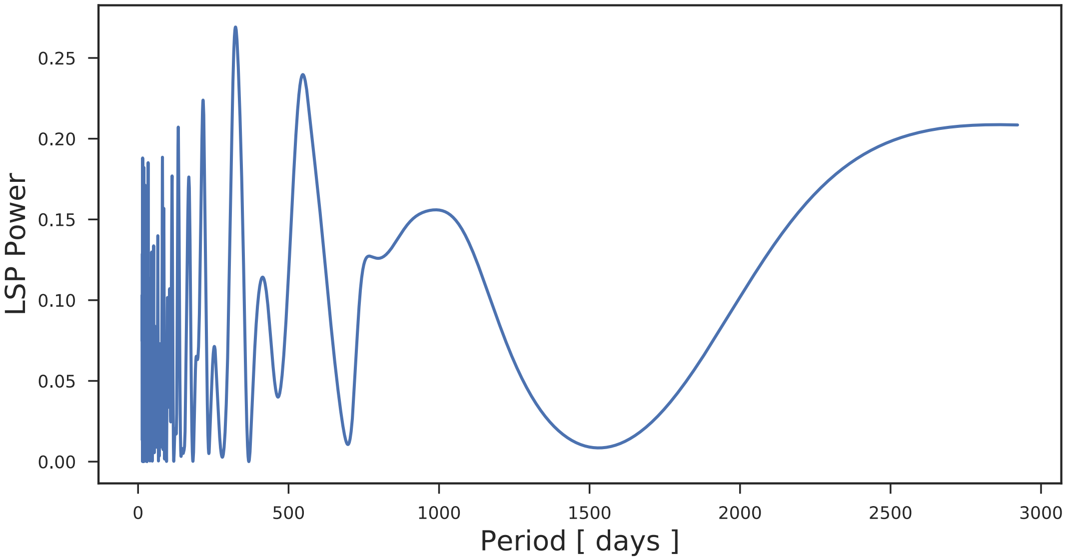

Figure 6.6: The Lomb-Scargle periodogram for the weekly VERITAS light curve of PG 1553+113.

The resulting periodogram is shown in Figure 6.6. There are no obvious peaks that can suggest periodic variations in the PG 1553+113 flux, including on ∼2-year timescales found in *Fermi*-LAT, optical, and radio observations. Note that this is not a rigorous assessment of significance of LSP peaks, which would require, e.g., a Monte Carlo study. The lack of obvious peaks, however, did not warrant such a study for the

---

[3] http://docs.astropy.org/en/stable/stats/lombscargle.html

exploratory analysis performed in this chapter.

### 6.2.5 Power Spectral Density

The weekly VERITAS light curve of PG 1553+113 is used to construct a PSD. No detrending beyond a simple mean-subtraction is applied to the light curve. The resulting PSD is displayed in Figure 6.7, along with the *Fermi*-LAT PG 1553+113 PSD from Ackermann et al. (2015) for comparison. Unlike the *Fermi*-LAT PSD that shows a clear features at $\sim$ 2-year timescale, no strong peaks appear in the VERITAS PSD of PG 1553+113 to indicate the presence of a periodic signal.

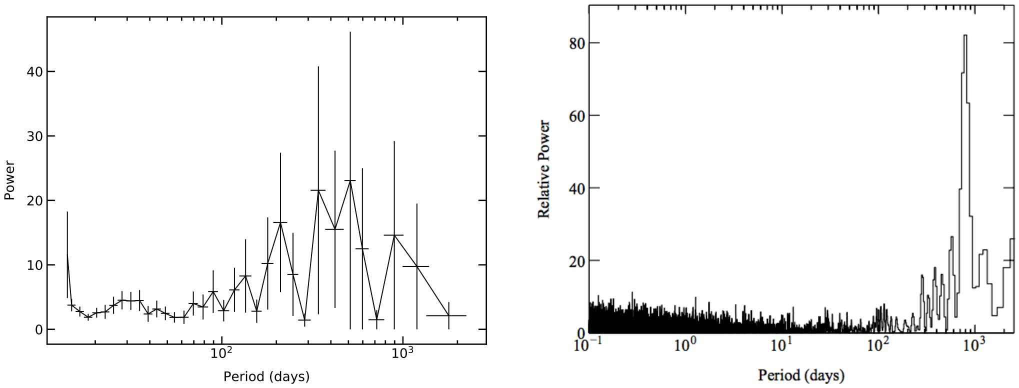

Figure 6.7: *Left*: PSD constructed from PG 1553+113 weekly VERITAS light curve.*Right*: PSD from 7 years of *Fermi*-LAT observations of PG 1553+113 from Ackermann et al. (2015).

### 6.2.6 Discussion and Outlook

There is no significant evidence of periodicity in the 8 years of VERITAS observations of PG 1553+113 using any of the tests performed in this chapter. This is not surprising, however, as it took 7 years of continuous monitoring of the source with *Fermi*-LAT to obtain a marginal detection of quasi-periodic modulations. Despite spanning a slightly longer time period than *Fermi*-LAT, the VERITAS observations of PG 1553+113 are sparse in comparison.

If, however, periodicity in VHE gamma rays can be confidently rejected (with e.g., more data and more sensitive analyses), then it would be difficult to invoke geometric scenarios that simply modulate the Doppler factor to explain the observed periodicity. Simple Doppler factor modulations should result in a VHE gamma-ray behavior similar to the periodicity in GeV and optical bands. These scenarios could still be made viable in models that represent the persistent emission from the source with multiple emission regions. Such models are likely to be severely underconstrained, however.

In the absence of VHE gamma-ray periodicity detection, as previously noted, a time-resolved modeling study of the multi-year PG 1553+113 SEDs is the most promising approach for discriminating between potential emission scenarios and for understanding the mechanism responsible for the observed periodic behavior of this source.

# Chapter 7

# Summary

In this thesis, emission properties of blazars with an array of variability patterns are explored through their VHE gamma-ray and multi-wavelength emissions.

The blazar nature of HESS 1943+213, an unusually stable source, is established with support from results presented here. The detection of a jet-like structure with multi-epoch observations in VLBA 1.6 GHz, 4.3 GHz, and 7.6 GHz bands and the measurements of spectral indices comparable to other known blazars for both the radio core and the jet are strong evidence in support of this position. In addition, the lack of detectable proper motion between EVN and VLBA observations and the two epochs of VLBA observations set constraining upper limits on the transverse velocity as low as 8 km/s if the source is of Galactic origin, essentially ruling out this possibility. The VERITAS and the *Fermi*-LAT spectra together give an accurate description of the $\gamma$-ray peak of the source SED. These spectra are used to derive more stringent upper limits on the source redshift of $z < 0.23$.

No statistically significant evidence of flux or spectral variability is found in data from long-term VERITAS observations, as well as in *Swift*-XRT observations over the course of 4 days.

The improved gamma-ray data are used to update and model the broadband SED of HESS J1943+213. An SSC model with a component for the infrared-to-optical light from the host galaxy describes the SED very well, while keeping model parameters to standard values for HBLs. The VLBA data can also be accommodated in the model with the addition of a stratified, conical jet component. Since EHBLs are candidates for hadronic emission, a possible contribution to the gamma-ray portion of the SED from secondary photons produced along the line-of-sight by UHECR-induced cascades is explored for a range of allowed distances for the source. The shape of the secondary gamma-ray spectra, however, makes them viable only for >1 TeV energies and only if the source is located closer than z $\sim$ 0.14.

A similar investigation is performed for the gamma-ray emission of blazar, PKS 1424+240. In this case, however, a self-consistent model with primary and secondary gamma-ray emission mechanisms is developed. The secondary gamma-rays from cosmic-ray interactions are found to be dominant for the highest-energy VERITAS emission and may account for the hardening of the source; however, they have little allowed contribution at energies below 300 GeV compared to the primary gamma-rays.

The VERITAS observations of the giant flare of Mrk 421 in February, 2010 are analyzed, producing a spectrum that extends up to tens of TeVs and a light curve that can sample the source flux on 2-minute timescales.

Timing analyses are applied to the flare data. The VERITAS and optical PSDs constructed from the flare light curves are consistent with flicker or pink noise. A modified autocorrelation technique is applied to the VERITAS timing data to explore variability on sub-minute timescale. The discrete cross-correlation technique applied to the VERITAS and optical light curves finds significant lags of 30–70 minutes, with gamma rays leading the optical. The short lag timescales might imply cospatial gamma-ray and optical emissions.

The flare of a blazar, MS 1221.8+2452 made the first strong detection of this source in VHE gamma-rays possible with VERITAS. In addition to the construction of the first VHE gamma-ray spectrum of the source, multi-wavelength data is used to assemble and model the flare-time SED of MS 1221.8+2452 with a single-zone SSC model. Moreover, the variability of the source in X-rays is investigated in detail, finding evidence for a spectral hysteresis. The clockwise direction of the hysteresis implies an emission region with a much longer cooling timescale compared to the acceleration and dynamical timescales. The source SED, however, places the X-ray emission at energies higher than the synchrotron peak, where the direction of the hysteresis cannot pinpoint a dominant emission mechanism due to a degeneracy with the total injection energy.

Finally, a search for periodic modulations is performed for the long-term VERITAS dataset of blazar, PG 1553+113, which has exhibited periodic behaviors in the *Fermi*-LAT, optical, and radio bands. This involves the construction of an 8-year VERITAS light curve of the source and application of periodicity search techniques, including the Lomb-Scargle periodogram and the PSD. No periodicity is found in the VERITAS data, which is not surprising given the strength of the signal in *Fermi*-LAT and the lower-statistics VERITAS dataset.

# References

Abdo, A. A., Ackermann, M., Ajello, M., et al. 2010, ApJ, 722, 520

Abeysekara, A. U., Archambault, S., Archer, A., et al. 2015, ApJ, 815, L22

—. 2017, ApJ, 834, 2

Abramowski, A., Acero, F., Aharonian, F., et al. 2011, A&A, 529, A49

Abramowski, A., Aharonian, F., Ait Benkhali, F., et al. 2015, ApJ, 802, 65

Acciari, V. A., Beilicke, M., Blaylock, G., et al. 2008, ApJ, 679, 1427

Acciari, V. A., Aliu, E., Arlen, T., et al. 2010, ApJ, 708, L100

Acciari, V. A., Arlen, T., Aune, T., et al. 2014, Astroparticle Physics, 54, 1

Acero, F., Ackermann, M., Ajello, M., et al. 2015, ApJS, 218, 23

Ackermann, M., Ajello, M., Albert, A., et al. 2015, ApJ, 813, L41

Ackermann, M., Ajello, M., Atwood, W. B., et al. 2016a, ApJS, 222, 5

Ackermann, M., Anantua, R., Asano, K., et al. 2016b, ApJ, 824, L20

Aharonian, F., Akhperjanian, A. G., Anton, G., et al. 2009, A&A, 502, 749

Ahn, C. P., Alexandroff, R., Allende Prieto, C., et al. 2014, ApJS, 211, 17

Ahnen, M. L., Ansoldi, S., Antonelli, L. A., et al. 2015, ApJ, 815, L23

—. 2016, A&A, 595, A98

Akiyama, K., Stawarz, Ł., Tanaka, Y. T., et al. 2016, ArXiv e-prints, arXiv:1603.00877

Albert, J., Aliu, E., Anderhub, H., et al. 2007, Nuclear Instruments and Methods in Physics Research A, 583, 494

Aleksić, J., Anderhub, H., Antonelli, L. A., et al. 2010, A&A, 515, A76

Aleksić, J., Antonelli, L. A., Antoranz, P., et al. 2011, ApJ, 730, L8

Aleksić, J., Ansoldi, S., Antonelli, L. A., et al. 2015, A&A, 578, A22

—. 2016, Astroparticle Physics, 72, 76

Aliu, E., Archer, A., Aune, T., et al. 2015, ApJ, 799, 7

Alves Batista, R., Dundovic, A., Erdmann, M., et al. 2016, JCAP, 5, 038

Amy Furniss for the VERITAS Collaboration. 2015, ArXiv e-prints, arXiv:1502.03012

Antonucci, R. 1993, ARA&A, 31, 473

Archambault, S., Aune, T., Behera, B., et al. 2014, ApJ, 785, L16

Armengaud, E., Sigl, G., Beau, T., & Miniati, F. 2007, Astroparticle Physics, 28, 463

Arnaud, K. A. 1996, in Astronomical Society of the Pacific Conference Series, Vol. 101, Astronomical Data Analysis Software and Systems V, ed. G. H. Jacoby & J. Barnes, 17

Atkins, R., Benbow, W., Berley, D., et al. 2003, ApJ, 595, 803

Atwood, W. B., Abdo, A. A., Ackermann, M., et al. 2009, ApJ, 697, 1071

Auger, P., Ehrenfest, P., Maze, R., Daudin, J., & Fréon, R. A. 1939, Rev. Mod. Phys., 11, 288

Bagchi, J., Vivek, M., Vikram, V., et al. 2014, ApJ, 788, 174

Bartlett, M. S. 1950, Biometrika, 37, 1

Baumgartner, W. H., Tueller, J., Markwardt, C. B., et al. 2013a, ApJS, 207, 19

—. 2013b, ApJS, 207, 19

Begelman, M. C., Fabian, A. C., & Rees, M. J. 2008, MNRAS, 384, L19

Biteau, J., & Williams, D. A. 2015, ApJ, 812, 60

Blackett, P. 1948, Physical Society, 34

Blandford, R. D., & Payne, D. G. 1982, MNRAS, 199, 883

Blandford, R. D., & Rees, M. J. 1978, Phys. Scr, 17, 265

Blandford, R. D., & Znajek, R. L. 1977, MNRAS, 179, 433

Boettcher, M. 2012, ArXiv e-prints, arXiv:1205.0539

Boettcher, M., Harris, D., & Krawczynski, H. 2012, Relativistic Jets from Active Galactic Nuclei (Wiley)

Bonnoli, G., Tavecchio, F., Ghisellini, G., & Sbarrato, T. 2015, MNRAS, 451, 611

Borione, A., Covault, C. E., Cronin, J. W., et al. 1994, Nuclear Instruments and Methods in Physics Research A, 346, 329

Böttcher, M. 2005, ApJ, 621, 176

—. 2007, Ap&SS, 309, 95

Böttcher, M., & Chiang, J. 2002, ApJ, 581, 127

Böttcher, M., Reimer, A., Sweeney, K., & Prakash, A. 2013, ApJ, 768, 54

Breeveld, A. A., Landsman, W., Holland, S. T., et al. 2011, in American Institute of Physics Conference Series, Vol. 1358, American Institute of Physics Conference Series, ed. J. E. McEnery, J. L. Racusin, & N. Gehrels, 373–376

Brisken, W. F., Fruchter, A. S., Goss, W. M., Herrnstein, R. M., & Thorsett, S. E. 2003, AJ, 126, 3090

Buckley, J. H., Akerlof, C. W., Biller, S., et al. 1996, ApJ, 472, L9

Cassidy, M., Fortson, L. F., Fowler, J. W., et al. 1997, International Cosmic Ray Conference, 5, 189

Catanese, M., & Sambruna, R. M. 2000, ApJ, 534, L39

Catanese, M., Bradbury, S. M., Breslin, A. C., et al. 1997, ApJ, 487, L143

Cerruti, M., Benbow, W., Chen, X., et al. 2017, A&A, 606, A68

Cerruti, M., Boisson, C., & Zech, A. 2013, A&A, 558, A47

Cerruti, M., Zech, A., Boisson, C., & Inoue, S. 2015, MNRAS, 448, 910

Chen, X., Pohl, M., & Böttcher, M. 2015, MNRAS, 447, 530

Cherenkov, P. A. 1934, Doklady Akademii Nauk SSSR, 2, 451+

Cogan, P. 2008, International Cosmic Ray Conference, 3, 1385

Cohen, D. P., Romani, R. W., Filippenko, A. V., et al. 2014, ApJ, 797, 137

Cologna, G., Mohamed, M., Wagner, S., et al. 2015, in International Cosmic Ray Conference, Vol. 34, 34th International Cosmic Ray Conference (ICRC2015), 762

Cortina, J. 2013, The Astronomer's Telegram, 5038, 1

Costamante, L., Ghisellini, G., Giommi, P., et al. 2001, A&A, 371, 512

Cui, W. 2004, ApJ, 605, 662

D. B. Kieda for the VERITAS Collaboration. 2013, ArXiv e-prints, arXiv:1308.4849

Danforth, C. W., Keeney, B. A., Stocke, J. T., Shull, J. M., & Yao, Y. 2010, ApJ, 720, 976

Daniel, M. K. 2008, International Cosmic Ray Conference, 3, 1325

Daniel, M. K., Badran, H. M., Bond, I. H., et al. 2005, ApJ, 621, 181

Davies, J. M., & Cotton, E. S. 1957, Solar Energy, 1, 16 , the Proceedings of the Solar Furnace Symposium de Naurois, M. 2006, ArXiv Astrophysics e-prints, astro-ph/0607247

Dwek, E., & Krennrich, F. 2013, Astroparticle Physics, 43, 112

Edelson, R. A., Krolik, J. H., & Pike, G. F. 1990, ApJ, 359, 86

Essey, W., Kalashev, O., Kusenko, A., & Beacom, J. F. 2011, ApJ, 731, 51

Essey, W., & Kusenko, A. 2010, Astroparticle Physics, 33, 81

—. 2014, Astroparticle Physics, 57, 30

F. Hess, V. 1912, Physikalische Zeitschrift, 13, 1084

Fabian, A. C. 2012, ARA&A, 50, 455

Falcone, A. D., Cui, W., & Finley, J. P. 2004, ApJ, 601, 165

Fanaroff, B. L., & Riley, J. M. 1974, MNRAS, 167, 31P

Fermi, E. 1949, Physical Review, 75, 1169

Ferreira, J., Dougados, C., & Cabrit, S. 2006, A&A, 453, 785

Ferrigno, C., Blasi, P., & de Marco, D. 2004, Nuclear Physics B Proceedings Supplements, 136, 191

Finke, J. D. 2013, ApJ, 763, 134

Finke, J. D., & Becker, P. A. 2015, ApJ, 809, 85

Fioc, M., & Rocca-Volmerange, B. 1999, ArXiv Astrophysics e-prints, astro-ph/9912179

Fitzpatrick, E. L. 1999, PASP, 111, 63

Fomin, V. P., Stepanian, A. A., Lamb, R. C., et al. 1994, Astroparticle Physics, 2, 137

Fossati, G., Buckley, J., Edelson, R. A., Horns, D., & Jordan, M. 2004, New Astro. Rev, 48, 419

Fossati, G., Maraschi, L., Celotti, A., Comastri, A., & Ghisellini, G. 1998, MNRAS, 299, 433

Fossati, G., Buckley, J. H., Bond, I. H., et al. 2008, ApJ, 677, 906

Fragile, P. C., & Meier, D. L. 2009, ApJ, 693, 771

Franceschini, A., Rodighiero, G., & Vaccari, M. 2008, A&A, 487, 837

Furniss, A., Williams, D. A., Danforth, C., et al. 2013, ApJ, 768, L31

Furniss, A., Noda, K., Boggs, S., et al. 2015, ApJ, 812, 65

Gabányi, K. É., Dubner, G., Giacani, E., et al. 2013, ApJ, 762, 63

Galbraith, W., & Jelley, J. V. 1953, Nature, 171, 349

Georganopoulos, M., & Kazanas, D. 2003, ApJ, 594, L27

Ghisellini, G., & Tavecchio, F. 2008, MNRAS, 387, 1669

Ghisellini, G., Tavecchio, F., & Chiaberge, M. 2005, A&A, 432, 401

Ghisellini, G., Della Ceca, R., Volonteri, M., et al. 2010, MNRAS, 405, 387

Gilmore, R. C., Somerville, R. S., Primack, J. R., & Domínguez, A. 2012, MNRAS, 422, 3189

Giommi, P., Padovani, P., Polenta, G., et al. 2012, MNRAS, 420, 2899

Gliozzi, M., Sambruna, R. M., Jung, I., et al. 2006, The Astrophysical Journal, 646, 61

Hachisuka, K., Choi, Y. K., Reid, M. J., et al. 2015, ApJ, 800, 2

Hanna, D., McCann, A., McCutcheon, M., & Nikkinen, L. 2010, Nuclear Instruments and Methods in Physics Research A, 612, 278

Harrison, C. 2014, PhD thesis, Durham University ¡EMAIL¿c.m.harrison@durham.ac.uk¡/EMAIL¿

Hauser, M. G., & Dwek, E. 2001, ARA&A, 39, 249

Heck, D., Knapp, J., Capdevielle, J. N., Schatz, G., & Thouw, T. 1998, CORSIKA: a Monte Carlo code to simulate extensive air showers. (TIB Hannover)

Heitler, W. 1954, The Quantum Theory of Radiation (Oxford University Press, London), 386

Hervet, O., Boisson, C., & Sol, H. 2015, A&A, 578, A69

H.E.S.S. Collaboration, Abramowski, A., Acero, F., et al. 2010, A&A, 520, A83

Hillas, A. M. 1985, International Cosmic Ray Conference, 3

—. 2013, Astroparticle Physics, 43, 19

Holder, J., Bond, I. H., Boyle, P. J., et al. 2003, ApJ, 583, L9

Holder, J., Atkins, R. W., Badran, H. M., et al. 2006, Astroparticle Physics, 25, 391

Hovatta, T., Aller, M. F., Aller, H. D., et al. 2014, AJ, 147, 143

Jannuzi, B. T., Yanny, B., & Impey, C. 1997, ApJ, 491, 146

Jones, T. W., O'dell, S. L., & Stein, W. A. 1974, ApJ, 188, 353

Kalberla, P. M. W., Burton, W. B., Hartmann, D., et al. 2005, A&A, 440, 775

Kara, E., Errando, M., Max-Moerbeck, W., et al. 2012, ApJ, 746, 159

Kataoka, J., Takahashi, T., Makino, F., et al. 2000, ApJ, 528, 243

Katarzyński, K., Ghisellini, G., Tavecchio, F., et al. 2005, A&A, 433, 479

Katarzyński, K., Sol, H., & Kus, A. 2001, A&A, 367, 809

Kato, S. 1979, PASJ, 31, 495

Kellermann, K. I., Sramek, R., Schmidt, M., Shaffer, D. B., & Green, R. 1989, AJ, 98, 1195

Kertzman, M. P., & Sembroski, G. H. 1994, Nuclear Instruments and Methods in Physics Research A, 343, 629

Khan, E., Goriely, S., Allard, D., et al. 2005, Astroparticle Physics, 23, 191

Kirk, J. G., Rieger, F. M., & Mastichiadis, A. 1998, A&A, 333, 452

Klein, O., & Nishina, T. 1929, Zeitschrift fur Physik, 52, 853

Klepser, S. 2012, Astroparticle Physics, 36, 64

Konigl, A. 1981, ApJ, 243, 700

Koning A. J., H. S., & C., D. M. 2008, EDP Sciences, Proceedings of International Conference on Nuclear Data for Science and Technology, 211

Krause, M., & the VERITAS Collaboration. 2017, AIP Conference Proceedings, 1792, 040002

Krawczynski, H., Hughes, S. B., Horan, D., et al. 2004, ApJ, 601, 151

Landi, R., Stephen, J. B., Masetti, N., et al. 2009, A&A, 493, 893

Lee, S. 1998, Physical Review D, 58, 043004

Li, H., & Kusunose, M. 2000, ApJ, 536, 729

Li, T.-P. 2001, CJAA, 1, 313

Li, T.-P., & Ma, Y.-Q. 1983, ApJ, 272, 317

Linford, J. D., Taylor, G. B., Romani, R. W., et al. 2012, ApJ, 744, 177

Lomb, N. R. 1976, Ap&SS, 39, 447

Longair, M. 1992, High Energy Astrophysics (Cambridge University Press), 443–445

—. 2003, Theoretical Concepts in Physics: An Alternative View of Theoretical Reasoning in Physics (Cambridge University Press), 470–471

Lorenz, E., & Wagner, R. 2012, European Physical Journal H, 37, 459

Madhavan, A. 2013, PhD thesis, Iowa State University

Malizia, A., Landi, R., Bassani, L., et al. 2007, ApJ, 668, 81

Marscher, A. P. 1980a, ApJ, 235, 386

—. 1980b, ApJ, 235, 386

—. 2009, ArXiv e-prints, arXiv:0909.2576

Marscher, A. P., & Gear, W. K. 1985, ApJ, 298, 114

Martí-Vidal, I., Muller, S., Vlemmings, W., Horellou, C., & Aalto, S. 2015, Science, 348, 311

Massaro, E., Giommi, P., Leto, C., et al. 2009, A&A, 495, 691

Matthews, J. 2005, Astroparticle Physics, 22, 387

Max-Moerbeck, W., Hovatta, T., Richards, J. L., et al. 2014, MNRAS, 445, 428

Mertens, F., & Lobanov, A. P. 2016, A&A, 587, A52

Meyer, E. T., Fossati, G., Georganopoulos, M., & Lister, M. L. 2011, ApJ, 740, 98

Meyer, M., & Horns, D. 2013, ArXiv e-prints, arXiv:1310.2058

Mortlock, D. J., Warren, S. J., Venemans, B. P., et al. 2011, Nature, 474, 616

Mücke, A., Engel, R., Rachen, J. P., Protheroe, R. J., & Stanev, T. 2000, Computer Physics Communications, 124, 290

Mücke, A., & Protheroe, R. J. 2001, Astroparticle Physics, 15, 121

Mücke, A., Protheroe, R. J., Engel, R., Rachen, J. P., & Stanev, T. 2003, Astroparticle Physics, 18, 593

Mushotzky, R. F., Done, C., & Pounds, K. A. 1993, ARA&A, 31, 717

Nalewajko, K. 2016, Galaxies, 4, 28

Nandikotkur, G., Jahoda, K. M., Hartman, R. C., et al. 2007, ApJ, 657, 706

Netzer, H. 2015, ARA&A, 53, 365

Nolan, P. L., Abdo, A. A., Ackermann, M., et al. 2012, ApJS, 199, 31

Ojha, R., Kadler, M., Böck, M., et al. 2010, ArXiv e-prints, arXiv:1001.0059

Oppenheim, A. V., & Schafer, R. W. 1975, NASA STI/Recon Technical Report A, 76

Ostorero, L., Villata, M., & Raiteri, C. M. 2004, A&A, 419, 913

Padovani, P. 2011, MNRAS, 411, 1547

Padovani, P., & Giommi, P. 1995, MNRAS, 277, 1477

Padovani, P., Alexander, D. M., Assef, R. J., et al. 2017, A&A Rev., 25, 2

Paiano, S., Landoni, M., Falomo, R., et al. 2017, ApJ, 837, 144

Park, N., & the VERITAS Collaboration. 2015, ArXiv e-prints, arXiv:1508.07070

Patrignani, C., & Particle Data Group. 2016, Chinese Physics C, 40, 100001

Peter, D., Domainko, W., Sanchez, D. A., van der Wel, A., & Gässler, W. 2014, A&A, 571, A41

Peterson, B. M., Bentz, M. C., Desroches, L.-B., et al. 2005, ApJ, 632, 799

Piner, B. G., & Edwards, P. G. 2004, ApJ, 600, 115

Piron, F., Djannati-Atai, A., Punch, M., et al. 2001, A&A, 374, 895

Primack, J. R., Bullock, J. S., & Somerville, R. S. 2005, in American Institute of Physics Conference Series, Vol. 745, High Energy Gamma-Ray Astronomy, ed. F. A. Aharonian, H. J. Völk, & D. Horns, 23–33

Prokhorov, D. A., & Moraghan, A. 2017, MNRAS, 471, 3036

Punch, M., Akerlof, C. W., Cawley, M. F., et al. 1992, Nature, 358, 477

Pushkarev, A. B., Kovalev, Y. Y., Lister, M. L., & Savolainen, T. 2009, A&A, 507, L33

Raiteri, C. M., Stamerra, A., Villata, M., et al. 2015, MNRAS, 454, 353

Ramakrishnan, V., Hovatta, T., Nieppola, E., et al. 2015, MNRAS, 452, 1280

Reynolds, S. P. 1982, ApJ, 256, 13

Rieger, F. M. 2004, ApJ, 615, L5

—. 2007, Ap&SS, 309, 271

Rieger, F. M., Bosch-Ramon, V., & Duffy, P. 2007, Ap&SS, 309, 119

Robertson, D. R. S., Gallo, L. C., Zoghbi, A., & Fabian, A. C. 2015, MNRAS, 453, 3455

Rodríguez-Pascual, P. M., Alloin, D., Clavel, J., et al. 1997, ApJS, 110, 9

Rolke, W. A., & López, A. M. 2001, Nuclear Instruments and Methods in Physics Research A, 458, 745

Romero, G. E., Boettcher, M., Markoff, S., & Tavecchio, F. 2017, Space Sci. Rev., 207, 5

Rovero, A. C., Muriel, H., Donzelli, C., & Pichel, A. 2016, A&A, 589, A92

Rybicki, G. B., & Lightman, A. P. 1986, Radiative Processes in Astrophysics, 400

Sandrinelli, A., Covino, S., & Treves, A. 2014, ApJ, 793, L1

Sandrinelli, A., Covino, S., Treves, A., et al. 2017, A&A, 600, A132

Sbarufatti, B., Treves, A., & Falomo, R. 2005, ApJ, 635, 173

Scargle, J. D. 1982, ApJ, 263, 835

Schlafly, E. F., & Finkbeiner, D. P. 2011, ApJ, 737, 103

Sembay, S., Warwick, R. S., Urry, C. M., et al. 1993, ApJ, 404, 112

Shahinyan, K., & the VERITAS Collaboration. 2015, ArXiv e-prints, arXiv:1508.07358

Shapiro, S., & Teukolsky, S. 1983, Black holes, white dwarfs, and neutron stars: the physics of compact objects, A Wiley-interscience publication (Wiley)

Sikora, M., Begelman, M. C., & Rees, M. J. 1994, ApJ, 421, 153

Sol, H., Pelletier, G., & Asseo, E. 1989, MNRAS, 237, 411

Stickel, M., Fried, J. W., & Kuehr, H. 1993, A&AS, 98, 393

Stickel, M., Padovani, P., Urry, C. M., Fried, J. W., & Kuehr, H. 1991, ApJ, 374, 431

Stocke, J. T., Morris, S. L., Gioia, I. M., et al. 1991, ApJS, 76, 813

Straal, S. M., Gabanyi, K. E., van Leeuwen, J., et al. 2016, ArXiv e-prints, arXiv:1603.01226

Stroh, M. C., & Falcone, A. D. 2013, ApJS, 207, 28

Tammi, J., & Duffy, P. 2009, MNRAS, 393, 1063

Tanaka, Y. T., Stawarz, Ł., Finke, J., et al. 2014, ApJ, 787, 155

Tavecchio, F., Ghisellini, G., Foschini, L., et al. 2010, MNRAS, 406, L70

Tavecchio, F., Maraschi, L., & Ghisellini, G. 1998, ApJ, 509, 608

The Fermi-LAT Collaboration. 2013, ArXiv e-prints, arXiv:1306.6772

—. 2017, ArXiv e-prints, arXiv:1702.00664

Thompson, D. J. 2015, Comptes Rendus Physique, 16, 600

Ulrich, M.-H., Kinman, T. D., Lynds, C. R., Rieke, G. H., & Ekers, R. D. 1975, ApJ, 198, 261

Ulrich, M.-H., Maraschi, L., & Urry, C. M. 1997, ARA&A, 35, 445

Urry, C. M., & Padovani, P. 1995, PASP, 107, 803

van Moorsel, G., Kemball, A., & Greisen, E. 1996, in Astronomical Society of the Pacific Conference Series, Vol. 101, Astronomical Data Analysis Software and Systems V, ed. G. H. Jacoby & J. Barnes, 37

VanderPlas, J. T. 2017, ArXiv e-prints, arXiv:1703.09824

Vaughan, S., Edelson, R., Warwick, R. S., & Uttley, P. 2003, MNRAS, 345, 1271

Weekes, T. C., & Turver, K. E. 1977, in ESA Special Publication, Vol. 124, Recent Advances in Gamma-Ray Astronomy, ed. R. D. Wills & B. Battrick

Weekes, T. C., Cawley, M. F., Fegan, D. J., et al. 1989, ApJ, 342, 379

Welch, P. 1967, IEEE Transactions on Audio and Electroacoustics, 15, 70

Wood, M., Caputo, R., Charles, E., et al. 2017, ArXiv e-prints, arXiv:1707.09551

Wright, E. L., Eisenhardt, P. R. M., Mainzer, A. K., et al. 2010, AJ, 140, 1868

Yan, D., Kalashev, O., Zhang, L., & Zhang, S.-N. 2015, MNRAS, 449, 1018

Yan, D., & Zhang, L. 2015, MNRAS, 447, 2810

Zhang, P.-f., Yan, D.-h., Liao, N.-h., & Wang, J.-c. 2017, ApJ, 835, 260